UNIVERSITAT POLITÈCNICA
DE CATALUNYA
BARCELONATECH

Advanced Discontinuous Integral-Equation Schemes for the Versatile Electromagnetic Analysis of Complex Structures

Author

Ivan Sekulić

Thesis Advisor

Eduard Úbeda Farré

A thesis submitted to the Universitat Politècnica de Catalunya (UPC)
in partial fulfillment of the requirements for the degree of
DOCTOR OF PHILOSOPHY

Department of Signal
Theory and Communications

Ph.D. program on Signal Theory and Communications
CommSensLab
Barcelona, April 2019

Abstract

The most prominent surface integral equations, the electric field integral equation (EFIE) used for the scattering analysis of perfectly electrically conducting (PEC) targets and the Poggio–Miller–Chang–Harrington–Wu–Tsai (PMCHWT) formulation commonly utilized for the analysis of homogeneous penetrable objects, are usually discretized, in the context of method of moments (MoM), with edge-based divergence-conforming basis functions. Divergence-conforming discretizations of the EFIE and PMCHWT formulations excel as conforming schemes, hence with converging solutions in the physical space of currents. However, the divergence-conforming MoM implementations require the underlying mesh to be geometrically conformal, with pairs of adjacent facets sharing a single edge. The development of divergence-conforming schemes for composite objects with junctions, viz. boundary lines where more than two regions intersect, becomes somewhat awkward because of the definition of special continuity conditions at junctions. Moreover, the meshes arising from the juxtaposition of independently meshed subdomains in the modular design of complex objects are typically nonconformal and thus not suitable for conventional divergence-conforming MoM schemes.

In this thesis, we address the robust, accurate and versatile scattering analysis of PEC and penetrable objects with arbitrary shape and composite objects with junctions meshed with conformal or nonconformal meshes. For this purpose, we employ the EFIE–PMCHWT integral-equation formulation, which follows from the application of the EFIE or PMCHWT formulations over boundary surfaces, respectively, enclosing PEC regions or separating penetrable regions. The proposed schemes rely on the expansion of the currents with the facet-based, discontinuous-across-edges basis functions. This choice gives rise to boundary integrals with hypersingular kernels, which we handle by testing the equations with well-suited testing functions defined off the boundary tessellation, inside the region where, in light of the surface equivalence principle, the fields must be zero. Our facet-based EFIE-PMCHWT implementations exhibit improved accuracy when compared with the conventional continuous schemes in the analysis of sharp-edged targets where the accurate modelling of singular fields is of great importance. Moreover, our schemes manifest in general great flexibility in the analysis of composite objects with junctions as the special modelling of currents at junctions is not required. Finally, the proposed implementations can handle geometrically nonconformal meshes when applied to piecewise (or fully) homogeneous arbitrarily shaped objects.

Acknowledgments

First and foremost, I would like to express my sincere gratitude to my supervisor, Associate Professor Eduard Úbeda. Eduard was always there when I needed his help or advice, and not only related to numerical methods. His hard-working attitude, patience and ability to stay calm in stressful moments will serve as a constant inspiration for the years to come. For all these, and much more, *grácies, Eduard.*

Next, I would like to thank Professor Juan M. Rius and Associate Professor Alexander Heldring, the other two members of computational electromagnetics group, for kindly accepting me and for all the fruitful discussions we had on a diverse range of topics. I met so many wonderful people in CommSensLab who made my stay here at UPC a delightful experience. Here I mention Professors Lluis Jofre and Jordi Romeu with whom I had the opportunity to organize European Schools of Antennas. Aynie Khoe and Beni Vazquez, thank you for helping me with all the bureaucratic stuff.

Part of this thesis was conducted in the Electromagnetics Research Group, Department of Electronics and Nanoengineering, School of Electrical Engineering, Aalto University, Finland. I would like to convey my gratitude to my host, Dr. Pasi Ylä-Oijala, for warmly welcoming me to the group and being there for everything I needed. Special thanks to Dimitrios Tzarouchis and Dr. Seppo Järvenpää, with whom I had the privilege to collaborate with in Finland.

I had a lot of fun here in Barcelona, and for this, the responsible are my Croatian friends, Mislav, Zvonko and Katarina. We have seen so many places together, and these will always remain the most memorable experiences. I had the opportunity and privilege to share the flat with many people. Rodrigo, thank you for accepting me when I first came here to Barcelona. Vlada, my Serbian flatmate and a friend, thank you for all the bike trips we had and for being patient and showing me the benefits of C++ programming language. Many people visited me here in Barcelona and made my stay away from home much more enjoyable. Klaudio, Marko, Djole, Zvone, Vale, and two Filips, I know you have enjoyed Barcelona.

Finally, I would like to thank my family, my mother, father and brother, without whom all of this would not be possible.

Contents

Acronyms

MoM Method of Moments

EFIE Electric Field Integral Equation

MFIE Magnetic Field Integral Equation

CFIE Combined Field Integral Equation

FEM Finite Element Method

FDTD Finite Difference Time Domain

TLM Transmission Line Matrix

EM ElectroMagnetic

VIE Volume Integral Equations

SIE Surface Integral Equations

EFIO Electric Field Integral Operator

MFIO Magnetic Field Integral Operator

PMCHWT Poggio–Miller–Chang–Harrington–Wu–Tsai

CTF Combined Tangential Formulation

MLFMA Multilevel Fast Multipole Algorithm

MLMDA Multilevel Matrix Decomposition Algorithm

ACA Adaptive Cross Approximation

DDM Domain Decomposition Methods

PEC Perfect Electric Conductor

2D Two-dimensional

3D Three-dimensional

TE Transverse Electric

TM Transverse Magnetic

BC Buffa-Christiansen

dof degrees of freedom

CPU Central Processing Unit

RCS Radar Cross Section

IEDG Integral Equation Discontinuous Galerkin

GMRS Generalized Minimal RESidual Method

RWG Rao-Wilton-Glisson basis functions

DDA Discrete Dipole Approximation

EO Even-Odd

UPC Universitat Politècnica de Catalunya

List of Figures

Chapter 1
Introduction

1.1 A brief overview of numerical methods in electromagnetics

The classical electromagnetic theory is governed with a set of four partial differential equations describing the space and time dependence of the electromagnetic field, named by its creator, Maxwell's equations [1]. In the design process of electrical devices, e.g., antennas, transformers, induction motors, radar systems, or metamaterials, the solution of Maxwell's equations is indispensable. However, the analytical solution to these equations can be obtained just for a few canonical geometries which severely limits their practical application (an example is scattering analysis of a sphere described in a seminal work of Gustav Mie [2]). A scientific discipline called computational (numerical) electromagnetics is developed in order to seek the electromagnetic solutions previously intractable for analytical methods. With the advent of powerful computers, numerical methods are becoming increasingly relevant. The numerical solution is organized in terms of a set of data, which provides limited insight into the solution of a mathematical task, whereas the analytical solution gives a fully comprehensive picture, in terms of functions. On the other hand, the numerical procedure is organized as a set of standardized steps while the analytical procedures often differ from task to task. Most importantly, numerical methods can solve almost any electromagnetic problem, which is a great asset in cases where there are no valid analytical approaches. The most relevant numerical methods in the full-wave computational analysis of electromagnetic fields can be roughly divided into two classes: differential equation methods and integral equation methods. The most popular differential equation methods in the numerical analysis of electromagnetic fields are: finite element method (FEM) [3,4], finite difference time domain method (FDTD) [5] and transmission line matrix method (TLM) [6]. These methods discretize the differential operator of the wave equation directly and solve for the unknown fields. Therefore, in the analysis of open problems with unbounded domains, the computational region has to be truncated artificiality and special absorbing conditions have to be defined [7]. On the other hand, these methods excel in the analysis of inhomogeneous, anisotropic and nonlinear problems producing sparse interaction matrices, which is a favourable property for iterative methods.

Integral equation methods are well suited for the analysis of open problems since the radiation condition at infinity is inherently satisfied in the analytical formulation and truncation of the domain under interest is not necessary. Therefore they are especially attractive tools in the analysis of scattering and radiation problems (antenna arrays, radar-cross-section calculations, computation of forces and torques exhibited by the wave

on a particle). Volume integral equations (VIE) discretize the interior of the target under consideration making them perfectly suitable for the scattering analysis of inhomogeneous and/or anisotropic targets. If the structure under interest is piecewise homogeneous and isotropic, surface integral equations (SIE) are preferable tools since both the unknowns and the analysis lie on the boundary-interfaces between the different homogeneous regions resulting in comparatively smaller interaction matrices. If the structure under consideration allows approximation with a boundary condition, such as good conductors with PEC condition, the SIE are very attractive since they can be restricted to the boundary-surface of the object. In that case, the target can be considered as *impenetrable* avoiding modelling of the interior fields.
In this thesis, we focus on the electromagnetic scattering analysis of piecewise homogeneous and isotropic targets. For this reason, SIE are the central topic of this research.

1.2 Surface integral equation methods

The first step in the derivation of surface integral equations is the transformation of Maxwell's equations to equivalent integral representations for the fields. This is achieved with the help of vector Green's identities [8] and appropriate Green's function [8]. The scattered fields are then expressed as the spatial convolution of the currents, the unknowns, defined over the interface-surfaces between different homogeneous regions, and the Green's function of the problem. Finally, the integral equation is constructed by invoking appropriate boundary conditions on the surface of the target. The method of moments [9], proposed by Harrington in 1968., is the most widespread numerical scheme used in the discretization of boundary integral equations. In the standard MoM approach, the unknown rotated tangential traces of total electromagnetic fields residing on the boundary of the target, the equivalent electric and magnetic currents, are expanded with suitable sets of basis functions. Then, the discretized equations are cast into matrix form by means of testing the tangential field traces with appropriate sets of testing functions.
Essentially, there are two kinds of surface integral operators present in the electromagnetic scattering analysis of piecewise homogeneous targets, namely; the electric field integral operator (EFIO) and the magnetic field integral operator (MFIO), which for the case of PEC objects, in combination with appropriate tangential boundary conditions defined on the surface of the target, give rise to the electric field integral equation (EFIE) and the magnetic field integral equation (MFIE). The EFIE is applicable to open and closed surfaces, while MFIE can be applied just to closed surfaces. Usually, EFIE yields more accurate results than the MFIE especially for the cases of objects with sharp edges and corners. Substantial effort has been invested in order to improve the accuracy of the MFIE; accurate computation of the Gram matrix [10], discretization with discontinuous basis functions [11] or the mixed discretization conforming to the relevant function spaces [12]. The EFIE is a fundamentally ill-conditioned equation plagued with problems like a dense-discretization breakdown or low-frequency breakdown associated with the condition number of the discretized electric field integral operator. Remedies to these problems are given in form of, for example, Calderon preconditioner [13] and quasi-Helmholtz decomposition [14]- [17], respectively. Neither EFIE or MFIE are uniquely solvable for all the frequencies of interest. They break down at resonant frequencies for which the associated integral operators have a null space. The remedy to this problems

is given in the form of the combined field integral equation (CFIE), which results from the linear combination of the MFIE and the EFIE. Although uniquely solvable for all the frequencies of interests, CFIE inherits the above-mentioned problems characteristic to the EFIE and MFIE.
On the other hand, many surface integral equation formulations can be developed for the scattering analysis of homogeneous penetrable bodies. They arise from different combinations of EFIO and MFIO, coupling coefficients between them, and appropriate boundary conditions defined on both sides of the surface [18]. The most prominent representatives are Poggio–Miller–Chang–Harrington–Wu–Tsai (PMCHWT) formulation [19]- [21], combined tangential formulation (CTF) [22], and NMüller formulation [23]. Each of these formulations has its characteristic properties which makes them suitable for a particular class of problems.

1.2.1 Fast solvers and preconditioning

The standard MoM discretization of integral operators gives rise to densely populated system matrices due to the presence of the Green's function. This represents a major bottleneck since memory requirements scale as $\mathcal{O}(N^2)$ and computational complexity of direct inversion scales as $\mathcal{O}(N^3)$, where N is the number of degrees of freedom in the system. The direct solution of the MoM linear system hence becomes prohibitively costly for a large enough number of unknowns, limited in practice to problems with a total surface at most of roughly $100\lambda^2$ (λ is the free-space wavelength). Instead, iterative Krylov subspace methods are used. They rely on a sequence of matrix-vector products in order to find a solution to the linear system of equations. The computational complexity of such methods scale as $\mathcal{O}(\alpha N^2)$, where α is the number of iterations required to reach the desired accuracy in the solution vector. Hence, since the required computational effort per iteration now scales as $\mathcal{O}(N^2)$, the global time to ensure convergence in the iterative search of the solution may be minimized drastically with a moderate number of iterative steps. A wide range of fast iterative methods, such are the multilevel fast multipole algorithm (MLFMA) [24], the multilevel matrix decomposition algorithm (MLMDA) [25], [26], and the adaptive cross approximation (ACA) [27] have been developed to further accelerate the matrix-vector product associated with iterative solvers, and reduce the memory consumption. Most of them are based on multilevel decomposition algorithms so that the computational cost per iteration and the memory requirements scale as $\mathcal{O}(Nlog^pN)$, where p is a positive real number characteristic to the particular fast method. However, in order to minimize the number of iterations required to reach convergence, the impedance matrix has to be well-conditioned. The MFIE is a well-conditioned equation since it consists of a compact operator (MFIO) (on smooth surfaces) and identity operator. Accordingly, its condition number (ratio of the maximum and minimum singular value of the impedance matrix) is low. Conversely, the EFIE has two forms of ill-conditioning; the low-frequency breakdown and the dense-discretization breakdown. The low-frequency breakdown of the EFIE is due to the different frequency scaling of the singular and hypersingular parts of the EFIO. Singular vector potential operator scales proportionally with the frequency, while the hypersingular scalar potential operator is inversely proportional to the frequency. Therefore, when frequency goes to zero, the singular values of scalar and vector potential operators are driven apart, and the condition number grows. A classical remedy to this problem is given by the surface quasi-Helmholtz decomposition [14]- [17].

If the surface of the target is simply connected, the discretized current space can be decomposed to solenoidal and non-solenoidal subspaces. Then loop (solenoidal) and star or tree (non-solenoidal) basis functions [14]- [17] are used to capture each of the subspaces. With proper frequency scaling of the resultant system matrix, the low-frequency breakdown is cured. Another way to circumvent this breakdown is by treating the charge density as an independent unknown [28]. As the average mesh size h reduces i.e. the number of unknowns increases, the condition number of the discretized EFIO scales as $1/h^2$ indicating that EFIE is ill-conditioned when discretization becomes finer. This so-called dense-discretization breakdown can be cured by exploiting Calderón identity [29], i.e. the fact that the square of the EFIO gives rise to the compact plus identity operator. However, Calderón preconditioner has to be carefully crafted in order to incorporate it effectively into the existing MoM codes [13]. Virtually all the surface integral formulations can be represented as a combination of the EFIO, MFIO, the identity operator and appropriate boundary conditions. Therefore, the presence of the aforementioned integral operators reflects on the properties of particular equation.
In the analysis of large and multi-scale problems, the resultant impedance matrix is often ill-conditioned due to the disparate electrical sizes of the structure components. Domain decomposition methods (DDM) offer the most effective preconditioners for these kinds of problems. The multi-scale structure is decomposed into a union of separate non-overlapping subdomains that are meshed independently according to their respective electrical sizes and local features. The convergence of DDM is strongly dependent on the transmission conditions established between adjacent subdomains. The transition of the tangential fields between neighbouring subdomains can be enforced with auxiliary unknowns defined on artificial closing surfaces [30] or with the definition of discontinuous monopolar-RWG basis functions along the tearing contour arising in the decomposition of the original object [31]- [33]. To accelerate the iterative search of the solution, a block-diagonal preconditioner is implemented, with the blocks accounting for the self-subdomain interactions.

1.2.2 Conforming discretizations of surface integral equations

For the majority of problems of practical interest, SIE can not be solved analytically. Method of moments [9] is the most widely used numerical scheme in the discretization of SIE. Usually, the boundary of the target (Γ) is tessellated into a union of non-overlapping facets, the mesh, and the unknown currents are expanded with a known set of basis functions with the local support on the mesh. These are divergence-conforming sets, such as the Rao-Wilton-Glisson (RWG) set [34], which enforce normal continuity across the edges arising from the discretization of the boundary and span a finite-dimensional subspace inside $H^{-1/2}(div_\Gamma, \Gamma)$ [35], the function space that encompasses the physical space of the currents. RWG set is a low-order divergence-conforming set which provides piecewise linear expansion of the currents on a particular facet. However, a piecewise linear approximation becomes rather simple whereby too many basis functions may be required to achieve the desired accuracy, for example, in the analysis of sharp-edged objects with detailed intricacy, concave cavities or electrically large targets. Instead, higher order divergence-conforming basis functions, based on piecewise high order polynomials, are developed to reach better accuracy for the same number of degrees of freedom (dof). To reach their full potential, higher order basis function have to be coupled with higher

order modelling of the geometry. Significant work in this area has been done, among others, by Kolundžija, Popović, Notaroš [36]- [38], Graglia, Peterson and Wilton [39], [40]. Furthermore, in the scattering analysis of objects with sharp edges and corners, singular fields are induced around geometrical singularities. Their accurate representation is of great importance, and special singular higher order divergence-conforming basis functions of the additive kind have been proposed [41].
After the SIE are discretized, they are cast into a matrix form by means of testing the tangential field traces with a proper set of testing functions. For the discretization to be conforming to the function spaces, the testing has to be done in the dual space of the range of the tangential-trace operators [12], [42], [43].
For example, in the conforming RWG discretization of the EFIE and the PMCHWT, the proper testing space is $H^{-1/2}(div_\Gamma, \Gamma)$, whereby RWG set can be used as a testing set giving rise to conforming Galerkin discretization. Conforming discretizations are favourable since solutions will converge in the physical space of the currents [44], [45].
However, since the divergence-conforming basis functions are edge-based, embracing at least two edge-adjacent facets, the conforming implementations are only valid for conformal meshes, where pairs of neighbouring facets have a single edge in common. This stringent condition gives rise to the plethora of problems in the analysis of real-life objects, a topic to which this thesis is partially dedicated.

1.2.3 Discontinuous discretizations of SIE for the analysis of composite and multi-scale structures

Generating a geometrically conformal mesh for a realistic multi-scale structure composed of parts with disparate electrical sizes is a daunting task. Moreover, the successful construction of such meshes often leads to ill-conditioned impedance matrices, which slow down the iterative search of the solution with Krylov subspace methods. For example, a PEC aircraft represents a multi-scale structure (wings, propellers, cabin, flaps, airframe) that assembles features with very different electrical dimensions. Generating a conformal mesh for such problem as a whole becomes, therefore, a very demanding task. Instead, it is much more agile to undertake the independent meshing of the constituent parts (subdomains) of the aircraft and assemble them back in the original structure. The resulting mesh, however, becomes geometrically nonconformal; that is, it arises from the juxtaposition of open independent triangulations with nonmatching edges. Moreover, the definition of divergence-conforming bases for piecewise homogeneous composite objects meshed with conformal meshes around junction-edges, viz. boundary lines where more than two regions intersect, becomes demanding from the implementation point of view [46]- [50]. In any case, these conforming *single-surface* (or *single-trace*) techniques yield accurate results with comparatively small number of degrees of freedom and have been widely used despite the inherently associated programming complications. In order to increase the versatility of the method, other so-called *two-surface* [51] or *multi-trace* [52] conforming schemes have been implemented. These approaches avoid the special management of junction-edges by considering the composite object as a union of isolated homogeneous subdomains defined in a host medium, with the separation distances tending to zero. These schemes provide improved flexibility when managing composite targets with junctions at the cost of additional redundant degrees of freedom defined on touching surfaces.

The conventional conforming MoM approaches which normally use divergence-conforming basis functions require, by definition, the underlying mesh to be geometrically conformal, with all pairs of adjacent facets sharing a single edge. Therefore, the application of such schemes to geometrically nonconformal meshes, which often arise in the modular design of objects, or as a flaw in the construction of a conformal mesh, where adjacent facets may not share single edges, appears unworkable.
Clearly, a breakaway from the standard edge-based MoM schemes is needed. Recently, discontinuous facet-based discretizations of integral equations have been introduced for the analysis of PEC [11], [53]- [56], penetrable [57]- [62] or composite [58], [62], [63] targets. The unknown tangential field traces are usually expanded with discontinuous-across-edges monopolar-RWG basis functions [11]. These implementations are nonconforming to the natural divergence function spaces since the finite-dimensional subspace spanned by the monopolar-RWG basis functions belongs to the space of square-integrable functions, $L^2(\Gamma)$. Interestingly, some of them exhibit similar or better accuracy than the conventional RWG-schemes in the scattering analysis of targets with sharp edges and corners, PEC [54]- [56], or penetrable [57]- [60], [62] especially if electrically small. In general, they exhibit great flexibility in the analysis of homogeneous targets meshed with nonconformal meshes [53]- [56], [61], [62]. Moreover, these schemes excel in the single-surface analysis of piecewise homogeneous composite objects with junctions as the special modelling of currents at junctions is not required [58], [62], [63]. The facet-based nonconforming schemes become also well suited for the enhancement of integral-equation domain decomposition methods [31]- [33], [61], [64] since the transmission conditions between contiguous subdomains may be satisfied through the discontinuous monopolar-RWG current expansion along the tearing contours.
The main bottleneck of the aforementioned integral equation methods discretized with the discontinuous basis and testing functions can be traced down to the necessity of the proper evaluation of the discretized hypersingular operator in the EFIE. Indeed, in the discontinuous Galerkin discretization of the scalar potential operator, double-contour integral arises, which becomes unbounded when the field integration point approaches the source point (on the same line). Over the last years, two different strategies have been proposed to make the unbounded kernel contributions numerically manageable, namely; compensating the double-contour integral through the introduction of the so-called *penalty terms* or directly evaluating the problematic integral through the non-Galerkin testing over small volumetric or surface domains attached to the boundary surface, defined inside the region where the fields must be zero according to the equivalence theorem.
Usually, there are two penalty terms added to the discontinuous Galerkin discretization of the EFIE; the first term is adjusted to directly cancel out the problematic double-contour integral, and the second one is introduced to weakly enforce the continuity of the currents across the adjacent mesh elements [53]. The second penalty term often comes with the multiplication factor dubbed *the interior penalty stabilization function.* However, the value of the interior penalty stabilization function often varies from case to case greatly influencing the accuracy and stability of the solution, and in some works, it is even set to zero, totally excluding the second penalty term [31], [61]. Moreover, the discontinuous Galerkin methods have been explored mainly in the context of scattering analysis of PEC targets. Their performance in the scattering analysis of penetrable targets has been less studied, with the exception of the work in [61], which deals mainly with low relative permittivity contrast dielectrics. In general, if the stabilization factor is well ad-

justed, the discontinuous Galerkin integral equation methods produce similar accuracy to standard divergence conforming implementations, but doubling the number of unknowns. Their performance in the scattering analysis of challenging problems like high relative permittivity contrast dielectrics, ferromagnetics or plasmonics remains unknown.
The second strategy relies on the direct evaluation of the unbounded contributions originating from the discontinuous discretization of the hypersingular operator through attentively designed non-Galerkin testing schemes. The testing elements are constructed off the boundary tessellation, in the region where the fields are compelled to be zero according to the surface equivalence theorem. Two families of discontinuous non-Galerkin testing schemes have been devised over the past few years; *volumetric* and surface *tangential-normal* scheme. They have been successfully applied to the scattering analysis of PEC 2D [58] and arbitrarily shaped 3D targets [54]- [56], penetrable 2D [58] and 3D targets [57], [59], [60], [62] or composite 2D [58] and 3D [62], [63] structures. Remarkably, these schemes often offer improved accuracy compared to the standard edge-based schemes in the scattering analysis of subwavelength objects with geometrical singularities (PEC targets, penetrable objects with high relative permittivity or permeability values and plasmonic nanoparticles). These are very challenging problems due to the appearance of the singular field quantities around sharp edges and corners, which accurate modelling may dominate the overall accuracy of the solution. Moreover, no additional contour penalty stabilization term is needed, which becomes very handy in the analysis of nonconformal meshes [64]. However, from the point of practical realization, the non-Galerkin discontinuous schemes become more complicated to implement than the Galerkin discontinuous counterparts since additional volumetric and line integrals have to be evaluated, and the original mesh has to be manipulated in order to construct the off-boundary testing entities.

1.3 Outline and the objectives of the thesis

This thesis focuses on the accurate nonconforming discontinuous discretizations of the most popular integral equations in electrodynamics, EFIE for PEC targets, and PMCHWT for homogeneous penetrable objects applied to 2D and 3D problems. The unknown currents are expanded with discontinuous set of basis functions, monopolar-RWG (3D) or discontinuous piecewise linear (2D), and the discretized equations are tested with surface(2D)/volumetric(3D) or line(2D)/surface(3D) tangential-normal non-Galerkin schemes. The objective of this thesis is to rigorously asses the accuracy and stability of new discontinuous implementations by testing them against challenging scattering problems. With extensive numerical tests, we prove that these formulations are more accurate than standard edge-based implementations in the scattering analysis of objects with sharp wedges or corners where singular field quantities are induced. Furthermore, we show how these schemes of discretization become versatile in the analysis of complex objects meshed with geometrically conformal or nonconformal meshes.

- Chapter 1 gives a general overview of the numerical methods in electromagnetics with a focus on integral equation formulations. The state of the art in the integral equation schemes is briefly delineated with the emphasis on discontinuous schemes, a subject to which we dedicate this doctoral thesis.

- Chapter 2 presents Maxwell's equations along with boundary conditions and the con-

stitutive relations. Scalar and vector potentials are introduced leveraging appropriate Green's function. Then, integral representations for the fields are given, and the fundamental surface integral equations are constructed.

- In Chapter 3, the standard conforming method of moments discretization of commonly used surface integral equations is presented. Necessary function spaces are introduced along with commonly used low order basis and testing functions.

- In Chapter 4, a discontinuous method of moments discretization of line integral equations applied to 2D problems is presented. The currents are expanded with discontinuous piecewise linear basis functions and the fields are tested with surface or line tangential-normal testing schemes. We show how these schemes offer improved accuracy in the analysis of single electrically small sharp-edged PEC targets (TE-scattering), sharp-edged dielectric targets with high relative permittivity contrast (TE-scattering) or sharp-edged ferromagnetic targets (TM-scattering) when compared to standard continuous piecewise linear schemes and the same number of dof. Furthermore, we show how our discontinuous schemes excel as versatile tools in the scattering analysis of infinitely long piecewise homogeneous composite objects with junctions.

- In Chapter 5, we introduce our discontinuous discretizations of commonly used surface integral equations. The unknown currents are expanded with a discontinuous-across-edges monopolar-RWG set. The discretized equations are cast into matrix form by testing the fields with volumetric or surface tangential-normal testing functions. Similarly to the observations in 2D, we show how these non divergence-conforming integral formulations boost the accuracy in the scattering analysis of subwavelength homogeneous targets, penetrable and PEC, with sharp edges and corners compared to standard edge-based divergence-conforming schemes and a similar number of dof. Moreover, we display the versatility of our discontinuous schemes in the scattering analysis of single homogeneous or composite piecewise homogeneous objects meshed with geometrically nonconformal meshes.

- Chapter 6 is dedicated to the hierarchical decomposition of the facet-based monopolar-RWG space to the edge-based even and odd monopolar-RWG subspaces. The even-odd monopolar-RWG discretization of PMCHWT formulation is used to analyse sharp-edged subwavelength plasmonic nanoparticles in resonance domain. We have observed faster convergence of computed scattering and absorption spectra, and improvements in the near-field region compared to the results obtained with RWG discretization of PMCHWT.

- The conclusions and future research lines are summarized in Chapter 7.

Chapter 2

Maxwell's Equations and Integral Representations for the Fields

2.1 Introduction

Maxwell's equations [1] are a set of coupled partial differential equations that provide a mathematical framework for the electromagnetic phenomena ranging from nano-scale to intergalactic scale. James Clerk Maxwell built upon the works of his predecessors, Gauss, Ampère, Faraday, and Coulomb, adding the concept of the *displacement currents*, i.e. the fact that the time-varying electric field induces the magnetic field, to the Ampère's law. This crucial term allowed the theoretical prediction of electromagnetic waves opening the door to a myriad of new applications in science and technology. In their original form published in 1865., they formed a set of twenty equations, however it was Oliver Heaviside [65] who introduced the concise vector notation and compressed them to the famous four expressions. Maxwell's equations are invariant to the speed of light and consistent with the laws of Einstein's special theory of relativity [66]. It was not until the middle of 20th century that the classical Maxwell's equations have shown to produce inaccuracies on very small scales (below 1nm) and were put in the framework of quantum field theory as a classical limit. In this work, we are interested in the electromagnetic problems around geometries far bigger than 1nm, where classical Maxwell's theory holds.

2.2 Maxwell's equations

Assuming the time-harmonic $e^{j\omega t}$ variation of the fields and sources with the angular frequency ω, we take the Fourier transform of the time-dependent Maxwell's equations converting them to frequency domain expressions which in their symmetric form are

$$\nabla \times \boldsymbol{H} = \boldsymbol{J} + j\omega\epsilon\boldsymbol{E} \tag{2.1}$$

$$\nabla \times \boldsymbol{E} = -\boldsymbol{M} - j\omega\mu\boldsymbol{H} \tag{2.2}$$

$$\nabla \cdot (\epsilon\boldsymbol{E}) = \rho_e \tag{2.3}$$

$$\nabla \cdot (\mu\boldsymbol{H}) = \rho_m \tag{2.4}$$

where $\boldsymbol{H}$ is magnetic field vector (A/m), $\boldsymbol{J}$ is the electric current density vector (A/m^2), $\boldsymbol{E}$ is the electric field vector (V/m), $\boldsymbol{M}$ is the magnetic current density vector (V/m^2), ρ_e is the electric charge density (C/m^3) and ρ_m is the magnetic charge density (Wb/m^3). Magnetic current density and the magnetic charge density are not physical quantities since they have never been observed in nature (so far). They are added to Maxwell's equations in order to symmetrize them and make the mathematical apparatus easier. Furthermore, ϵ is the permittivity of the medium and μ is the permeability of the medium in which the fields and sources are defined. The total electric and magnetic current densities, $\boldsymbol{J}$ and $\boldsymbol{M}$, are defined as a sum of the conduction ($\boldsymbol{J}_c$, $\boldsymbol{M}_c$) and impressed ($\boldsymbol{J}_i$, $\boldsymbol{M}_i$) currents as

$$\boldsymbol{J} = \boldsymbol{J}_i + \boldsymbol{J}_c \tag{2.5}$$

$$\boldsymbol{M} = \boldsymbol{M}_i + \boldsymbol{M}_c \tag{2.6}$$

The conduction currents are induced in the materials due to the fields as follows

$$\boldsymbol{J}_c = \sigma_e \boldsymbol{E} \tag{2.7}$$

$$\boldsymbol{M}_c = \sigma_m \boldsymbol{H} \tag{2.8}$$

where σ_e and σ_m designate the electric and magnetic current conductivities, respectively. Furthermore, the electric and magnetic fields are related to their respective fluxes as

$$\boldsymbol{D} = \epsilon \boldsymbol{E} \tag{2.9}$$

$$\boldsymbol{B} = \mu \boldsymbol{H} \tag{2.10}$$

The equations (2.7)-(2.10) are known as constitutive relations. The constitutive parameters ϵ, μ, σ_e and σ_m can be functions of space (inhomogeneous materials), frequency (dispersive materials), field itself (nonlinear materials), or a tensor (anisotropic materials). In this thesis, with the exception of the chapter dedicated to the analysis of plasmonic nanoparticles, we focus on the linear, isotropic, and piecewise homogeneous materials and therefore the constitutive parameters take the form of a scalar. In the case of the plasmonic effect, the dispersion has to be taken into account since the permittivity of the material is frequency dependent.

2.3 Boundary conditions

Maxwell's equations along with constitutive relations describe the fields within a media with specified electrical parameters. However, on the boundary (Γ) between the media with different electrical properties they have to be supplemented with proper boundary conditions. Let us consider two regions filled with media, each with distinctive electrical parameters. Then, on the boundary-surface between the two regions, the following tangential boundary conditions for electric and magnetic fields hold

$$\hat{n} \times (\boldsymbol{E}_1 - \boldsymbol{E}_2) = -\boldsymbol{M}_\Gamma \tag{2.11}$$

$$\hat{n} \times (\boldsymbol{H}_1 - \boldsymbol{H}_2) = \boldsymbol{J}_\Gamma \tag{2.12}$$

where $\boldsymbol{J}_\Gamma$ and $\boldsymbol{M}_\Gamma$ are electric and magnetic surface current densities at the boundary-surface between the regions. The unit normal $\hat{n}$ is oriented from region 2 to region 1 (see Fig 2.1). Furthermore, we define the normal boundary conditions for electric and magnetic fields at the interface

$$\hat{n} \cdot (\epsilon_1 \boldsymbol{E}_1 - \epsilon_2 \boldsymbol{E}_2) = \rho_{e,\Gamma} \tag{2.13}$$

$$\hat{n} \cdot (\mu_1 \boldsymbol{H}_1 - \mu_2 \boldsymbol{H}_2) = \rho_{m,\Gamma} \tag{2.14}$$

where $\rho_{e,\Gamma}$ and $\rho_{m,\Gamma}$ are electric and magnetic surface charge densities on the interface between the regions. These boundary conditions can be derived by applying integral forms of Maxwell's equations to the infinitesimally small surfaces or volumes defined at the interface of two mediums (see for example [67]).

2.4 Potentials and field representations

In this section, we will derive the expressions for the electric and magnetic fields due to the sources, currents and charges. We assume the medium is linear and isotropic, and the conductivities are equal to zero, i.e. $\sigma_e = \sigma_m = 0$. In the absence of magnetic sources, the magnetic field is solenoidal and the following statement holds

$$\nabla \times \boldsymbol{A} = \boldsymbol{H} \tag{2.15}$$

where the vector function $\boldsymbol{A}$ is magnetic vector potential, and we used the fact that $\nabla \cdot (\nabla \times \boldsymbol{A}) = 0$. Next, we take the second Maxwell's equation (2.2), and by interchanging $\boldsymbol{H}$ with $\nabla \times \boldsymbol{A}$ we get

$$\nabla \times (\boldsymbol{E} + j\omega\mu\boldsymbol{A}) = 0 \tag{2.16}$$

Now we can define the electric scalar potential Φ_e as

$$-\nabla\Phi_e = \boldsymbol{E} + j\omega\mu\boldsymbol{A} \tag{2.17}$$

exploiting the fact that $\nabla \times (\nabla\Phi_e) = 0$. Inserting the definitions of the potentials to (2.1) and using the identity $\nabla \times \nabla \times \boldsymbol{A} = \nabla\nabla \cdot \boldsymbol{A} - \nabla^2\boldsymbol{A}$ we get

$$\nabla\nabla \cdot \boldsymbol{A} - \nabla^2\boldsymbol{A} - k^2\boldsymbol{A} = \boldsymbol{J}_i - j\omega\epsilon\nabla\Phi_e \tag{2.18}$$

where $k = \omega\sqrt{\epsilon\mu}$ is the wave number of the medium.
In order to simplify (2.18), we prescribe the divergence of magnetic vector potential to be $\nabla \cdot \boldsymbol{A} = -j\omega\epsilon\Phi_e$ which is called the Lorenz gauge condition in literature. By inserting the Lorenz gauge condition in (2.18), we get

$$\nabla^2\boldsymbol{A} + k^2\boldsymbol{A} = -\boldsymbol{J}_i. \tag{2.19}$$

Furthermore, by taking the divergence of (2.17) and using the Lorenz gauge condition in combination with (2.3) we have

$$\nabla^2\Phi_e + k^2\Phi_e = -\frac{\rho_e}{\epsilon} \tag{2.20}$$

Equations (2.19) and (2.20) are called the wave equations for electromagnetic potentials, and their solutions can be given in terms of the convolution of the sources (impressed electric currents and electric charges) with the appropriate Green's function of the medium as follows

$$\boldsymbol{A} = \iiint_V \boldsymbol{J}_i(\boldsymbol{r}')GdV \tag{2.21}$$

$$\Phi_e = \frac{1}{\epsilon}\iiint_V \rho_e(\boldsymbol{r}')GdV \tag{2.22}$$

where $R = |\boldsymbol{r} - \boldsymbol{r}'|$ is the distance between the source point $\boldsymbol{r}'$ and the field point $\boldsymbol{r}$, and G is the Green's function, the fundamental solution of the scalar Helmholtz equation

$$G(\boldsymbol{r}, \boldsymbol{r}') = \frac{e^{-jkR}}{4\pi R}, \quad R = |\boldsymbol{r} - \boldsymbol{r}'| \tag{2.23}$$

If we assume there are no electric sources, the analogous procedure leads to the definition of electric vector potential $\boldsymbol{F}$ and magnetic scalar potential Φ_m as follows

$$\boldsymbol{F} = \iiint_V \boldsymbol{M}_i(\boldsymbol{r}')GdV \tag{2.24}$$

$$\Phi_m = \frac{1}{\mu}\iiint_V \rho_m(\boldsymbol{r}')GdV. \tag{2.25}$$

Now, by exploiting the superposition theorem, we can express the electric and magnetic fields in terms of their excitations, currents and charges in the form of mixed potential representations

$$\boldsymbol{E} = -\nabla \times \boldsymbol{F} - j\omega\mu\boldsymbol{A} - \nabla\Phi_e \tag{2.26}$$

$$\boldsymbol{H} = \nabla \times \boldsymbol{A} - j\omega\epsilon\boldsymbol{F} - \nabla\Phi_m \tag{2.27}$$

where the electromagnetic potentials are related to the sources with the expressions (2.21) - (2.25). If the sources are distributed on the surfaces or lines, than the corresponding volumetric integrals in (2.21), (2.22) and (2.24), (2.25) reduce to surface or line integrals, respectively.

2.5 Surface equivalence theorem

The surface equivalence theorem is a natural consequence of the second Green's vector identity applied to the vector Helmholtz equations for the fields (complete derivation is reproduced in, for example, [68]). Without loss of generality, let us assume the problem of the electromagnetic scattering from a penetrable target illuminated by a plane wave (see Fig. 2.1). The surface equivalence theorem breaks the original physical problem into two equivalent problems. The first equivalent problem states that the total physical

fields inside the region 1 $(\boldsymbol{E}_1, \boldsymbol{H}_1)$ can be uniquely determined by knowing the sources inside the region 1 $(\boldsymbol{E}_{inc}, \boldsymbol{H}_{inc})$ (in our example the source is the plane wave, but it can be any other source of radiation) and the rotated tangential traces of the total fields $(\hat{n} \times \boldsymbol{E}_1, \hat{n} \times \boldsymbol{H}_1)$ residing on the boundary (Γ) between regions 1 and 2 (see Fig. 2.1). Therefore, the distribution of sources and fields inside region 2 can be arbitrary and does not affect the physical solution of fields inside region 1. If we assume, for example, that fields inside region 2 $(\boldsymbol{E}_2, \boldsymbol{H}_2)$ are zero, then, by invoking the boundary conditions and replacing medium 2 with medium 1, we have

$$\hat{n} \times \boldsymbol{H}_1 = \boldsymbol{J}_{1,\Gamma} \tag{2.28}$$

$$-\hat{n} \times \boldsymbol{E}_1 = \boldsymbol{M}_{1,\Gamma} \tag{2.29}$$

where $\boldsymbol{J}_{1,\Gamma}$ and $\boldsymbol{M}_{1,\Gamma}$ are the equivalent non-physical radiating surface currents and $\hat{n}$ is the unit vector normal pointing from region 2 to region 1. These currents radiate the correct physical scattered fields inside the region 1 and exactly cancel out the incident fields generated inside the region 1 in the volume occupied by region 2. Applying the same rationale to the fields in region 2 we get the other set of equivalent currents, $\boldsymbol{J}_{2,\Gamma}$ and $\boldsymbol{M}_{2,\Gamma}$;

$$-\hat{n} \times \boldsymbol{H}_2 = \boldsymbol{J}_{2,\Gamma} \tag{2.30}$$

$$\hat{n} \times \boldsymbol{E}_2 = \boldsymbol{M}_{2,\Gamma} \tag{2.31}$$

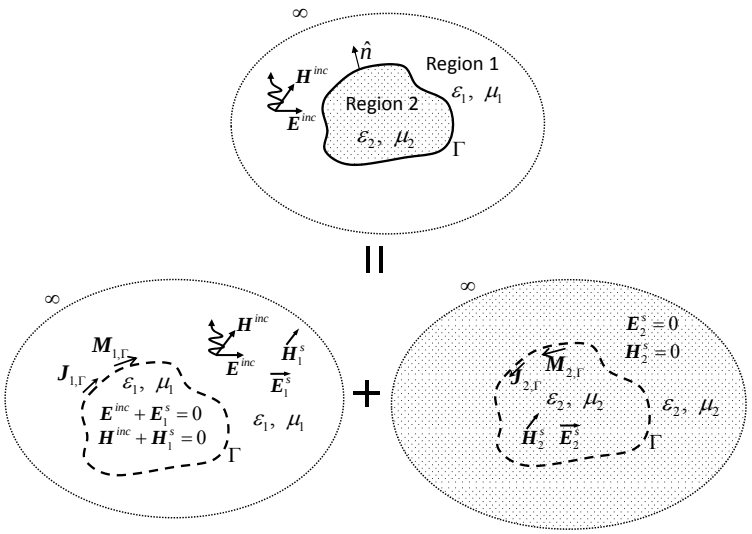

Figure 2.1: Surface equivalence theorem

Analogously to the first equivalent problem, the non-physical equivalent surface currents $\boldsymbol{J}_{2,\Gamma}$ and $\boldsymbol{M}_{2,\Gamma}$ defined in the second equivalent problem radiate the correct physical

scattered fields inside region 2, and zero fields inside region 1 (because we assumed there are no sources inside the region 2). The original physical problem can be viewed as a superposition of two equivalent problems. To reduce the number of unknown equivalent surface currents, we invoke the tangential boundary conditions of the physical problem, relating the equivalent currents as follows

$$\boldsymbol{J}_{1,\Gamma} = -\boldsymbol{J}_{2,\Gamma} \tag{2.32}$$

$$\boldsymbol{M}_{1,\Gamma} = -\boldsymbol{M}_{2,\Gamma} \tag{2.33}$$

which renders the problem uniquely solvable. In the following, we will omit the subscript Γ from the definition of the equivalent current densities, assuming they are surface or line current densities, which will be clear from the context.

2.6 Electromagnetic surface integral equations

With the mixed potential representations of the fields and the surface equivalence theorem at hand, we proceed to the derivation of the most important surface integral equations. Without loss of generality, consider an arbitrarily shaped homogeneous and isotropic target with orientable Lipschitz surface (Γ) and electrical parameters (ϵ_2, μ_2) embedded in a surrounding medium (usually free-space) with parameters (ϵ_1, μ_1). The time-harmonic electromagnetic field ($\boldsymbol{E}^{inc}$, $\boldsymbol{H}^{inc}$) with angular frequency ω is impinging upon the target and the unit normal vector $\hat{n}$ is oriented outwards, (see Fig. 2.1). To this end, we introduce two tangential trace operators, the *rotated tangential trace operator* γ_r and the *tangential trace operator* γ_t which act on an arbitrary vector function $\boldsymbol{F}$ as follows [18]

$$\gamma_t \boldsymbol{F} = -\hat{n} \times \hat{n} \times \boldsymbol{F} \tag{2.34}$$

$$\gamma_r \boldsymbol{F} = \hat{n} \times \boldsymbol{F} \tag{2.35}$$

We proceed by replacing the physical problem with the two equivalent problems by virtue of the surface equivalence theorem and use the tangential boundary conditions for the total electric and magnetic fields, (2.11) and (2.12), applied to each of the equivalent problems. Then, the following statements for the first equivalent problem hold

$$\gamma_t \boldsymbol{E}^{inc} = \gamma_r \boldsymbol{M}_1 + \gamma_t(\nabla \times \boldsymbol{F}_1 + j\omega\mu_1 \boldsymbol{A}_1 + \nabla\Phi_{e,1}) \tag{2.36}$$

$$-\gamma_t \boldsymbol{H}^{inc} = \gamma_r \boldsymbol{J}_1 + \gamma_t(\nabla \times \boldsymbol{A}_1 - j\omega\epsilon_1 \boldsymbol{F}_1 - \nabla\Phi_{m,1}) \tag{2.37}$$

where we have used the fact that the total fields in region 1, ($\boldsymbol{E}_1$, $\boldsymbol{H}_1$) are the sum of the incident fields ($\boldsymbol{E}^{inc}$, $\boldsymbol{H}^{inc}$) and the scattered fields ($\boldsymbol{E}_1^s$, $\boldsymbol{H}_1^s$) which in turn are generated by the equivalent currents ($\boldsymbol{J}_1$, $\boldsymbol{M}_1$).
Analogously, for the second equivalent problem we may write

$$0 = \gamma_r \boldsymbol{M}_2 - \gamma_t(\nabla \times \boldsymbol{F}_2 + j\omega\mu_2 \boldsymbol{A}_2 + \nabla\Phi_{e,2}) \tag{2.38}$$

$$0 = \gamma_r \boldsymbol{J}_2 - \gamma_t(\nabla \times \boldsymbol{A}_2 - j\omega\epsilon_2 \boldsymbol{F}_2 - \nabla\Phi_{m,2}) \tag{2.39}$$

where the total fields in region 2 ($\boldsymbol{E}_2$, $\boldsymbol{H}_2$) are equal to scattered fields ($\boldsymbol{E}_2^s$, $\boldsymbol{H}_2^s$) which are radiated by the equivalent currents ($\boldsymbol{J}_2$, $\boldsymbol{M}_2$).
Summing the equations (2.36) with (2.38), and (2.37) with (2.39), and using the Lorenz gauge condition in order to express scalar potentials through vector potentials, we arrive to the PMCHWT integral formulation

$$-\gamma_t \boldsymbol{E}^{inc} = \sum_{i=1}^{2} \gamma_t \big[\frac{\eta_i}{jk_i}(k_i^2 \boldsymbol{A}_i + \nabla\nabla\cdot\boldsymbol{A}_i)\big] - \gamma_t(\nabla\times\boldsymbol{F}_i) \tag{2.40}$$

$$-\gamma_t \boldsymbol{H}^{inc} = \sum_{i=1}^{2} \gamma_t \big[\frac{1}{j\eta_i k_i}(k_i^2 \boldsymbol{F}_i + \nabla\nabla\cdot\boldsymbol{F}_i)\big] + \gamma_t(\nabla\times\boldsymbol{A}_i) \tag{2.41}$$

where k_i is the wave number of medium i associated to the region i, $\eta_i = \sqrt{\mu_i\epsilon_i}$ is the impedance of the medium i, and we have used the fact that $\boldsymbol{J} = \boldsymbol{J}_1 = -\boldsymbol{J}_2$ and $\boldsymbol{M} = \boldsymbol{M}_1 = -\boldsymbol{M}_2$. Furthermore, we can write equations (2.40) and (2.41) in the form using integral operators as follows

$$-\gamma_t \boldsymbol{E}^{inc} = \sum_{i=1}^{2} \gamma_t \eta_i \boldsymbol{\mathcal{T}}_i - \gamma_t \boldsymbol{\mathcal{K}}_i \tag{2.42}$$

$$-\gamma_t \boldsymbol{H}^{inc} = \sum_{i=1}^{2} \gamma_t \frac{1}{\eta_i} \boldsymbol{\mathcal{T}}_i + \gamma_t \boldsymbol{\mathcal{K}}_i \tag{2.43}$$

where $\boldsymbol{\mathcal{T}}_i$ is the electric field integral operator (EFIO) defined as

$$\boldsymbol{\mathcal{T}}_i = \frac{1}{jk_i}\big[\nabla\nabla\cdot\iint_\Gamma G_i(\boldsymbol{r},\boldsymbol{r}')\boldsymbol{X}(\boldsymbol{r}')d\Gamma + k_i^2\iint_\Gamma G_i(\boldsymbol{r},\boldsymbol{r}')\boldsymbol{X}(\boldsymbol{r}')d\Gamma\big] \tag{2.44}$$

and $\boldsymbol{\mathcal{K}}_i$ is the magnetic field integral operator (MFIO) defined as

$$\boldsymbol{\mathcal{K}}_i = \nabla\times\iint_\Gamma G_i(\boldsymbol{r},\boldsymbol{r}')\boldsymbol{X}(\boldsymbol{r}')d\Gamma \tag{2.45}$$

where $\boldsymbol{X}$ is electric or magnetic surface current density and G_i is the Green's function of the medium i defined as

$$G_i(\boldsymbol{r},\boldsymbol{r}') = \frac{e^{-jk_iR}}{4\pi R} \tag{2.46}$$

Integral operators $\boldsymbol{\mathcal{T}}_i$ and $\boldsymbol{\mathcal{K}}_i$ should be interpreted in Cauchy principal value sense if the field point is on the surface of the target.
Let us now consider a special case where region 2 is occupied by PEC. Then, there is only one equivalent problem, which exactly corresponds to the physical problem. Since $\boldsymbol{M} = \boldsymbol{M}_1 = 0$, we are left only with the equivalent electric surface current which is equal to the physical surface electric current, $\boldsymbol{J} = \boldsymbol{J}_1$, induced on the surface of the PEC target. Taking this into consideration and leveraging the tangential boundary conditions for electric and magnetic field, (2.11) and (2.12), we may write

$$-\gamma_t \boldsymbol{E}^{inc} = \gamma_t \eta_1 \boldsymbol{\mathcal{T}}_1 \tag{2.47}$$

$$\gamma_r \boldsymbol{H}^{inc} = \frac{\boldsymbol{J}_1(\boldsymbol{r})}{2} - \gamma_r \boldsymbol{\mathcal{K}}_1 \tag{2.48}$$

and the integral operators are again evaluated in Cauchy principal value sense. The equations (2.47) and (2.48) are the well known electric field integral equation (EFIE) and magnetic field integral equation (MFIE) in the electromagnetic scattering analysis of PEC objects. Both the EFIE and the MFIE are not uniquely solvable for all the frequencies of interest, corresponding to internal resonance frequencies. The common remedy to this problem is to define the combined field integral equation (CFIE) [69] as a linear combination of the EFIE and the MFIE as follows

$$-\alpha\gamma_t \boldsymbol{E}^{inc} + (1-\alpha)\gamma_r \boldsymbol{H}^{inc} = \alpha\gamma_t\eta_1 \boldsymbol{\mathcal{T}}_1 + (1-\alpha)(\frac{\boldsymbol{J}_1(\boldsymbol{r})}{2} - \gamma_r \boldsymbol{\mathcal{K}}_1) \tag{2.49}$$

where the combination factor α is a real number between zero and one (usually $\alpha = 0.5$).

Chapter 3

Conforming Method of Moments Discretization of Surface Integral Equations

3.1 Introduction

We are interested in solving surface integral equations for the unknown surface electric and magnetic currents, $\boldsymbol{J}$ and $\boldsymbol{M}$. Once the currents are known, the fields anywhere in the space can be computed using the mixed potential representations, (2.26) and (2.27), with the special care taken if the field evaluation point is on the surface of the target. However, for most of the problems of practical interest, the surface integral equations introduced in Chapter 2 are not analytically solvable. Instead, we introduce two approximations. First, the surface of the target under analysis is represented as a union of nonoverlapping facets (usually flat), called mesh. Second, we approximate the unknown surface currents with a set of subsectional known basis functions, with the local support on the mesh, weighted with unknown coefficients. The discretized surface integral equations are cast into matrix form by means of testing the tangential field traces with a set of known subsectional testing functions, and the linear system is solved for the unknown coefficients. However, in order for the discretization to be *conforming to the function spaces*, hence with converging solutions in the physical space of the currents, special restrictions have to be put on the choice of basis and testing functions. Indeed, basis functions have to span a finite-dimensional subspace inside the physical space of the currents, and the testing functions have to span the finite-dimensional subspace of the dual of the range of tangential-trace integral operators [12], [42], [43]. Through this thesis, we will slightly abuse the term *nonconforming*, thinking about all the discretizations of surface integral equations that do not satisfy the above-mentioned rule. In this chapter, we will introduce the conforming MoM discretization of the commonly used surface integral equations presented in Chapter 2.

3.2 The mathematical spaces and mapping properties

Here we introduce the natural mathematical spaces of the surface currents (the domain of the integral operators) and of the (rotated) tangential traces of the integral operators (the range space of the tangential trace of integral operators). Since both the current densities and the tangential traces of the integral operators are vector quantities residing on surfaces, their natural mathematical space is the vector Sobolev space of fractional order. The surface electric and magnetic currents, $\boldsymbol{J}$ and $\boldsymbol{M}$, belong to the space $H^{-1/2}(div_\Gamma, \Gamma)$ [35]. Therefore, the basis functions $\boldsymbol{f}_n$ have to belong to that space, i.e. $\boldsymbol{f}_n \in H^{-1/2}(div_\Gamma, \Gamma)$. These are edge-based divergence-conforming basis functions which commonly straddle two adjacent mesh elements, preserving the normal continuity of the currents across them. Next, we define the mapping properties of the (rotated) tangential traces of integral operators

$$\gamma_t \boldsymbol{\mathcal{T}} : H^{-1/2}(div_\Gamma, \Gamma) \rightarrow H^{-1/2}(curl_\Gamma, \Gamma) \tag{3.1}$$

$$\gamma_r \boldsymbol{\mathcal{I}}/2 - \gamma_t \boldsymbol{\mathcal{K}} : H^{-1/2}(div_\Gamma, \Gamma) \rightarrow H^{-1/2}(curl_\Gamma, \Gamma) \tag{3.2}$$

$$\boldsymbol{\mathcal{I}}/2 - \gamma_r \boldsymbol{\mathcal{K}} : H^{-1/2}(div_\Gamma, \Gamma) \rightarrow H^{-1/2}(div_\Gamma, \Gamma) \tag{3.3}$$

where $\boldsymbol{\mathcal{I}}$ is the identity operator. Furthermore, we will assume that we have a mesh at hand, defined as a union of nonoverlapping flat triangular facets $\tilde{\Gamma} = \bigcup_{t=1}^{N_t} S_t$, where N_t is the number of triangular facets on which low-order divergence-conforming RWG basis functions [34] are defined. This mesh has to be geometrically conformal, with all pairs of adjacent facets sharing a single edge, in order for RWG basis functions to be successfully constructed. Equipped with the necessary function spaces, mapping properties of the tangential traces of integral operators, and a conformal mesh, we can proceed to the conforming MoM discretization of the SIE.

3.3 Conforming MoM discretization of the EFIE

We are interested in the scattering analysis of an arbitrarily shaped PEC target with an orientable surface Γ and the unit normal $\hat{n}$ oriented outwards, embedded in the medium with parameters ϵ_1 and μ_1, illuminated by a time-harmonic electromagnetic field ($\boldsymbol{E}^{inc}$, $\boldsymbol{H}^{inc}$). The induced electric current $\boldsymbol{J}$ can be retrieved by solving the EFIE on the meshed boundary $\tilde{\Gamma}$. We proceed by expanding the unknown electric current $\boldsymbol{J}$ with low-order divergence-conforming RWG set $\{\boldsymbol{f}_n\} \in H^{-1/2}(div_\Gamma, \Gamma)$ as follows

$$\boldsymbol{J} \simeq \sum_{n=1}^{N_e} J_n \boldsymbol{f}_n \tag{3.4}$$

where N_e is the number of interior edges arising in the tesselation of the boundary and $\{J_n\}$ is the set of unknown coefficients in the expansion of the current. The RWG basis functions $\{\boldsymbol{f}_n\}$ are defined on interior edges of the mesh [34] as, (see Fig. 3.1)

$$\boldsymbol{f}_n(\boldsymbol{r}') = \begin{cases} \frac{1}{2A_n^1}(\boldsymbol{r}' - \boldsymbol{r}_n^1), & \boldsymbol{r}' \in S_n^1 \\ -\frac{1}{2A_n^2}(\boldsymbol{r}' - \boldsymbol{r}_n^2), & \boldsymbol{r}' \in S_n^2 \end{cases} \tag{3.5}$$

where A_n^1 and A_n^2 denote the areas of the corresponding edge-adjacent triangles, S_n^1 and S_n^2, respectively. The position vectors of the free vertices opposite to the nth edge are designated by $\boldsymbol{r}_n^1$ and $\boldsymbol{r}_n^2$, (see Fig. 3.1). Different to the definition in [34], we do not normalize the basis function with the corresponding edge length l_n.

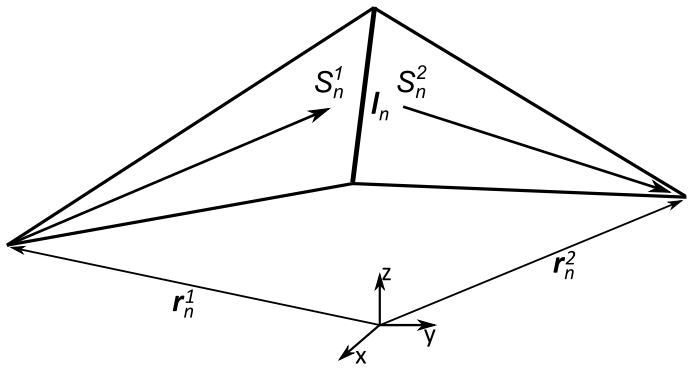

Figure 3.1: RWG basis function defined over two edge adjacent facets

The RWG discretization of the EFIE yields

$$\sum_{n=1}^{N_e} \eta_1 \gamma_t (\boldsymbol{\mathcal{T}}_n^1) J_n = -\gamma_t \boldsymbol{E}^{inc} \tag{3.6}$$

where the discretized EFIO, $\boldsymbol{\mathcal{T}}_n^1$, is defined as

$$\boldsymbol{\mathcal{T}}_n^1 = \frac{1}{jk_1}\left[\nabla\nabla\cdot \iint_{S_n^1 \cup S_n^2} G_1(\boldsymbol{r}, \boldsymbol{r}') \boldsymbol{f}_n(\boldsymbol{r}') dS' + k_1^2 \iint_{S_n^1 \cup S_n^2} G_1(\boldsymbol{r}, \boldsymbol{r}') \boldsymbol{f}_n(\boldsymbol{r}') dS'\right] \tag{3.7}$$

The range space of the tangential trace of the operator $\boldsymbol{\mathcal{T}}$ is $H^{-1/2}(curl_\Gamma, \Gamma)$ (see eq. (3.1)). It is well known that the dual space of the $H^{-1/2}(curl_\Gamma, \Gamma)$ is $H^{-1/2}(div_\Gamma, \Gamma)$ [12], [44] so the good candidates for the testing functions would be RWG basis functions. Proceeding with this justification we transform the discretized EFIE (3.6) into matrix form as

$$\begin{aligned} \iint_{S_m^1 \cup S_m^2} J_n \eta_1 \boldsymbol{\mathcal{T}}_n^1 \cdot \boldsymbol{f}_m(\boldsymbol{r}) dS = -\iint_{S_m^1 \cup S_m^2} \boldsymbol{E}^{inc} \cdot \boldsymbol{f}_m(\boldsymbol{r}) dS, \\ 1 \leqslant m \leqslant N_e, \\ 1 \leqslant n \leqslant N_e \end{aligned} \tag{3.8}$$

The discretization shown in (3.8) is dubbed Galerkin MoM discretization since the basis and the testing functions are the same. Apart from being conforming to the natural function spaces, divergence-conforming Galerkin MoM discretization of the EFIE is especially convenient since the hypersingular part of the EFIO (first term on the right hand side of

(3.7)) can be transformed into an integral with weakly singular kernel by virtue of the Green's identity. The EFIE can be applied on closed or open surfaces.

3.4 Conforming MoM discretization of the MFIE and the CFIE

Alternatively, if the boundary of the PEC target Γ is closed, the unknown electric current $\boldsymbol{J}$ can be obtained by solving the MFIE or the CFIE. We proceed by approximating the unknown electric current with RWG basis functions as in (3.4). Then, the RWG discretization of the MFIE yields

$$\sum_{n=1}^{N_e} \frac{J_n}{2} \boldsymbol{f}_n(\boldsymbol{r}) - \sum_{n=1}^{N_e} \gamma_r(\boldsymbol{\mathcal{K}}_n^1) J_n = \gamma_r \boldsymbol{H}^{inc} \tag{3.9}$$

where the discretized MFIO $\boldsymbol{\mathcal{K}}_n^1$ is defined as

$$\boldsymbol{\mathcal{K}}_n^1 = \nabla \times \iint_{S_n^1 \cup S_n^2} G_1(\boldsymbol{r}, \boldsymbol{r}') \boldsymbol{f}_n(\boldsymbol{r}') dS' \tag{3.10}$$

Using the mapping properties defined in (3.3) we can deduce that the range space of the rotated tangential trace of the MFIO is $H^{-1/2}(div_\Gamma, \Gamma)$ and therefore the dual of the range space is $H^{-1/2}(curl_\Gamma, \Gamma)$. Naively we could assume that the convenient testing functions would be $\tilde{\boldsymbol{f}}_m = \hat{n} \times \boldsymbol{f}_m$ since $\tilde{\boldsymbol{f}}_m \in H^{-1/2}(curl_\Gamma, \Gamma)$. However, this choice would lead to the singular Gram matrix and the ill-conditioned linear system. The commonly used RWG-Galerkin discretization of the MFIE leads to the following statements

$$\begin{aligned} &\iint_{S_m^1 \cup S_m^2} \frac{J_n}{2} \boldsymbol{f}_m(\boldsymbol{r}) \boldsymbol{f}_n(\boldsymbol{r}) dS - \iint_{S_m^1 \cup S_m^2} J_n \gamma_r(\boldsymbol{\mathcal{K}}_n^1) \cdot \boldsymbol{f}_m(\boldsymbol{r}) dS = \\ &\iint_{S_m^1 \cup S_m^2} \gamma_r \boldsymbol{H}^{inc} \cdot \boldsymbol{f}_m(\boldsymbol{r}) dS, \quad 1 \leqslant m \leqslant N_e, \quad 1 \leqslant n \leqslant N_e \end{aligned} \tag{3.11}$$

However, this RWG-Galerkin discretization of the MFIE is not conforming with respect to the aforementioned mapping properties. To obtain the conforming discretization of the MFIE, a new set of testing functions is needed. These are Buffa-Christiansen (BC) basis functions $\{\boldsymbol{g}_m\}$ [70], [13]. These functions are divergence-conforming by its construction, but also quasi curl-conforming in the sense that the Gram matrix linking the rotated BC basis functions $\tilde{\boldsymbol{g}}_m = \hat{n} \times \boldsymbol{g}_m$ and the RWG basis functions $\boldsymbol{f}_m$ is well conditioned [13]. We proceed with the *mixed* discretization of the MFIE [12] as follows

$$\begin{aligned} &\iint_{D_m} \frac{J_n}{2} \tilde{\boldsymbol{g}}_m(\boldsymbol{r}) \boldsymbol{f}_n(\boldsymbol{r}) dS - \iint_{D_m} J_n \gamma_r(\boldsymbol{\mathcal{K}}_n^1) \cdot \tilde{\boldsymbol{g}}_m(\boldsymbol{r}) dS = \\ &\iint_{D_m} \gamma_r \boldsymbol{H}^{inc} \cdot \tilde{\boldsymbol{g}}_m(\boldsymbol{r}) dS, \quad 1 \leqslant m \leqslant N_e, \quad 1 \leqslant n \leqslant N_e \end{aligned} \tag{3.12}$$

where D_m is the domain on which the mth rotated BC testing function is defined. It was shown in [12] that the mixed conforming discretization of the MFIE produces more accurate results than the frequently used Galerkin RWG discretization.

The commonly used Galerkin RWG implementation of the CFIE is also not conforming with respect to the mapping properties, since the rotated tangential trace of the MFIO is not well tested. Instead, mixed discretization of the MFIE (3.12) is adopted together with the Galerkin RWG discretization of the EFIE resulting in the conforming low order mixed discretization of the CFIE as follows

$$\begin{aligned}(1-\alpha)\left(\iint_{D_m}\frac{J_n}{2}\tilde{\boldsymbol{g}}_m(\boldsymbol{r})\boldsymbol{f}_n(\boldsymbol{r})dS-\iint_{D_m}J_n\gamma_r(\boldsymbol{\mathcal{K}}_n^1)\cdot\tilde{\boldsymbol{g}}_m(\boldsymbol{r})dS\right)+\\ \alpha\iint_{S_m^1\cup S_m^2}J_n\eta_1\boldsymbol{\mathcal{T}}_n^1\cdot\boldsymbol{f}_m(\boldsymbol{r})dS=(1-\alpha)\left(\iint_{D_m}\gamma_r\boldsymbol{H}^{inc}\cdot\tilde{\boldsymbol{g}}_m(\boldsymbol{r})dS\right)\\ -\alpha\iint_{S_m^1\cup S_m^2}\boldsymbol{E}^{inc}\cdot\boldsymbol{f}_m(\boldsymbol{r})dS,\quad 1\leqslant m\leqslant N_e,\quad 1\leqslant n\leqslant N_e\end{aligned}\tag{3.13}$$

3.5 Conforming MoM discretization of the PMCHWT

Let us consider the scattering analysis of an arbitrary shaped penetrable target with orientable surface Γ and electrical parameters (ϵ_2, μ_2) immersed in the medium with parameters (ϵ_1, μ_1). The time-harmonic electromagnetic wave ($\boldsymbol{E}^{inc}$, $\boldsymbol{H}^{inc}$) is impinging upon the homogeneous obstacle, and the unit normal $\hat{n}$ is oriented outwards (see Fig. 2.1). We approximate the equivalent electric and magnetic currents with the weighted sum of the RWG basis functions defined on a triangulation $\tilde{\Gamma}$ analogously to the expansion performed in (3.4) for PEC targets.
The RWG discretization of the PMCHWT reads

$$\sum_{n=1}^{N_e}\sum_{i=1}^{2}\gamma_t\eta_i\boldsymbol{\mathcal{T}}_n^iJ_n-\sum_{n=1}^{N_e}\sum_{i=1}^{2}\gamma_t\boldsymbol{\mathcal{K}}_n^iM_n=-\gamma_t\boldsymbol{E}^{inc}\tag{3.14}$$

$$\sum_{n=1}^{N_e}\sum_{i=1}^{2}\gamma_t\boldsymbol{\mathcal{K}}_n^iJ_n+\sum_{n=1}^{N_e}\sum_{i=1}^{2}\gamma_t\frac{1}{\eta_i}\boldsymbol{\mathcal{T}}_n^iM_n=-\gamma_t\boldsymbol{H}^{inc}\tag{3.15}$$

where the discretized operators $\boldsymbol{\mathcal{T}}_n^i$ and $\boldsymbol{\mathcal{K}}_n^i$ are defined according to equations (3.7) and (3.10), respectively, by setting the proper values for the wave number and the impedance of the region i ($i=1,2$). The sets of unknown coefficients in the expansion of the electric and magnetic currents are designated as $\{J_n\}$ and $\{M_n\}$, respectively. The range space of the tangential traces of the involved integral operators is $H^{-1/2}(curl_\Gamma,\Gamma)$, (3.1), (3.2), so the testing should be done in $H^{-1/2}(div_\Gamma,\Gamma)$ [45]. Therefore, the Galerkin RWG MoM discretization of the PMCHWT excels as low order conforming scheme and leads to the following linear system

$$\begin{aligned}\sum_{i=1}^{2}\iint_{S_m^1\cup S_m^2}J_n\eta_i\boldsymbol{\mathcal{T}}_n^i\cdot\boldsymbol{f}_m(\boldsymbol{r})dS-\sum_{i=1}^{2}\iint_{S_m^1\cup S_m^2}M_n\boldsymbol{\mathcal{K}}_n^i\cdot\boldsymbol{f}_m(\boldsymbol{r})dS=\\ -\iint_{S_m^1\cup S_m^2}\boldsymbol{E}^{inc}\cdot\boldsymbol{f}_m(\boldsymbol{r})dS,\quad 1\leqslant m\leqslant N_e,\quad 1\leqslant n\leqslant N_e\end{aligned}\tag{3.16}$$

$$\sum_{i=1}^{2} \iint_{S_m^1 \cup S_m^2} J_n \boldsymbol{\mathcal{K}}_n^i \cdot \boldsymbol{f}_m(\boldsymbol{r}) dS + \sum_{i=1}^{2} \iint_{S_m^1 \cup S_m^2} M_n \frac{1}{\eta_i} \boldsymbol{\mathcal{T}}_n^i \cdot \boldsymbol{f}_m(\boldsymbol{r}) dS = - \iint_{S_m^1 \cup S_m^2} \boldsymbol{H}^{inc} \cdot \boldsymbol{f}_m(\boldsymbol{r}) dS, \quad 1 \leqslant m \leqslant N_e, \quad 1 \leqslant n \leqslant N_e \tag{3.17}$$

3.6 Remarks

Conforming discretizations of surface integral equations guarantee the convergence of the numerical approximation to the physical solution as the number of unknowns rises [18]. This does not hold for nonconforming discretizations. In the implementation of a numerical scheme, we are limited by memory resources and the CPU time, which set an upper bound on the number of unknowns in the approximation of currents. Therefore, in this *discretized space* we are searching for the most accurate solution possible. It has been observed by Ylä-Oijala et al. [42] that conforming solutions may not always be the most accurate for a fixed number of unknowns. For example, the conforming MoM Galerkin discretization of the EFIE with BC basis functions has shown to produce results of very poor accuracy because of the inadequate modelling of the charge. On the contrary, other nonconforming strategies have proven to be very accurate especially in the analysis of objects with sharp edges and corners where singular fields are induced. For example, the Galerkin discretization of the MFIE with discontinuous-across-edges monopolar-RWG basis functions introduced by Ubeda and Rius [11] perform close to the conforming RWG Galerkin discretization of the EFIE in the analysis of electrically small sharp-edged targets. Similar observations were made with Galerkin MoM discretization of the MFIE with low order curl conforming basis functions [11], [71]. Therefore, as we will show in the next three chapters, a cleverly crafted nonconforming discretization of surface integral equations may produce a more accurate result than the corresponding conforming discretization for the fixed number of degrees of freedom.

Chapter 4

Discontinuous Method of Moments Discretization of Integral Equations Applied to 2D Problems

4.1 Introduction

The discretization by the method of moments and Galerkin testing of, respectively, the electric field integral equation [34], for single perfectly conducting objects, or the Poggio–Miller–Chang–Harrington–Wu–Tsai formulation [19]– [21], for single penetrable objects, is traditionally based on low order divergence-conforming functions, e.g., Rao-Wilton-Glisson basis functions [34], [72], so that normal continuity is preserved across edges. In the particular case of infinitely long (2D) bodies, these implementations are normally carried out with continuous piecewise linear basis functions [73], [74]. These are node-based strategies because the basis functions embrace two adjacent cells in the meshed boundary. Moreover, these schemes are conforming, hence with converging solutions [44], [45], because the finite dimensional subspace in the current expansion lies in the physical function space and the testing functions span the dual of the range of tangential trace integral operators [12], [42]. The divergence-conforming choice is especially advantageous for the computation of the impedance matrix because of the cancellation of the hypersingular kernel contributions. In practice, these schemes can be extended naturally to the scattering analysis of composite objects, made up of different homogeneous regions, PEC or penetrable, as long as there are no junctions, such as coated metallic objects or multi-layered penetrable structures [75], [76]. Junctions stand for boundary lines where more than two regions intersect [46]- [50]. In general, for an arbitrary composite object, they are modelled with edges (nodes in 2D).

However, the development of conforming schemes for composite objects with junctions becomes somewhat awkward because continuity conditions need to be applied at junctions through specially tailored functions [46]- [50]. The conventional MoM-codes are then modified accordingly by inserting exceptions at junctions. This is a somewhat convoluted task that involves the search for junctions, the identification of the regions intersecting at each junction, and the choice of the appropriate continuity condition (metallic-penetrable or penetrable). In any case, these single-surface (or single-trace) approaches have been successful for decades in the analysis of composite structures despite the involved search of junctions and the required identification of the number and type (metallic or penetrable)

of intersecting regions at each junction. More recently, other so-called *two-surface* [51] or *multi-trace* [52] schemes circumvent the management of junctions by treating the composite object as a set of disjoint objects immersed in a host medium, with the separation distances tending to zero. These schemes provide improved flexibility when managing composite objects but require the definition of additional redundant unknowns on touching surfaces. Clearly, the single-trace approaches were developed in earlier times, with restricted computational resources, such that the definition of additional unknowns was just too costly. Conversely, over the past years, the double-surface and multi-trace schemes have captured the attention of researchers thanks to the dramatic increase of available memory resources. All these schemes suffer from the mesh restrictions imposed by the adopted divergence-conforming sets, which need to be defined over geometrically conformal meshes, with all pairs of adjacent segments sharing a single node. In consequence, the mesh generation of composite objects in the single-trace analysis becomes especially constrained, inadequate to combine arbitrary meshes arising from the independent tessellation of each of the several subdomains that form the original structure.

In this chapter, we present a new, robust, and accurate method for the scattering analysis of 2D piecewise homogeneous objects with junctions, based on the discretization of the EFIE, over boundaries enclosing PEC regions, and of the PMCHWT formulation, over interface boundaries between different penetrable regions. We propose the expansion of the electric and magnetic currents with piecewise linear basis functions, discontinuous at nodes. The resulting EFIE-PMCHWT implementation gives rise to hypersingular kernel contributions, which we evaluate numerically by testing the electric– or magnetic–field equations, in the transversal electric (TE) or transversal magnetic (TM)–implementations over domains off the boundary segmentation, inside the region where, in light of the surface equivalence theorem, the fields must be zero. Whereas the surface scheme tests the fields over a set of trapezoids attached to the boundary, the tangential-normal scheme makes use of a set of pairs of adjacent segments, such that one matches a boundary segment and the other one is quasi-normally oriented. These discretization strategies are nonconforming because the finite-dimensional subspaces of electric and magnetic currents, spanned with discontinuous piecewise linear basis functions, are not the proper subsets of the function spaces of currents. Interestingly, as we will show in this chapter, in the scattering analysis of sharp-edged 2D conductors, nonconforming MoM implementations of the TE-EFIE, based on the discontinuous cell-based expansion of the current exhibit more accurate and faster converging solutions in the near-field or far-field regions than the conventional conforming schemes. Similar observations were made in the scattering analysis of sharp-edged 2D dielectric targets with moderate or high permittivity contrasts or sharp-edged 2D ferromagnetic objects using TE-PMCHWT or TM-PMCHWT, respectively. Furthermore, we show that these TE/TM-EFIE-PMCHWT implementations, with segment-based expansion and testing schemes, excel as flexible and versatile tools in the analysis of composite objects when compared with the conventional node-based implementations. Although our discontinuous EFIE-PMCHWT discretizations rely on an elaborate generation of the impedance elements, the burdensome management of junctions of the conforming schemes is circumvented because only segment-to-segment interactions are considered.

The concepts introduced in this chapter are published in [58].

4.2 Theoretical background

Field singularities arising in the infinitely long sharp PEC wedges, with aperture angle α, ($\alpha < 180^{\circ}$) are associated with the transverse component of the incident field. In the TE scattering analysis of a PEC wedge, the electric charge density becomes singular near the tip of the wedge, while the electric current stays bounded [77]. Conversely, in the TM scattering analysis, the electric current exhibits singular behaviour near the tip of the wedge, while the charge density is equal to zero in the system [77]. These singularities get more pronounced as the wedge becomes sharper. The singular field behaviour around penetrable wedges is more involved. Field singularities arising in infinitely long dielectric or magnetic sharp wedges, are linked with the transverse component of, respectively, the electric or magnetic fields [77]. Singular field performance near penetrable wedges, sharp ($\alpha < 180^{\circ}$) or reentrant ($\alpha > 180^{\circ}$), occurs whenever the transverse field component of the impinging plane wave is, respectively, parallel or perpendicular, to the line bisecting the wedge [77]. In the TE (or TM) scattering analysis of dielectric (or magnetic) sharp wedges, the singularity of the magnetic (or electric) current and the electric (or magnetic) charge density near the wedge becomes more pronounced as the relative permittivity (or permeability) rises for the fixed aperture of the wedge (see [77], [Table 4.2] and [77], [Fig. 4.28]).

As shown in this chapter, our nonconforming discretization of the TE-EFIE for PEC sharp wedges, TE-PMCHWT formulation for dielectric sharp wedges, or, similarly, of the TM-PMCHWT formulation for magnetic sharp wedges, must provide a better capture of the singular electric-field or magnetic-field performance, respectively, than the conventional piecewise continuous scheme because improved accuracy, versus the number of unknowns, is observed. Conversely, the analogous implementations of TM-PMCHWT for dielectric wedges, or of TE-PMCHWT for magnetic wedges, do not provide improved accuracy, versus the number of unknowns, because, consistently, in these cases field singularities do not occur [77]. In any case, all these nonconforming EFIE and PMCHWT implementations, segment-based, are very useful for the agile management of junctions in 2D composite objects.

Several authors characterized the specific behaviour of electromagnetic fields near sharp edges [77], [80]. Several basis functions incorporate the Meixner subsets [79] for the rigorous capture of the singular behaviour of the current near edges in PEC sharp wedges [41], [81]- [83], where the singular coefficients of the singular terms are obtained from the aperture angle of the wedge. The definition of the subsets for penetrable wedges, though, requires the numerical solution of transcendental equations that depend on the aperture angle and the relative permittivity/permeability contrast [77], [80]. The use of our discontinuous piecewise linear schemes in these cases appears as a robust option because, unlike the elaborate singular-field implementations with the Meixner subsets, our approach does not require the *a priori* knowledge of aperture angles or the relative contrasts of the body.

4.3 Discontinuous discretization of TE-EFIE for conductors

For a z-infinite PEC closed body illuminated by a TE plane wave, the expansion of the electric current $\boldsymbol{J}$ with a set of discontinuous piecewise linear basis functions gives rise to

$$\boldsymbol{J} \simeq \sum_{n=1}^{N_s} \sum_{p=1}^{2} J_n^p \boldsymbol{f}_n^p \tag{4.1}$$

where N_s denotes the number of segments over the transversal boundary of the body. The sequences $\{J_n^1\}$ and $\{J_n^2\}$ denote the unknown coefficients in the expansion of the electric current. The sets of discontinuous basis functions $\{\boldsymbol{f}_1^1 ... \boldsymbol{f}_{N_s}^1, \boldsymbol{f}_1^2 ... \boldsymbol{f}_{N_s}^2\}$ are defined as

$$\boldsymbol{f}_n^p(\boldsymbol{\rho}') = \frac{1}{h_n}(\boldsymbol{\rho}' - \boldsymbol{\rho}_n^p), \quad \boldsymbol{\rho}' \in L_n \quad p = 1, 2 \tag{4.2}$$

where L_n stands for the nth segment arising from the boundary segmentation, with length h_n, and $\boldsymbol{\rho}_n^1$ and $\boldsymbol{\rho}_n^2$ represent the position vectors of the endpoints of L_n (see Fig. 4.1)

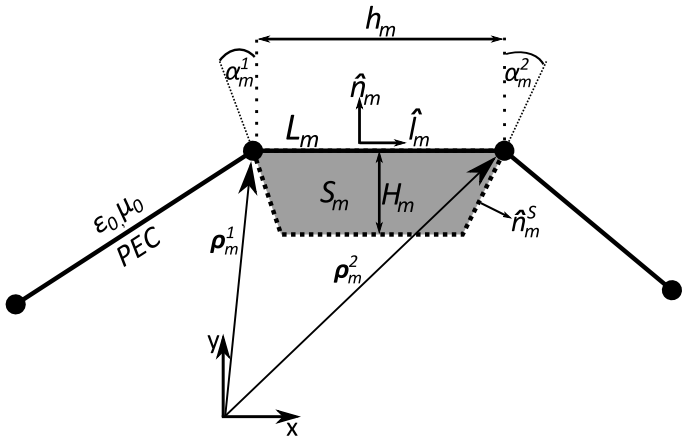

Figure 4.1: mth segment arising from the discretized section of an infinitely long PEC cylinder where the surface testing scheme is defined conformal to the boundary

The approximation of the TE scattered electric field from the expansion of $\boldsymbol{J}$ in (4.1) yields

$$\boldsymbol{E}^S \simeq -jk\eta \sum_{n=1}^{N_s} \sum_{p=1}^{2} J_n^p \boldsymbol{A}_n^p(\boldsymbol{\rho}) - \sum_{n=1}^{N_s} \sum_{p=1}^{2} J_n^p \nabla \Phi_n^p(\boldsymbol{\rho}) \tag{4.3}$$

where k and η denote, respectively, the wave number and the impedance of the host medium, where the object is immersed. The two source contributions ($p = 1, 2$) at the nth segment in the discretization of the potentials Φ_n^p and $\boldsymbol{A}_n^p$ yield

$$\boldsymbol{A}_n^p(\boldsymbol{\rho}) = \int_{L_n} G_k(\boldsymbol{\rho}, \boldsymbol{\rho}') \boldsymbol{f}_n^p(\boldsymbol{\rho}') dl' \tag{4.4}$$

$$\Phi_n^p(\boldsymbol{\rho}) = j\frac{\eta}{k}\Big[\int_{L_n} G_k(\boldsymbol{\rho},\boldsymbol{\rho}')dl' - G_k(\boldsymbol{\rho},\boldsymbol{\rho}_n^{p+1})\Big] \tag{4.5}$$

where the superscript in (4.5) assumes modulo two arithmetic. The Green's function G_k of the host medium is defined as

$$G_k(\boldsymbol{\rho},\boldsymbol{\rho}') = \frac{1}{4j}H_0^{(2)}(kR), \quad R = |\boldsymbol{\rho}-\boldsymbol{\rho}'| \tag{4.6}$$

where $k = \omega/\sqrt{\mu\epsilon}$, $\eta = \sqrt{\mu/\epsilon}$, and ω denotes the angular frequency in the $e^{j\omega t}$ time-harmonic dependence assumed for fields and currents. The constants ϵ and μ denote the permittivity and the permeability, respectively, of the host medium (usually free space). The Galerkin testing of the gradient of the electric scalar potential $\nabla\Phi_n^p$ in (4.5) cannot be evaluated numerically for self or node-adjacent interactions because of the unbounded contributions in $\nabla G_k(\boldsymbol{\rho},\boldsymbol{\rho}_n^{p+1})$, behaving as $\mathcal{O}(|\boldsymbol{\rho}-\boldsymbol{\rho}_n^{p+1}|^{-1})$ when the field point approaches the endpoints of the segment. In this chapter, we present two non-Galerkin testing schemes that ensure a proper numerical evaluation of such contributions by testing transverse components of the fields inside the body under analysis, off the boundary line. These testing functions are devised to have a good coupling with the fields generated by the discontinuous piecewise linear basis functions.

4.3.1 Surface testing

The surface testing is carried out over a set of quadrilaterals $\{S_m\}$ attached to the set of segments over the boundary $\{L_m\}$, inside the region where the fields are zero (Fig. 4.1). The quadrilaterals can be defined either *conformal* or *nonconformal* to the boundary. Whereas the former establishes trapezoids with two sides parallel to the matching segments and with two sides bisecting the angles formed by the adjacent segments, the latter adopts rectangles. This definition appears more flexible because no *a priori* knowledge of the boundary shape is required. For segments with a node lying on an abrupt sharp edge, though, the testing rectangle may break out of the boundary interface and some numerical error may appear.
We define the set of surface testing functions $\{\boldsymbol{P}_1^1 ... \boldsymbol{P}_{N_s}^1, \boldsymbol{P}_1^2 ... \boldsymbol{P}_{N_s}^2\}$ as

$$\boldsymbol{P}_m^q(\boldsymbol{\rho}) = \frac{1}{H_m h_m}\Big[(\boldsymbol{\rho}-\boldsymbol{\rho}_m^q)\cdot\hat{l}_m\Big]\cdot\hat{l}_m + (-1)^q\frac{1}{H_m h_m}\Big[(\boldsymbol{\rho}_m^q-\boldsymbol{\rho})\cdot\hat{n}_m\Big]\tan\alpha_m^q\cdot\hat{l}_m, \tag{4.7}$$
$$\boldsymbol{\rho}\in S_m \quad q=1,2 \quad 1\leqslant m\leqslant N_s$$

where H_m denotes the height of the mth quadrilateral, and $\hat{n}_m$ and $\hat{l}_m$ represent, respectively, the unit normal and tangential vectors to the mth segment. The parameters α_m^1 and α_m^2 denote the angles of the sides of the quadrilaterals meeting the endpoints of the mth segment, respectively, $\boldsymbol{\rho}_m^1$, $\boldsymbol{\rho}_m^2$, with respect to the normal direction to the segment. For testing elements that are nonconformal to the boundary, these sides are perpendicular to the segment, whereby $\alpha_m^1 = \alpha_m^2 = 0$ and the second term in (4.7) gets canceled.
The surface tested nonconforming discretization of the TE-EFIE results in the following matrix system:

$$E_{inc}^{\mathbf{S},[m,q]} = \sum_{n=1}^{N_s} Z_{[n,1]}^{\mathbf{S},[m,q]} J_n^1 + \sum_{n=1}^{N_s} Z_{[n,2]}^{\mathbf{S},[m,q]} J_n^2, \qquad q = 1,2 \quad 1 \leqslant m \leqslant N_s \tag{4.8}$$

where the excitation vector stands for

$$E_{inc}^{\mathbf{S},[m,q]} = \iint_{S_m} \boldsymbol{P}_m^q(\boldsymbol{\rho}) \cdot \boldsymbol{E}_{inc}(\boldsymbol{\rho}) dS \tag{4.9}$$

and $\boldsymbol{E}_{inc}(\boldsymbol{\rho})$ denotes the incident TE-electric field. The definition of the impedance elements in 4.8 yields

$$Z_{[n,p]}^{\mathbf{S},[m,q]} = jk\eta \iint_{S_m} \boldsymbol{P}_m^q(\boldsymbol{\rho}) \cdot \boldsymbol{A}_n^p(\boldsymbol{\rho}) dS + \iint_{S_m} \boldsymbol{P}_m^q(\boldsymbol{\rho}) \cdot \nabla \Phi_n^p(\boldsymbol{\rho}) dS \tag{4.10}$$

where, for self- or node-adjacent interactions, the second surface integral at the right-hand side can manage the singular terms in $\nabla\Phi_n^p$ because an extra degree of freedom is incorporated with respect to the Galerkin scheme. In our implementation, we compute (4.10), equivalently, as

$$Z_{[n,p]}^{\mathbf{S},[m,q]} = jk\eta \iint_{S_m} \boldsymbol{P}_m^q(\boldsymbol{\rho}) \cdot \boldsymbol{A}_n^p(\boldsymbol{\rho}) dS + \int_{\partial S_m} \Phi_n^p(\boldsymbol{\rho}) \boldsymbol{P}_m^q(\boldsymbol{\rho}) \cdot \hat{n}_m^S dl - \iint_{S_m} \nabla \cdot \boldsymbol{P}_m^q(\boldsymbol{\rho}) \Phi_n^p(\boldsymbol{\rho}) dS \tag{4.11}$$

where $\hat{n}_m^S$ stands for the unit vector normal to the boundary of the rectangular domain S_m and pointing outwards (see Fig. 4.1). All the integrals appearing in (4.11) are with weakly singular kernels, readily computable with existing numerical routines.

4.3.2 Line tangential-normal testing

The line tangential-normal testing is defined over pairs of segments sharing a node arising from the segmentation of the boundary line. Whereas one testing segment matches a cell arising from the boundary segmentation, the other segment is oriented towards the region where the fields, in light of the equivalence principle, are zero (Fig. 4.2). The tangential-normal testing scheme can also be defined conformal or nonconformal to the boundary depending whether the off-boundary segment is aligned over the direction bisecting the angle between adjacent segments or perpendicular to the matching segment.
The definition, with modulo two arithmetic, of the tangential-normal testing functions, $\{\boldsymbol{t}_1^1 ... \boldsymbol{t}_{N_s}^1, \boldsymbol{t}_1^2 ... \boldsymbol{t}_{N_s}^2\}$ yields

$$\boldsymbol{t}_m^q(\boldsymbol{\rho}) = \begin{cases} \frac{1}{h_m}(\boldsymbol{\rho} - \boldsymbol{\rho}_m^q), & \boldsymbol{\rho} \in L_m \\ \frac{1}{h_m^{N,q+1}}(\boldsymbol{\rho}_m^{N,q+1} - \boldsymbol{\rho}), & \boldsymbol{\rho} \in N_m^{q+1} \end{cases} \quad q = 1,2 \quad 1 \leqslant m \leqslant N_s \tag{4.12}$$

where $\boldsymbol{t}_m^1$ and $\boldsymbol{t}_m^2$ represent the two tangential-normal functions sharing the mth segment L_m, and N_m^1 and N_m^2 denote two segments with lengths $h_m^{N,1}$ and $h_m^{N,2}$ evolving inward from the endpoints of L_m, respectively, $\boldsymbol{\rho}_m^1$ and $\boldsymbol{\rho}_m^2$, to $\boldsymbol{\rho}_m^{N,1}$ and $\boldsymbol{\rho}_m^{N,2}$, inside the null-field region (see Fig. 4.2)

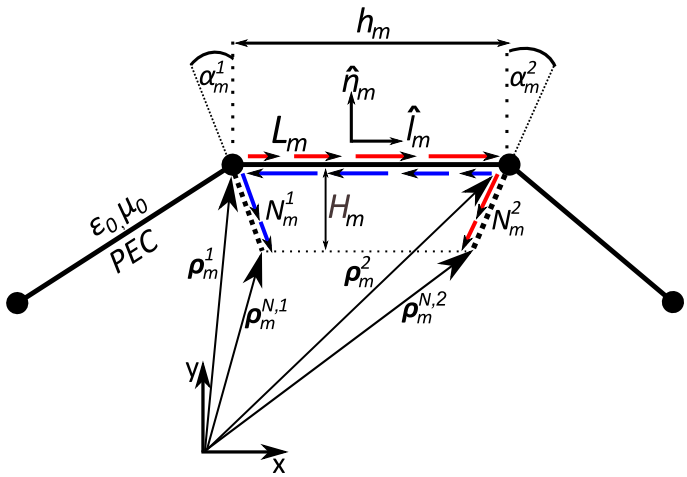

Figure 4.2: mth segment arising from the discretized section of an infinitely long PEC cylinder where the tangential-normal testing scheme is defined conformal to the boundary

The discretization of the TE-EFIE with discontinuous piecewise linear basis functions and tangential-normal testing leads to the following matrix system:

$$E_{inc}^{\mathbf{T},[m,q]} = \sum_{n=1}^{N_s} Z_{[n,1]}^{\mathbf{T},[m,q]} J_n^1 + \sum_{n=1}^{N_s} Z_{[n,2]}^{\mathbf{T},[m,q]} J_n^2, \quad q = 1,2 \quad 1 \leqslant m \leqslant N_s \tag{4.13}$$

where the excitation vector yields

$$E_{inc}^{\mathbf{T},[m,q]} = \int\limits_{L_m \cup N_m^{q+1}} \boldsymbol{t}_m^q(\boldsymbol{\rho}) \cdot \boldsymbol{E}_{inc}(\boldsymbol{\rho}) dl \tag{4.14}$$

and the impedance elements are defined as (see Fig. 4.2)

$$Z_{[n,p]}^{\mathbf{T},[m,q]} = jk\eta \int\limits_{L_m \cup N_m^{q+1}} \boldsymbol{t}_m^q(\boldsymbol{\rho}) \cdot \boldsymbol{A}_n^p(\boldsymbol{\rho}) dl + \int\limits_{L_m \cup N_m^{q+1}} \boldsymbol{t}_m^q(\boldsymbol{\rho}) \cdot \nabla \Phi_n^p(\boldsymbol{\rho}) dl \tag{4.15}$$

In view of the continuity along $L_m \cup N_m^1$ and $L_m \cup N_m^2$ of, respectively, $\boldsymbol{t}_m^2$ and $\boldsymbol{t}_m^1$, (4.15) can be simplified to

$$Z_{[n,p]}^{\mathbf{T},[m,q]} = jk\eta \int\limits_{L_m \cup N_m^{q+1}} \boldsymbol{t}_m^q(\boldsymbol{\rho}) \cdot \boldsymbol{A}_n^p(\boldsymbol{\rho}) dl - \int\limits_{L_m \cup N_m^{q+1}} \nabla \cdot \boldsymbol{t}_m^q(\boldsymbol{\rho}) \Phi_n^p(\boldsymbol{\rho}) dl \tag{4.16}$$

where the second line integral can now handle the $ln(|\boldsymbol{\rho} - \boldsymbol{\rho}_n^{p+1}|)$ singular contributions in $G_k(\boldsymbol{\rho}, \boldsymbol{\rho}_n^{p+1})$. Interestingly, the generation of the impedance elements in (4.16) demands less computational burden than in 4.11, for the surface tested approach. Similarly to (4.11), the integrals appearing in (4.16) are with weakly singular kernels.
The accuracy of our nonconforming implementations depends on the height of the testing elements (H), which we define, in view of Figs. 4.1 and 4.2, as a fraction of the discretization parameter (h).

4.3.3 Numerical results

We show TE-scattering results, RCS and near-field, for infinitely long single PEC objects with sharp-edged sections immersed in the free space. We pick the targets with small electrical dimensions since the singular field behaviour is observed near sharp edges and corners and, since the objects are electrically small, these singularities play an important role in the scattered fields. We show the improved accuracy versus the number of unknowns (N) and the height of the testing domains (H) of the corresponding discontinuous implementations, surface-tested, TE-EFIE[surf], and tangential-normal tested, TE-EFIE[tn], with respect to the conventional continuous implementation, TE-EFIE[C]. In the TE-scattering analysis of 2D PEC targets with smooth sections, where no singular fields are present [77], our nonconforming schemes show similar accuracy to the continuous piecewise linear scheme but doubling the number of unknowns.
In the TM-scattering study of infinitely long PEC targets, a Galerkin discontinuous piecewise linear implementation of the TM-EFIE is possible since the scalar potential is equal to zero. However, for the cases of sharp-edged PEC targets, no improvements in the near-field or far-field results were observed with respect to TM-EFIE[C], although the electric current exhibits singular nature around sharp corners, according to [77]. This leads us to the assumption that our nonconforming discontinuous implementations are especially suited for the singular charge modelling, electric and magnetic, the fact we will heavily exploit in the scattering analysis of plasmonic nanoparticles in resonance region.
We compute the inner line integrals in the generation of the impedance matrix through the singularity subtraction technique [85], [86] and 6-point quadrature rule. In the TE-EFIE[surf], we compute the surface testing integral over each quadrilateral through surface integrals over two triangles with 3-point rule [87]. In the TE-EFIE[C] and TE-EFIE[tn], the outer line integrals are computed with, respectively, 2 and 4 point rules, for the potentials $\boldsymbol{A}$ or Φ. In all the 2D PEC testing objects, the scattered fields are computed under an impinging $+y$ propagating plane wave and the free space wavelength λ_0 is set to $0.06\pi m$.
We assess the relative performance of the TE-EFIE implementations by displaying the root-mean-square relative error of the near-field and RCS results. All the testing domains are defined conformal to the boundary.
We define the near-field relative error e_{near} for a particular implementation, as

$$e_{near} = \frac{\Big[\sum\limits_{j=1}^{M} |\tilde{\boldsymbol{E}}(\boldsymbol{\rho}_j) - \boldsymbol{E}_{REF}(\boldsymbol{\rho}_j)|^2 + \eta_0^2 \sum\limits_{j=1}^{M} |\tilde{\boldsymbol{H}}(\boldsymbol{\rho}_j) - \boldsymbol{H}_{REF}(\boldsymbol{\rho}_j)|^2\Big]^{1/2}}{\Big[\sum\limits_{j=1}^{M} |\boldsymbol{E}_{REF}(\boldsymbol{\rho}_j)|^2 + \eta_0^2 \sum\limits_{j=1}^{M} |\boldsymbol{H}_{REF}(\boldsymbol{\rho}_j)|^2\Big]^{1/2}} \tag{4.17}$$

by computing the approximated electric and magnetic fields, respectively, $\tilde{\boldsymbol{E}}$ and $\tilde{\boldsymbol{H}}$, over a set of M points, $\{\boldsymbol{\rho}_1 ... \boldsymbol{\rho}_M\}$. The observation points are distributed uniformly around the object's section at a very close distance (the mesh parameter adopted in the discontinuous implementations).
Similarly, we define the far-field error e_{far} in terms of the bistatic RCS computed with a particular implementation over a set of M observation angles $\{\theta_1 ... \theta_M\}$, uniformly distributed, so that

$$e_{far} = \frac{\Big[\sum\limits_{j=1}^{M} |RCS(\theta_j) - RCS_{REF}(\theta_j)|^2\Big]^{1/2}}{\Big[\sum\limits_{j=1}^{M} |RCS_{REF}(\theta_j)|^2\Big]^{1/2}} \tag{4.18}$$

where $\theta_1 = 0$ and $\theta_M = 2\pi - 2\pi/M$. The near-field and far-field errors provide relative measures with respect to reference near-field and RCS solutions, respectively, $\boldsymbol{E}_{REF}$, $\boldsymbol{H}_{REF}$ and RCS_{REF}. With no analytical solutions available for the sharp-edged objects tested, the reference solutions in (4.17) and (4.18) are computed with the conventional continuous piecewise linear implementation, TE-EFIE[C], and very fine degree of meshing of the boundary line (around 15000 segments for the tested objects). The segmentations of the boundary line of the tested objects when computing the reference results employ geometrical mesh refinement near the sharp edges so that the ratio of the smallest segment to the biggest segment is set to 0.05. The source integrals in the computed far and near fields in (4.17) and (4.18) are carried out with 2 point and 10 point numerical rules, respectively. In all the examples, we adopt $M = 1000$.

4.3.3.1 Accuracy versus H

In Figs. 4.3 and 4.4, we plot the error performance of our nonconforming TE-EFIE implementations for two infinitely long sharp-edged PEC objects with equilateral triangular and square sections and sides of $0.2\lambda_0$. We plot our errors in terms of the height of the testing domains H defined as a fraction of the mesh parameter h. We display the normalized error $\bar{e}$ for each nonconforming implementation which we define as

$$\bar{e}^{tn}_{near} = \frac{e^{tn}_{near}}{e^{C}_{near}}, \quad \bar{e}^{surf}_{near} = \frac{e^{surf}_{near}}{e^{C}_{near}} \tag{4.19}$$

$$\bar{e}^{tn}_{far} = \frac{e^{tn}_{far}}{e^{C}_{far}}, \quad \bar{e}^{surf}_{far} = \frac{e^{surf}_{far}}{e^{C}_{far}} \tag{4.20}$$

where e^{tn}_{near}, e^{surf}_{near}, and e^{tn}_{far}, e^{surf}_{far} arise from computing, respectively, (4.17) and (4.18) with the corresponding nonconforming implementations of the TE-EFIE.
Similarly, e^{C}_{near} and e^{C}_{far} are derived from evaluation of (4.17) and (4.18), respectively, with the solution of the TE-EFIE[C]. In order to build a fair comparison, our nonconforming and piecewise continuous implementations handle the same number of unknowns. Hence, TE-EFIE[C] makes use of segments that are twice smaller than the segments adopted in our nonconforming implementations, where two unknowns are assigned to each boundary segment. Also, we establish uniform segmentations of the boundary line so that the mesh parameters are the same in all cases ($h \simeq 0.0033\lambda_0$ for continuous piecewise linear implementation).
In view of Figs. 4.3 and 4.4, our nonconforming discontinuous TE-EFIE implementations outperform the continuous scheme for a wide range of H values in both far-field and near-field scenarios. In view of the definition of the normalized errors in (4.19) and (4.20), there is an improvement in our nonconforming implementations as long as the normalized error is smaller than one. From the comparison of far-field errors in Fig. 4.3 with the near-field errors in Fig. 4.4 the H-ranges of improved far-fields appear similar or slightly wider than

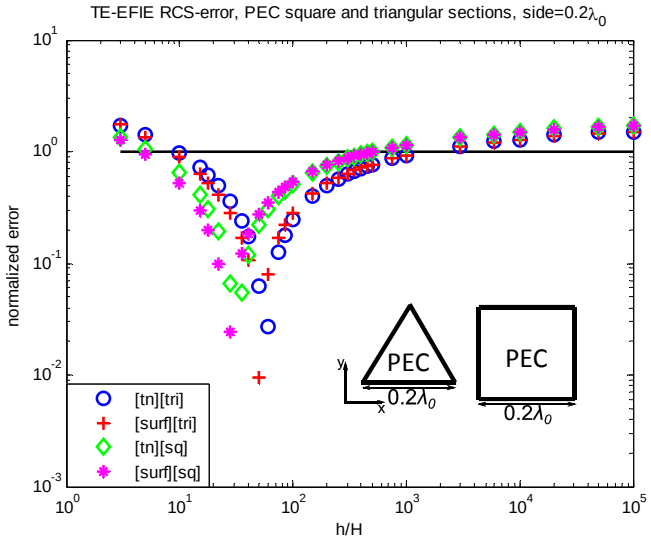

Figure 4.3: Normalized RCS error (4.20) computed for several nonconforming TE-EFIE implementations, relative to TE-EFIE[C], and the same number of unknowns (180 for triangular and 240 for square section) versus the height H of the testing domains for PEC cylinders with equilateral triangular or square sections and side $0.2\lambda_0$ ($\lambda_0 = 0.06\pi m$). The reference results are computed with TE-EFIE[C] and very fine meshing (12000 segments for triangular and 16000 segments for square section).

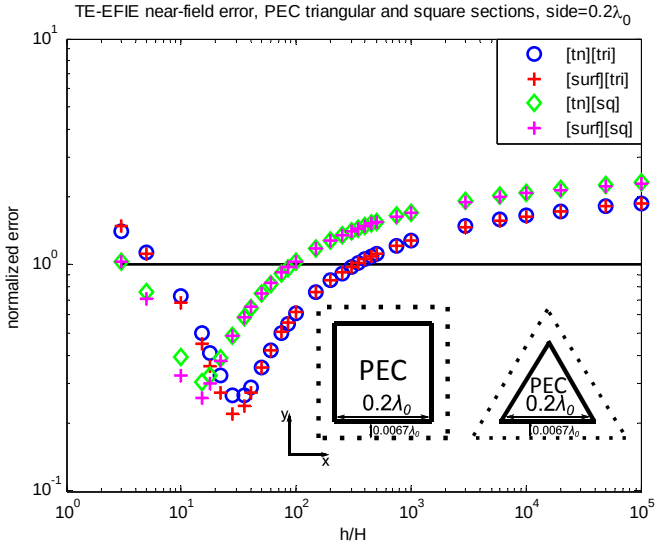

Figure 4.4: Normalized near-field error (4.19) computed for several nonconforming TE-EFIE implementations, relative to TE-EFIE[C], and the same number of unknowns (180 for triangular and 240 for square section) versus the height H of the testing domains for PEC cylinders with equilateral triangular or square sections and side $0.2\lambda_0$ ($\lambda_0 = 0.06\pi m$). The reference results are computed with TE-EFIE[C] and very fine meshing (12000 segments for triangular and 16000 segments for square section).

the near-field H-ranges. In general, we observe the accuracy improvements between $h/10$ and $h/500$ for our nonconforming TE-EFIE implementations in both near-fields and far-fields. Furthermore, we see that the impact on the overall accuracy of our nonconforming implementations due to the surface testing and the tangential-normal testing is quite similar.

4.3.3.2 Accuracy versus N

We show the relative far-field and near-field errors for our nonconforming and conforming TE-EFIE implementations as defined in (4.18) and (4.17), respectively.
The errors are plotted in terms of the number of unknowns N for electrically small infinitely long PEC cylinders with square or equilateral triangle sections and side of $0.2\lambda_0$. Our discontinuous implementations employ H values that are inside the good performing H-ranges displayed on Figs. 4.3 and 4.4 . As regards the far-field behaviour, in light of Fig. 4.5, TE-EFIE[C] exhibits around $\mathcal{O}(h^{1.3})$ decrease in the far-field error as the mesh parameter h is reduced. As shown in Fig. 4.5, our nonconforming implementations of TE-EFIE exhibit the reduction in far-field errors, for the examples presented, around $\mathcal{O}(h^{1.3})$, and the errors are always smaller than the ones produced by continuous implementation. As for the near-field performance, in light of Fig. 4.6, the continuous implementation exhibits around $\mathcal{O}(h^{1.5})$ decrease in the near-field error

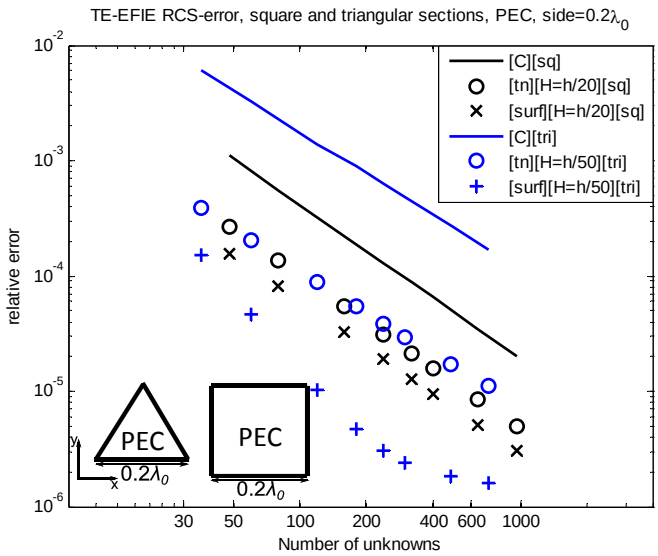

Figure 4.5: Relative RCS-error (4.18) computed for several nonconforming TE-EFIE implementations, versus the number of unknowns N for PEC cylinders with equilateral triangular or square sections and side $0.2\lambda_0$ ($\lambda_0 = 0.06\pi m$). The reference results are computed with TE-EFIE[C] and very fine meshing (12000 segments for triangular and 16000 segments for square section)

Our discontinuous implementations provide faster reduction and smaller near-field errors as h diminishes, when compared with continuous implementation. Our discontinuous implementations show a reduction in near-field error around $\mathcal{O}(h^2)$ (see Fig. 4.6).

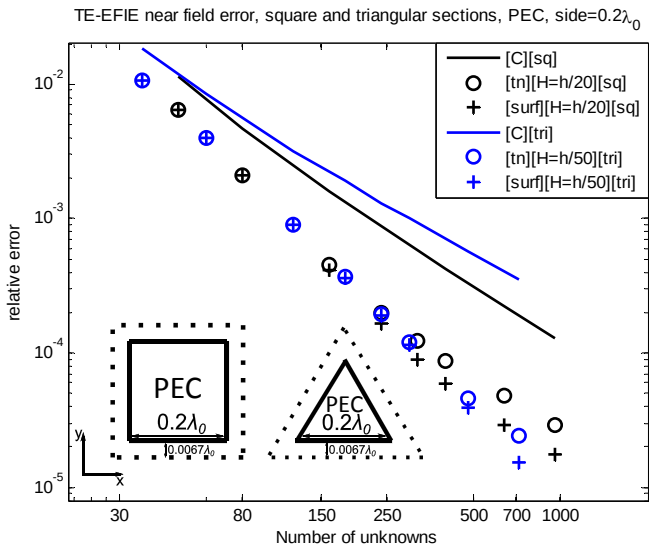

Figure 4.6: Relative near-field error (4.17) computed for several nonconforming TE-EFIE implementations, versus the number of unknowns N for PEC cylinders with equilateral triangular or square sections and side $0.2\lambda_0$ ($\lambda_0 = 0.06\pi m$). The reference results are computed with TE-EFIE[C] and very fine meshing (12000 segments for triangular and 16000 segments for square section)

4.3.3.3 Hybrid TE-EFIE

The hybrid nonconforming implementations of the TE-EFIE, in the analysis of sharp-edged infinitely long PEC cylinders with polygonal sections arise from the continuous expansion of the current at nodes inside the sides of the polygon and the discontinuous expansion at the corners [54]. This implementation is not segment-based and cannot hence benefit from the inherent flexibility associated with the fully discontinuous schemes.
However, as shown in Fig. 4.7 for the cylinders with the equilateral triangular or square sections and side $0.2\lambda_0$, the hybrid discontinuous implementations of the TE-EFIE exhibit huge improved accuracy with respect to the fully continuous schemes (and the same number of unknowns). Note that the hybrid and continuous implementations for the same boundary segmentation of sharp-edged target handle a very similar amount of unknowns. When compared with Fig. 4.3 and the fully discontinuous implementations, it is clear that the H-range of improved performance for the hybrid implementations rises drastically. This illustrates that the observed trends in Fig. 4.3 are mainly due to the discontinuous modelling of the current transition at the corners of the polygon, where the singular-field behaviour occurs.

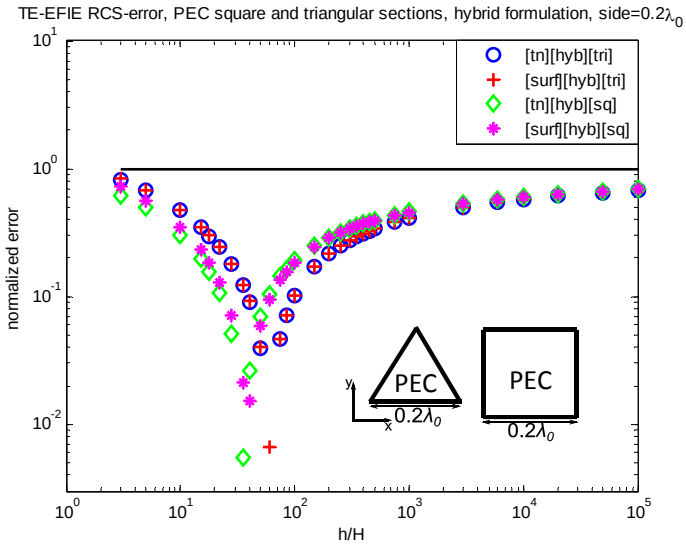

Figure 4.7: Normalized RCS error (4.20) computed for several hybrid TE-EFIE implementations, relative to TE-EFIE[C], and the same number of unknowns (180 for triangular and 240 for square section) versus the height H of the testing domains for PEC cylinders with equilateral triangular or square sections and side $0.2\lambda_0$ ($\lambda_0 = 0.06\pi m$). The reference results are computed with TE-EFIE[C] and very fine meshing (12000 segments for triangular and 16000 segments for square section)

4.4 Discontinuous MoM discretization of PMCHWT for single penetrable targets

In general, the scattering analysis of a homogeneous z-infinite penetrable body, with arbitrary section, illuminated by a TE-polarized plane wave is carried out, in light of the equivalence theorem, through the superposition of the scattered fields, $\boldsymbol{E}_i^s$ and $\boldsymbol{H}_i^s$, associated with the homogeneous problems of, respectively, regions $(i = 1)$ and $(i = 2)$ (see Fig. 4.8). These fields are generated by the equivalent currents over the penetrable interface, $\boldsymbol{J}_i$ and $\boldsymbol{M}_i$, so that the total fields arising from the summation of the incident and scattered fields, $\boldsymbol{E}_i$ and $\boldsymbol{H}_i$, are zero outside of the respective regions (see Fig. 4.8). We assume that the incident electric and magnetic fields in the original problem are in region 1, whereby the total fields, electric or magnetic, generated in the homogeneous problems associated with region i, $\boldsymbol{C}_i$, become

$$\boldsymbol{C}_1(\boldsymbol{\rho}) = \begin{cases} \boldsymbol{C}_1^S(\boldsymbol{\rho}) + \boldsymbol{C}_{inc}(\boldsymbol{\rho}), & \boldsymbol{\rho} \in region\ 1 \\ 0, & \boldsymbol{\rho} \in region\ 2 \end{cases} \tag{4.21}$$

$$\boldsymbol{C}_2(\boldsymbol{\rho}) = \begin{cases} 0, & \boldsymbol{\rho} \in region\ 1 \\ \boldsymbol{C}_2^S(\boldsymbol{\rho}), & \boldsymbol{\rho} \in region\ 2 \end{cases} \tag{4.22}$$

The electric and magnetic currents, $\boldsymbol{J}_i$ and $\boldsymbol{M}_i$, are expanded with tangentially orientated $\{\boldsymbol{f}_1^1 ... \boldsymbol{f}_{N_s}^1, \boldsymbol{f}_1^2 ... \boldsymbol{f}_{N_s}^2\}$ (4.2), and z-oriented $\{\boldsymbol{g}_1^1 ... \boldsymbol{g}_{N_s}^1, \boldsymbol{g}_1^2 ... \boldsymbol{g}_{N_s}^2\}$ discontinuous piecewise lin-

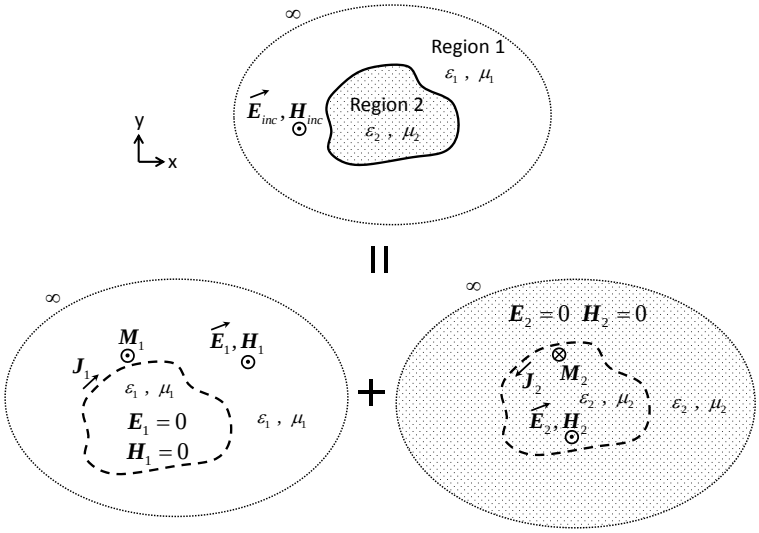

Figure 4.8: Application of the surface equivalence theorem to a z-infinite penetrable cylinder with the arbitrary section under an impinging TE-polarized plane wave

ear sets of basis functions, such that

$$\boldsymbol{M}_i \simeq \sum_{p=1}^{2}\sum_{n=1}^{N_s} M_n^{p,i}\boldsymbol{g}_n^p, \quad i=1,2 \tag{4.23}$$

$$\boldsymbol{J}_i \simeq \sum_{p=1}^{2}\sum_{n=1}^{N_s} J_n^{p,i}\boldsymbol{f}_n^p, \quad i=1,2 \tag{4.24}$$

where the sequences $\{J_n^1\}$, $\{J_n^2\}$ and $\{M_n^1\}$, $\{M_n^2\}$ denote the unknown coefficients in the expansion of the electric and magnetic currents over the ith-region's side of the boundary interface, respectively, and

$$\boldsymbol{g}_n^p(\boldsymbol{\rho}') = \frac{1}{h_n}[(\boldsymbol{\rho}' - \boldsymbol{\rho}_n^p)\cdot\hat{l}_n]\hat{z}, \quad \boldsymbol{\rho}' \in L_n \quad p=1,2 \tag{4.25}$$

The discretization of TE-PMCHWT relies on the approximated scattered electric and magnetic fields in the problems associated with region i, $\tilde{\boldsymbol{E}}_i^S$ and $\tilde{\boldsymbol{H}}_i^S$, which yield

$$\begin{aligned}\tilde{\boldsymbol{E}}_i^S = &-\sum_{p=1}^{2}\sum_{n=1}^{N_s} jk_i\eta_i \boldsymbol{A}_n^{p,i}(\boldsymbol{\rho})J_n^{p,i} - \sum_{p=1}^{2}\sum_{n=1}^{N_s}\nabla\Phi_n^{p,i}(\boldsymbol{\rho})J_n^{p,i} \\ &- \sum_{p=1}^{2}\sum_{n=1}^{N_s}\boldsymbol{R}_n^{p,i}(\boldsymbol{\rho})\times\hat{z}M_n^{p,i}, \quad i=1,2\end{aligned} \tag{4.26}$$

$$\tilde{\boldsymbol{H}}_i^S = \sum_{p=1}^{2}\sum_{n=1}^{N_s}\boldsymbol{R}_n^{p,i}(\boldsymbol{\rho})\times\hat{l}_n J_n^{p,i} - \sum_{p=1}^{2}\sum_{n=1}^{N_s} j\frac{k_i}{\eta_i}\boldsymbol{F}_n^{p,i}(\boldsymbol{\rho})M_n^{p,i}, \quad i=1,2 \tag{4.27}$$

The quantities η_i and k_i represent, respectively, the wave impedance and the wave number of the ith region and the potentials $\boldsymbol{F}_n^{p,i}$ and $\boldsymbol{R}_n^{p,i}$ are defined as

$$\boldsymbol{F}_n^{p,i}(\boldsymbol{\rho}) = \int_{L_n} G_{k_i}(\boldsymbol{\rho}, \boldsymbol{\rho}') \boldsymbol{g}_n^p(\boldsymbol{\rho}') dl' \tag{4.28}$$

$$\boldsymbol{R}_n^{p,i}(\boldsymbol{\rho}) = \int_{L_n} \frac{1}{h_n} [(\boldsymbol{\rho}' - \boldsymbol{\rho}_n^p) \cdot \hat{l}_n] \nabla G_{k_i}(\boldsymbol{\rho}, \boldsymbol{\rho}') dl', \quad p = 1, 2 \quad i = 1, 2 \tag{4.29}$$

where G_{k_i} denotes the Green's function corresponding to the homogeneous problem associated with the ith region. The final matrices are constructed so that the tangential boundary conditions are satisfied, $J_n^{p,1} = -J_n^{p,2}$ and $M_n^{p,1} = -M_n^{p,2}$.
The electric field in (4.26) exhibits hypersingular kernel contributions over the boundary line, associated with the terms $\nabla \Phi_n^{p,i}$. In contrast, the magnetic field in (4.27) does not show such contributions because of the inherent zero magnetic charge density in the TE-scattering problems. In consequence, whereas the scattered magnetic fields can be Galerkin tested over the boundary line, the testing of the scattered electric fields needs to be shifted off the boundary line, inside the region where, in light of the equivalence principle, the electric and magnetic fields must be null (see Fig. 4.8). The wave number and the impedance of the medium i occupying the region i are $k_i = k_0 \sqrt{\epsilon_{r,i} \mu_{r,i}}$ and $\eta_i = \eta_0 \sqrt{\mu_{r,i} / \epsilon_{r,i}}$, where k_0 and η_0 denote the free space wave number and impedance, respectively.
The Galerkin testing of the magnetic-field boundary equation at the boundary line results in

$$\int_{L_m} \boldsymbol{g}_m^q \cdot \boldsymbol{H}_{inc} dl = \int_{L_m} \boldsymbol{g}_m^q \cdot (\tilde{\boldsymbol{H}}_2^S - \tilde{\boldsymbol{H}}_1^S) dl, \quad q = 1, 2 \quad 1 \leqslant m \leqslant N_s \tag{4.30}$$

where the limiting values of the singular kernel contributions in (4.29), at both sides of the boundary line, are canceled out so that such integrals can be taken as Cauchy principal values.
Here, we present two nonconforming discontinuous MoM-discretizations of the TE-PMCHWT. In both cases, we apply the magnetic-field boundary equation in (4.30). As regards the electric-field boundary equation, we apply in one case the surface testing scheme, which we call TE-PMCHWT[surf], and in the other case the tangential-normal testing, TE-PMCHWT[tn]. In view of (4.9) and (4.10), the tested electric-field boundary equation in TE-PMCHWT[surf] yields

$$\begin{aligned} \iint_{S_m^2} \boldsymbol{P}_m^{\mathbf{2},q} \cdot \boldsymbol{E}_{inc} dS = \iint_{S_m^1} \boldsymbol{P}_m^{\mathbf{1},q} \cdot \tilde{\boldsymbol{E}}_2^S dS - \iint_{S_m^2} \boldsymbol{P}_m^{\mathbf{2},q} \cdot \tilde{\boldsymbol{E}}_1^S dS, \\ q = 1, 2 \quad 1 \leqslant m \leqslant N_s \end{aligned} \tag{4.31}$$

where the set of testing functions $\{\boldsymbol{P}_1^{\mathbf{1},1} ... \boldsymbol{P}_{N_s}^{\mathbf{1},1}, \boldsymbol{P}_1^{\mathbf{1},2} ... \boldsymbol{P}_{N_s}^{\mathbf{1},2}\}$ and $\{\boldsymbol{P}_1^{\mathbf{2},1} ... \boldsymbol{P}_{N_s}^{\mathbf{2},1}, \boldsymbol{P}_1^{\mathbf{2},2} ... \boldsymbol{P}_{N_s}^{\mathbf{2},2}\}$ adopt the definition in (4.7) over a set of quadrilaterals, respectively, $\{S_m^1\}$ and $\{S_m^2\}$, attached to the boundary segmentation, inside regions 1 and 2 (see Fig. 4.9). Similarly, in light of (4.14) and (4.15), the electric-field boundary equation in TE-PMCHWT[tn] becomes

$$\int\limits_{L_m \cup N_m^{2,q+1}} \boldsymbol{t}_m^{\mathbf{2},q} \cdot \boldsymbol{E}_{inc} dl = \int\limits_{L_m \cup N_m^{1,q+1}} \boldsymbol{t}_m^{\mathbf{1},q} \cdot \tilde{\boldsymbol{E}}_2^S dl - \int\limits_{L_m \cup N_m^{2,q+1}} \boldsymbol{t}_m^{\mathbf{2},q} \cdot \tilde{\boldsymbol{E}}_1^S dl, \qquad q = 1,2 \quad 1 \leqslant m \leqslant N_s \tag{4.32}$$

where the set of testing functions $\{\boldsymbol{t}_1^{\mathbf{1},1} ... \boldsymbol{t}_{N_s}^{\mathbf{1},1}, \boldsymbol{t}_1^{\mathbf{1},2} ... \boldsymbol{t}_{N_s}^{\mathbf{1},2}\}$ and $\{\boldsymbol{t}_1^{\mathbf{2},1} ... \boldsymbol{t}_{N_s}^{\mathbf{2},1}, \boldsymbol{t}_1^{\mathbf{2},2} ... \boldsymbol{t}_{N_s}^{\mathbf{2},2}\}$ adopt the definition in (4.12) in such a manner that the sets of segments $\{N_1^{\mathbf{1},1} ... N_{N_s}^{\mathbf{1},1}, N_1^{\mathbf{1},2} ... N_{N_s}^{\mathbf{1},2}\}$ and $\{N_1^{\mathbf{2},1} ... N_{N_s}^{\mathbf{2},1}, N_1^{\mathbf{2},2} ... N_{N_s}^{\mathbf{2},2}\}$ are oriented from the endpoints of the boundary segments $\{L_1 ... L_{N_s}\}$ into, respectively, regions 1 and 2 (see Fig. 4.9).

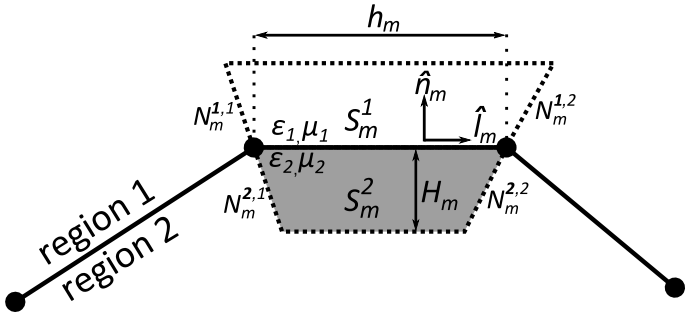

Figure 4.9: mth segment arising from the discretized section of an infinitely long penetrable cylinder where the testing schemes are defined conformal to the boundary

Note that in both testing schemes, (4.31) and (4.32), the incident and scattered fields are tested in the regions where, in accordance with the equivalence theorem, the total fields must be zero. The performance of such implementations depends on the heights of the testing domains (H), which we set in terms of the length of the associated segments (h) (see Figs. 4.1, 4.2 and 4.9). Here, we impose the same value of H for each of the testing domains, in regions 1 or 2, attached to a particular boundary segment.
Our discontinuous implementation of the TM-PMCHWT can be readily obtained from the expressions above. Indeed, in the TM case, the electromagnetic wave is impinging upon the z-infinite cylinder so that the magnetic field is oriented transversally and the electric field is z-oriented. In consequence, the sets of basis functions adopted for our discontinuous TM-expansions of the electric and magnetic currents arise from the sets of functions employed in the TE-expansions of, respectively, the magnetic and electric currents. Similarly, since in the TM case the electric charge is zero, the electric-field boundary equation is Galerkin tested, whereas the surface or the tangential-normal testing needs to be applied to the magnetic-field boundary equation, giving thus rise to the implementations TM-PMCHWT[surf] or TM-PMCHWT[tn].

4.4.1 Numerical results

In this section, we show TE/TM-scattering results, far-field (RCS) and near-field, for infinitely long homogeneous penetrable objects with sharp-edged sections embedded in the free-space. Equivalently to numerical tests performed in Section 4.3.3, we choose the targets with small electrical dimensions, and moderate or high relative permittivity

or permeability values since the singular field behaviour is observed at sharp edges and corners [77] and the proper modelling of these singularities plays a crucial role in obtaining reliable and highly accurate results.
In the TE-scattering problems of dielectric targets with moderate or high dielectric contrasts, we show the improved accuracy versus the number of unknowns (N) and the height of the testing domains (H) of the discontinuous TE-PMCHWT numerical implementations, TE-PMCHWT[surf] and TE-PMCHWT[tn], with respect to the conventional continuous implementation, TE-PMCHWT[C]. In the TE-scattering analysis of 2D targets with smooth sections and/or low relative permittivity contrasts, where no singular fields are present [77], our nonconforming schemes show similar accuracy to the continuous piecewise linear scheme, but doubling the number of unknowns.
Dually to our nonconforming TE-PMCHWT, the discontinuous nonconforming discretizations of TM-PMCHWT, TM-PMCHWT[surf] and TM-PMCHWT[tn], show accuracy improvements in the scattering analysis of small sharp-edged magnetic targets with moderate or high relative permeability values. To illustrate this, we show the TM-scattering results for electrically small 2D ferromagnetic targets. Similarly to TE-problems, no accuracy improvements were observed in the TM-analysis of smooth and/or low relative permeability objects since no singular fields are observed for those cases [77].
The TE/TM-PMCHWT implementations presented here are scaled in order to improve the condition numbers of the resulting impedance matrices. The magnetic-field equations are then multiplied by the free space impedance η_0 and the magnetic-current density is expressed in terms of another unknown so that $\boldsymbol{M}_i = \eta_0 \boldsymbol{M}'_i$ [47].
The inner line integrals in the generation of the impedance matrix are computed with the singularity subtraction technique [85], [86] and 6-point quadrature rule for all the interactions involved. In TE/TM-PMCHWT[surf], we compute the surface testing over each quadrilateral through surface integrals over two triangles with 3-point rule [87]. In TE/TM-PMCHWT[C] and TE/TM-PMCHWT[tn], the outer line integrals are computed with, respectively, 2 and 4 point rules, for the potentials $\boldsymbol{A}$, $\boldsymbol{F}$ or Φ and with, respectively, 4 and 8 point rules for potential $\boldsymbol{R}$. The scattered fields are computed under an impinging $+y$ propagating plane wave and the free space wavelength λ_0 is set to $0.06\pi m$.
We asses the accuracy of the TE/TM-PMCHWT implementations by computing the root-mean-square relative error of the near field and RCS results, according to expressions (4.17) and (4.18), respectively. We compute the relative errors in the same manner as for the infinitely long PEC targets. For the sake of enhanced accuracy, all the testing domains are defined conformal to the boundary.
The reference solutions in (4.17) and (4.18) are computed with the conventional implementations, TE/TM-PMCHWT[C], and very fine degree of meshing of the boundary line (around 15000 segments for the tested objects). The reference results are computed on a h-refined mesh equivalently to PEC case (see Section 4.3.3). The source integrals in the computed far and near fields in (4.17) and (4.18) are carried out with 2 point and 10 point numerical rules, respectively.

4.4.1.1 Accuracy versus H

In view of Figs. 4.10 and 4.11, we show the error plots of our discontinuous TE-PMCHWT schemes for an electrically small sharp-edged dielectric object with equilateral triangular section and side of $0.2\lambda_0$ and several dielectric contrasts (relative permittivities of 5, 15,

50, 90). Next, on Figs. 4.12 and 4.13, we show the error results of our discontinuous TM-PMCHWT numerical implementations for two small sharp-edged infinitely long ferromagnetic targets. We plot our errors in terms of the height of the testing domains H defined as a fraction of the mesh parameter h. We display the normalized near-field and far-field errors, for each discontinuous implementation, which are defined with expressions (4.19) and (4.20), respectively.
e^{tn}_{near}, e^{surf}_{near}, and e^{tn}_{far}, e^{surf}_{far} arise from computing, respectively, (4.17) and (4.18) with the corresponding discontinuous numerical implementations of TE/TM-PMCHWT. Similarly, e^{C}_{near} and e^{C}_{far} are computed with TE/TM-PMCHWT[C]. In order for the comparison to be fair, our discontinuous and piecewise continuous implementations handle the same number of unknowns. Hence, TE/TM-PMCHWT[C] makes use of a twice the number of segments employed by our discontinuous implementations. We establish uniform segmentations of the boundary line so that the mesh parameters are the same in all cases ($h \simeq 0.0033\lambda_0$ for continuous piecewise linear implementations).
As predicted by the theory [77], the well-performing H ranges grow as the relative permittivity/permeability rises and/or the target becomes sharper. Similarly to the observed results for PEC targets, the H-ranges of improved far-field appear similar or slightly wider than the near-field H-ranges. In general, we observe the accuracy improvements between $h/10$ and $h/600$ for our nonconforming discontinuous TE/TM-PMCHWT discretizations and high relative contrasts in both near-fields and far-fields. Furthermore, the surface and tangential-normal implementations show a quite similar accuracy.

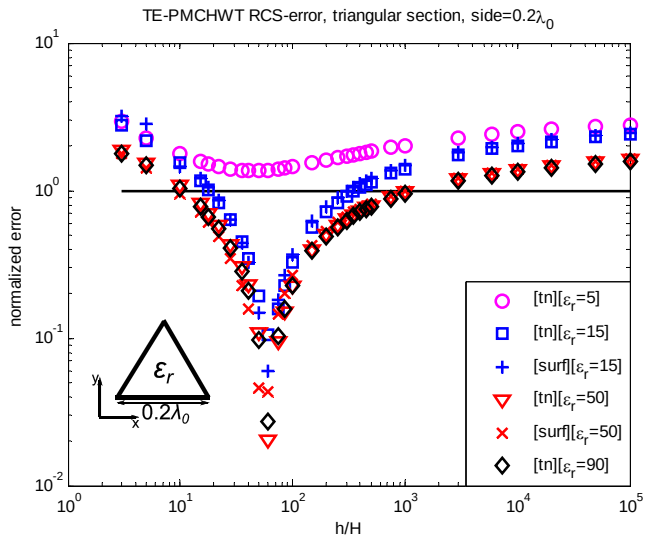

Figure 4.10: Normalized RCS error (4.20) computed for several nonconforming TE-PMCHWT implementations, relative to TE-PMCHWT[C], and the same number of unknowns (360) versus the height H of the testing domains for dielectric cylinders with equilateral triangular section, side $0.2\lambda_0$ ($\lambda_0 = 0.06\pi m$) and several relative permittivities (5, 15, 50, 90). The reference results are computed with TE-PMCHWT[C] and very fine meshing (12000 segments)

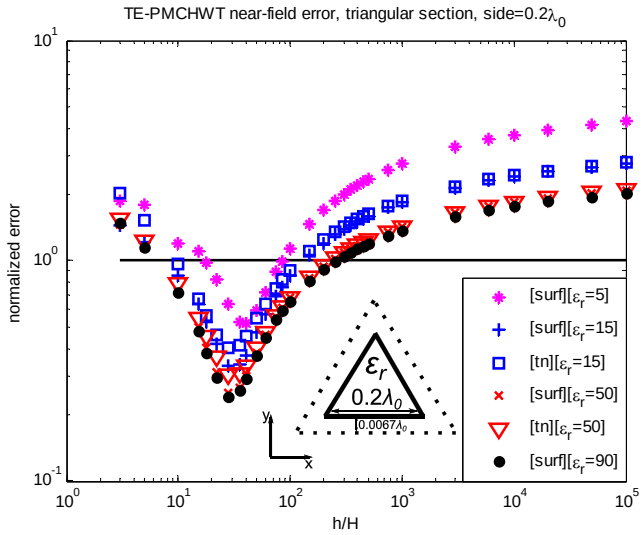

Figure 4.11: Normalized near-field error (4.19) computed for several nonconforming TE-PMCHWT implementations, relative to TE-PMCHWT[C], and the same number of unknowns (360) versus the height H of the testing domains for dielectric cylinders with equilateral triangular section, side $0.2\lambda_0$ ($\lambda_0 = 0.06\pi m$) and several relative permittivities (5, 15, 50, 90). The reference results are computed with TE-PMCHWT[C] and very fine meshing (12000 segments)

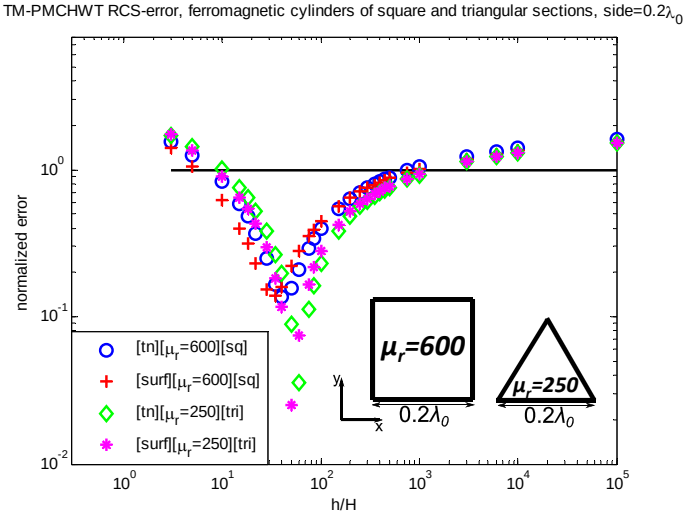

Figure 4.12: Normalized RCS error (4.20) computed for several discontinuous TM-PMCHWT implementations, relative to TM-PMCHWT[C], and the same number of unknowns (360) versus the height H of the testing domains for ferromagnetic cylinders with equilateral triangular or square section, side $0.2\lambda_0$ ($\lambda_0 = 0.06\pi m$) and two relative permeabilities (250, 600). The reference results are computed with TM-PMCHWT[C] and very fine meshing (12000 segments for triangular and 16000 segments for square section)

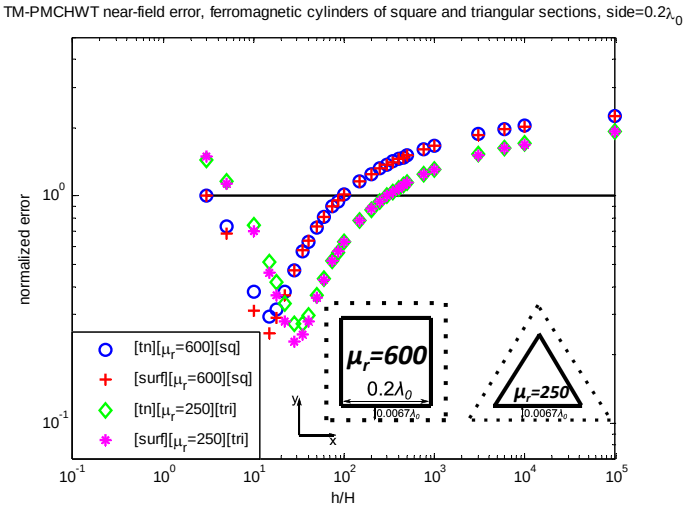

Figure 4.13: Normalized near-field error (4.19) computed for several discontinuous TM-PMCHWT numerical schemes, relative to TM-PMCHWT[C], and the same number of unknowns (360) versus the height H of the testing domains for ferromagnetic cylinders with equilateral triangular or square section, side $0.2\lambda_0$ ($\lambda_0 = 0.06\pi m$) and two relative permeabilities (250, 600). The reference results are computed with TM-PMCHWT[C] and very fine meshing (12000 segments for triangular and 16000 segments for square section)

4.4.1.2 Accuracy versus N

We present the relative far-field and near-field errors for our discontinuous and continuous TE-PMCHWT discretizations as defined in (4.18) and (4.17), respectively. The errors are plotted in terms of the number of unknowns N for electrically small infinitely long cylinders with square or equilateral triangle sections and side of $0.2\lambda_0$.
Our nonconforming implementations employ H values that are inside the good performing H-ranges shown on Figs. 4.10 and 4.11. As regards the far-field behaviour, in view of Fig. 4.14, TE-PMCHWT[C] exhibits around $\mathcal{O}(h^{1.3})$ decrease in the far-field error as the mesh parameter h is reduced. As shown in Fig. 4.14, our discontinuous numerical implementations of the TE-PMCHWT exhibit the reduction in far-field errors around $\mathcal{O}(h^{1.8})$, with the smaller observed errors than the errors produced by a continuous implementation. As for the near-field performance, in view of Fig. 4.15, the continuous implementation exhibits around $\mathcal{O}(h^{1.5})$ decrease in the near-field error. Our nonconforming implementations provide a faster reduction in the near-field error as h diminishes, when compared with continuous implementations. Indeed, according to Fig. 4.15, our discontinuous implementations show a reduction in the near-field error around $\mathcal{O}(h^2)$. Our discontinuous implementations of TM-PMCHWT exhibit the same performance as the TE-PMCHWT counterparts if the values of relative permittivity and permeability are swapped (they are dual to each other).

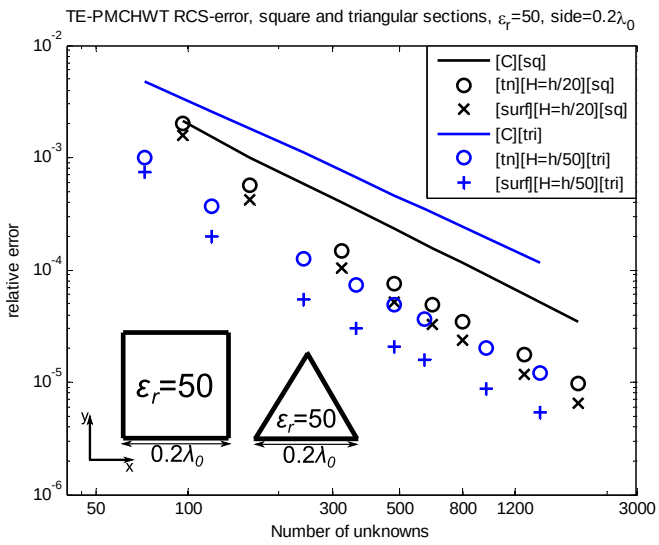

Figure 4.14: Relative RCS error (4.18) computed for several TE-PMCHWT implementations discretized with discontinuous basis functions, versus the number of unknowns N, for dielectric cylinders with equilateral triangular or square sections, relative permittivity 50, and side $0.2\lambda_0$ ($\lambda_0 = 0.06\pi m$). The reference results are computed with TE-PMCHWT[C] and very fine meshing (12000 segments for triangular and 16000 segments for square section)

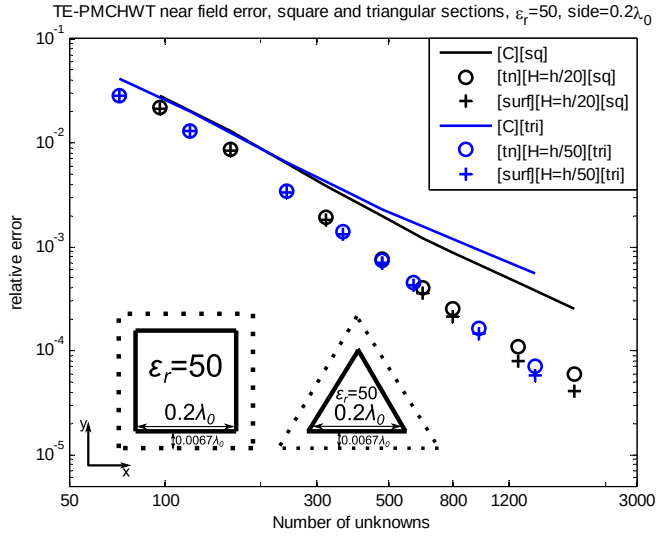

Figure 4.15: Relative near-field error (4.17) computed for several discontinuous TE-PMCHWT discretizations, versus the number of unknowns N, for dielectric cylinders with equilateral triangular or square sections, relative permittivity 50, and side $0.2\lambda_0$ ($\lambda_0 = 0.06\pi m$). The reference results are computed with TE-PMCHWT[C] and very fine meshing (12000 segments for triangular and 16000 segments for square section)

4.4.1.3 Hybrid TE-PMCHWT

The hybrid nonconforming implementations of TE/TM-PMCHWT, in the analysis of sharp-edged infinitely long homogeneous penetrable cylinders with polygonal sections, similarly to hybrid continuous-discontinuous TE-EFIE discretizations, arise from the continuous expansion of the currents at nodes inside the sides of the polygon and the discontinuous expansion at the corners. The hybrid discontinuous implementations of TE-PMCHWT exhibit improved accuracy with respect to the continuous scheme in all H-range (see Fig. 4.16). This proves that the observed trends in Fig. 4.10 are mainly due to the discontinuous modelling of the current transition at the corners of the polygon, where the singular-field behaviour is induced. The hybrid TE/TM-PMCHWT implementations make a suitable choice for the accurate analysis of single homogeneous penetrable targets with sharp edges where the singular fields are involved.

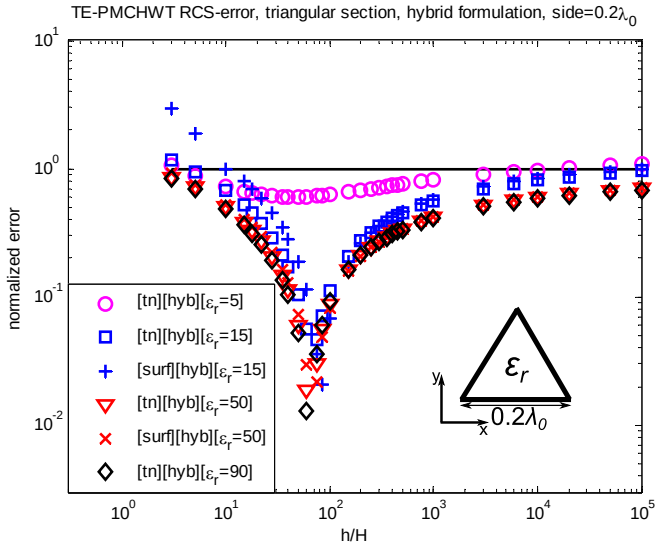

Figure 4.16: Normalized RCS error (4.20) computed for several hybrid continuous-discontinuous TE-PMCHWT discretizations, relative to TE-PMCHWT[C], and the same number of unknowns (360) versus the height H of the testing domains for dielectric cylinders with equilateral triangular section, side $0.2\lambda_0$ ($\lambda_0 = 0.06\pi m$) and several relative permittivities (5, 15, 50, 90). The reference results are computed with TE-PMCHWT[C] and very fine meshing (12000 segments)

4.5 Discretization of EFIE-PMCHWT with discontinuous basis functions for 2D composite PEC and penetrable structures with junctions

Our discontinuous nonconforming implementations for the TE-scattering analysis of composite infinitely long objects, with PEC or penetrable regions, TE-EFIE-PMCHWT, arise from the following:

1. The definition of the expansions in (4.24) for the electric currents and the imposition of the electric-field boundary conditions (4.31) or (4.32) over all the boundary interfaces

2. The definition of the expansion (4.23) for the magnetic currents and the imposition of the Galerkin-tested magnetic-field boundary equation (4.30), exclusively, over interfaces shared by penetrable regions (see Fig. 4.17).

Similarly, in the TM-scattering problems, our nonconforming TM-EFIE-PMCHWT is defined from the following statements

1. Electric current is expanded with $\hat{z}$ oriented discontinuous piecewise linear basis functions and the electric-field boundary equation is Galerkin tested over all the boundary-interfaces

2. Magnetic current is expanded with tangentially oriented discontinuous piecewise linear basis functions and the magnetic-field boundary equation is tested with the surface or tangential-normal schemes over interfaces shared by penetrable regions

In general, the single-trace continuous piecewise linear implementation of the EFIE-PMCHWT formulation is defined in an analogous manner as the discontinuous implementation for basis and testing functions out of junctions, except for the fact that the electric and magnetic field conditions are Galerkin tested. This scheme treats the interface between two different regions as *single lines*, however, the single-line continuous piecewise linear implementations become somewhat laborious at junction nodes from the implementation point of view because specially tailored schemes need to be defined in order to enforce the continuity conditions [46]- [50].
In Fig. 4.17, we show a composite structure with one penetrable junction [A], where all the intersecting regions are penetrable, and three PEC-penetrable junctions [B], [C], and [D], where one of the intersecting regions is PEC.
In both types of junctions, tangential electric field and current continuity conditions around junctions need to be enforced; moreover, for the penetrable junction, the magnetic continuity of the current and field conditions are also required. Note that, unlike the single penetrable object, where each unknown (electric or magnetic) is invoked by the two homogeneous penetrable problems, the unknowns associated with the penetrable junction node in Fig. 4.17 are invoked by the three associated homogeneous problems, one for each intersecting region at the junction. Similarly, the (electric) unknowns at each PEC-penetrable junction node [B], [C] or [D] are invoked by different pairs of associated homogeneous problems, respectively, regions 2, 3, 1, 2, or 1, 3. Clearly, the node-based continuous single-line EFIE-PMCHWT implementation involves a significant

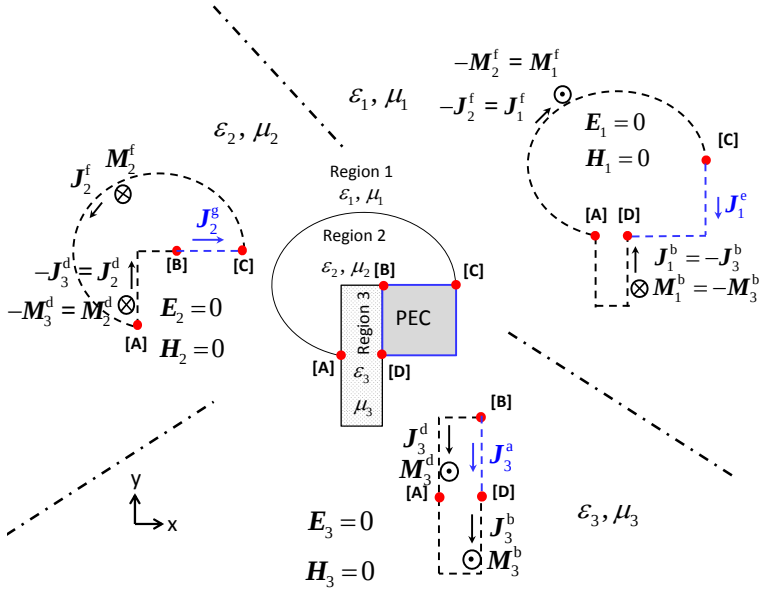

Figure 4.17: Surface equivalence theorem applied to an infinitely long composite object with two penetrable regions and one PEC region. The dashed lines denote line interfaces between regions. The nodes denote junctions. TE-polarized plane wave is illuminating the structure

burden when handling junctions if compared with our segment-based discretization, which by definition ignores junctions.

Interestingly, another conforming implementation of the EFIE-PMCHWT can be obtained by analyzing the composite structure as a set of disjoint objects, corresponding to each of the regions of the composite object, immersed in the free space and with separation distances tending to zero ($\delta \to 0$) (see Fig. 4.18) [51]. This scheme considers the interfaces as *two contact lines* and becomes easier to implement than the single-line approach since no continuity exceptions need to be considered at junction nodes. However, the amount of unknowns is increased because redundant currents are defined over the two contact surfaces. Also, in addition to the Cauchy principal value of the integrals, the residue term needs to be computed and for some particular examples the multi-body modelling may become complicated.

4.5.1 Numerical results

We show RCS results for infinitely long composite objects inside the free-space, with piecewise homogeneous regions, PEC or dielectric. We show how our discontinuous implementations of TE/TM-EFIE-PMCHWT for composite bodies, where the nodes are ignored in both the current expansion and the field testing, allow agile management of junction-nodes while providing similar or improved accuracy.

Furthermore, these implementations allow for easy management of composite objects arising from the juxtaposition of penetrable targets meshed with independent segmentations, which are typically nonconformal (i.e., with nonmatching nodes, see Fig. 4.18(c)).

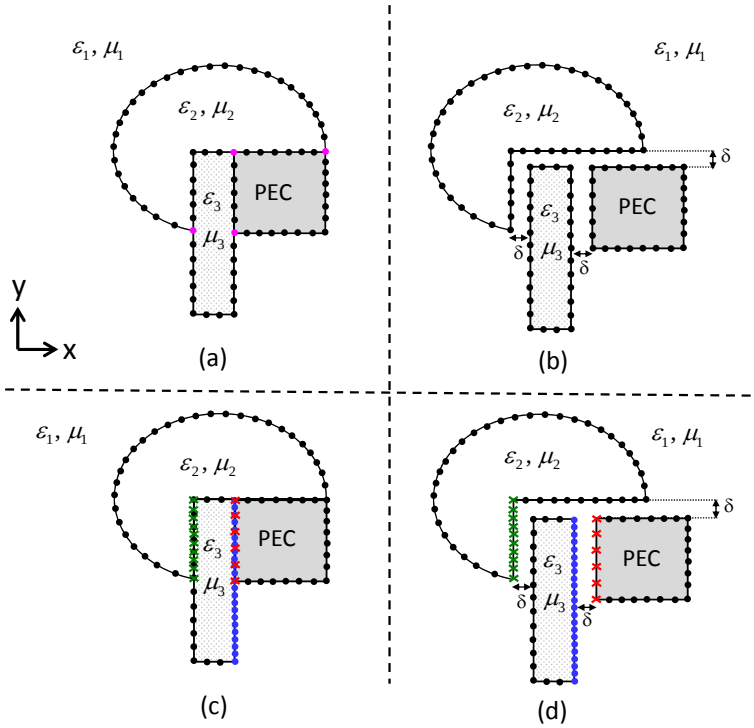

Figure 4.18: Analysis of 2D composite objects. (a) Single-line interfaces and conformal segmentations. (b) Interfaces with two contact lines and conformal segmentations when $\delta \to 0$. (c) Single-line interfaces and nonconformal segmentations. (d) Interfaces with two contact lines and nonconformal segmentations when $\delta \to 0$

Although in theory the two-contact-line approach can handle such problems (see Fig. 4.18(d)), in practice the required computation of the residue terms becomes bothersome when the field and source segmentations do not match. For such composite multi-penetrable structures, our discontinuous TE/TM-PMCHWT numerical implementations allow the definition of the electric current and the electric-field boundary condition at one nonmatching mesh and the magnetic current and the magnetic-field boundary condition over the other nonmatching mesh. This is still a single-line approach because the field equations and the currents are defined at one boundary line, but is meshed through two different, overlapped, segmentations.

For the sake of the robust and flexible analysis of complex structures, we adopt testing domains nonconformal to the boundary line, whereby no *a priori* knowledge on nodes is required. In Figs. 4.19 and 4.20 we compare the RCS-performance of our discontinuous TE-EFIE and TE-PMCHWT numerical implementations with testing domains defined conformal[conf] or nonconformal[nonconf] to the boundary line. Some loss of accuracy is observed for the nonconformal choice, which we attribute to the fact that the testing elements bordering on abruptly sharp corners cross the boundary line. We minimize such discrepancy in our discontinuous EFIE-PMCHWT numerical implementations with a testing nonconformal to the boundary by adopting very small H-values ($H = h/1e5$).

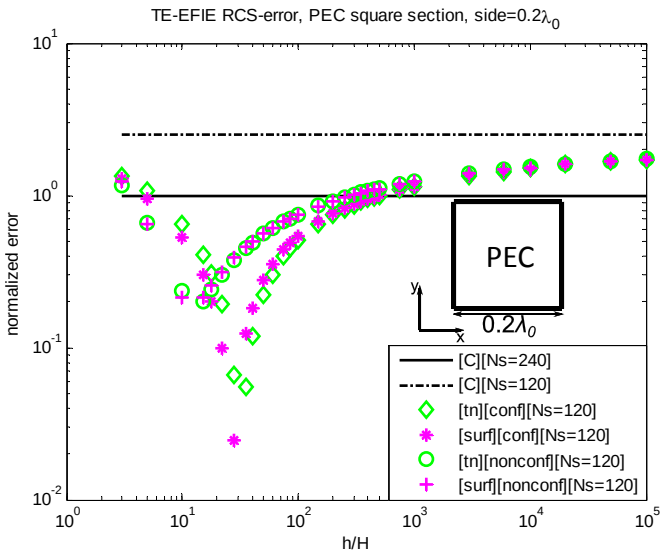

Figure 4.19: Normalized RCS error (4.20) computed for several discontinuous TE-EFIE discretizations, relative to TE-EFIE[C][$N_s = 240$], versus the height H of the testing domains (conformal or nonconformal to the boundary) for a PEC cylinder with square section and side $0.2\lambda_0$ ($\lambda_0 = 0.06\pi m$). The reference results are computed with TE-EFIE[C] and very fine meshing (16000 segments). N_s denotes the number of segments

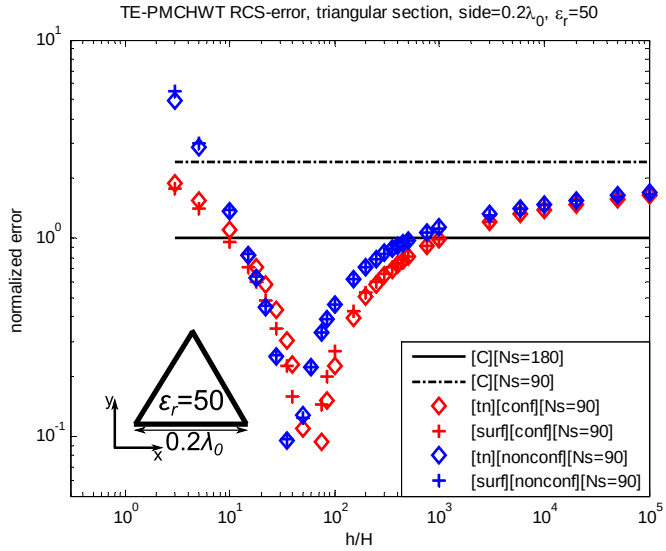

Figure 4.20: Normalized RCS error (4.20) computed for several discontinuous TE-PMCHWT implementations, relative to TE-PMCHWT[C] [$N_s = 180$], versus the height H of the testing domains (conformal or nonconformal to the boundary) for a dielectric cylinder with equilateral triangular section, side $0.2\lambda_0$ ($\lambda_0 = 0.06\pi m$) and $\epsilon_r = 50$. The reference results are computed with TE-PMCHWT[C] and very fine meshing (12000 segments). N_s denotes the number of segments

When compared with the continuous implementations, our nonconforming implementations produce similar or better far-field results, if the same number of unknowns or the same mesh, respectively, are adopted (see Figs. 4.19 and 4.20). In Figs. 4.21 and 4.22, we show RCS results for composite objects with PEC and dielectric regions and our discontinuous implementations of the TE-EFIE-PCMHWT (Figs. 4.21a and 4.22) or of TM-EFIE-PMCHWT implementation (see Fig. 4.21b). Whereas our TE/TM-EFIE-PMCHWT implementations in Figs. 4.21 and 4.22 adopt the single-line approach, the reference results are obtained with the continuous piecewise linear implementation and the two-contact-line approach. In Fig. 4.23, we provide TE-RCS results for a composite body with two dielectric regions arising from the juxtaposition of two independent meshes resulting in a nonconformal mesh (i.e., with nonmatching nodes). In view of Fig. 4.23, the single-line discontinuous TE-PMCHWT numerical implementations provide similar accuracy as the continuous piecewise linear implementation with two contact lines. In order to reach a fair comparison, we generate the impedance matrices of our discontinuous and the piecewise linear implementations with similar sizes. In any case, the number of unknowns handled by the continuous implementations, with two contact lines, is somewhat bigger because additional unknowns are introduced where boundary lines are in contact. For all the 2D composite targets, the scattered fields are computed under an impinging $+y$ propagating plane wave and the free space wavelength λ_0 is set to $0.06\pi m$.

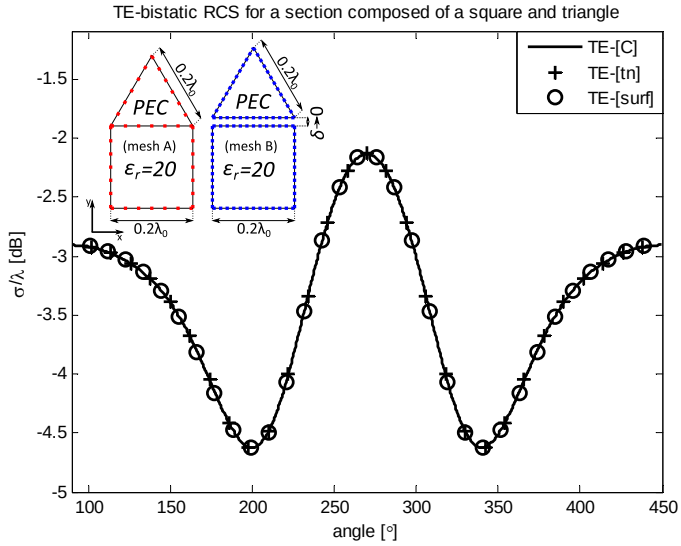

(a)

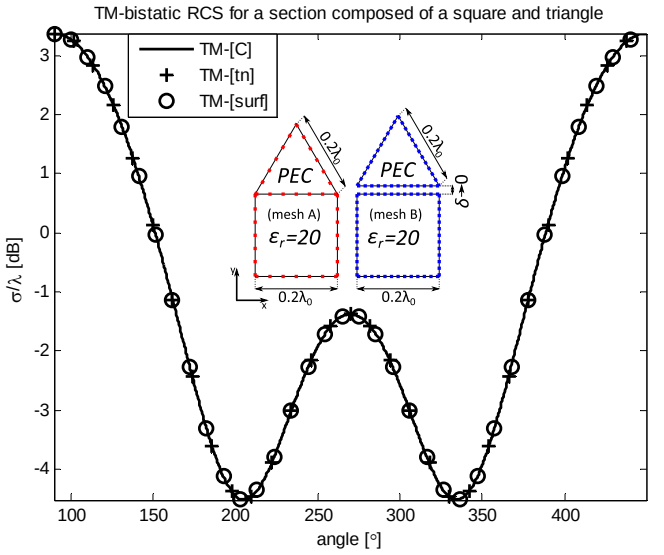

(b)

Figure 4.21: Bistatic RCS of a composite object consisting of dielectric cylinder of square section and a PEC cylinder of equilateral triangle section under an impinging (a) TE-polarized and (b) TM-polarized $+y$ propagating plane wave. The relative permittivity of the region with square section is 20. The number of unknowns is 360 for our discontinuous EFIE-PMCHWT numerical implementations and 440 for the continuous implementation, which is adopted as reference

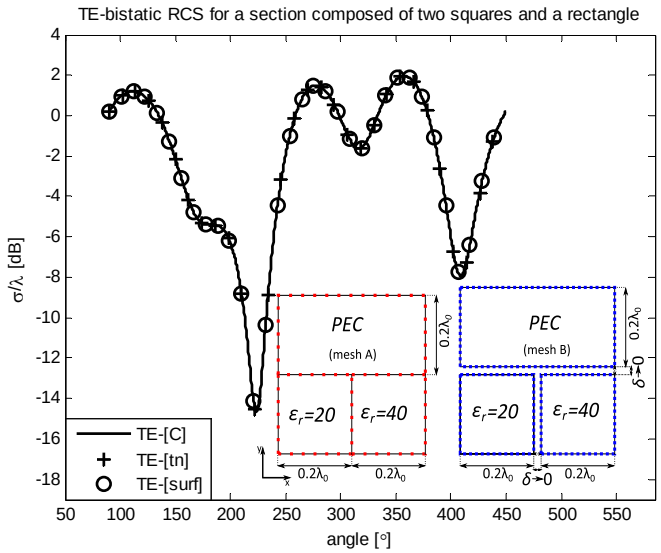

Figure 4.22: Bistatic RCS of a composite object consisting of two dielectric cylinders of square section and a PEC cylinder of rectangular section under an impinging TE-polarized $+y$ propagating plane wave. The relative permittivities of the two dielectric cylinders are 20 and 40. The number of unknowns is 640 for our discontinuous EFIE-PMCHWT discretizations and 800 for the continuous implementation, which is adopted as reference

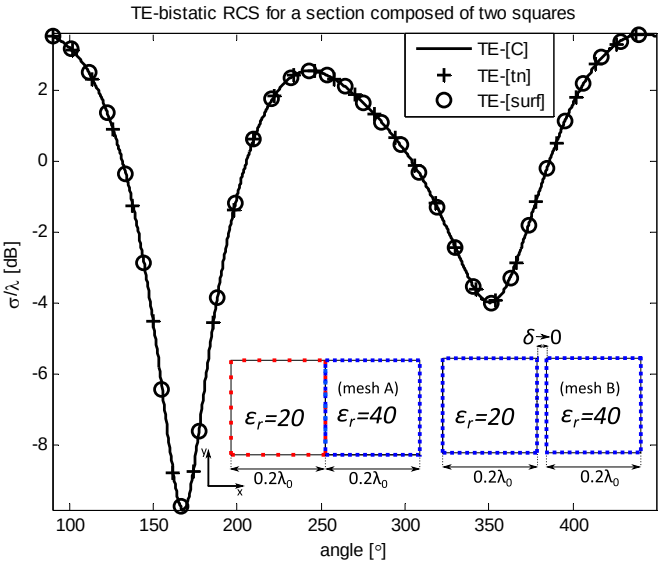

Figure 4.23: Bistatic RCS of a composite object consisting of two dielectric cylinders of square section assembled after juxtaposing two independent closed line meshes under an impinging TE-polarized $+y$ propagating plane wave. The relative permittivity of the two dielectric cylinders is 20 and 40. The number of unknowns is 700 for our discontinuous PMCHWT implementations and 960 for the continuous implementation, which is adopted as reference

4.6 Conclusion

The discretization with discontinuous piecewise linear basis functions of the currents and the testing of the fields off the boundary interfaces, with surface or tangential-normal testing, gives rise to new discontinuous nonconforming numerical implementations of the EFIE and PMCHWT formulations for infinitely long homogeneous bodies, and of the EFIE-PMCHWT formulation for infinitely long piecewise homogeneous structures, with PEC or penetrable regions. Our tests with 2D objects, penetrable or PEC, with triangular or square sections, suggest that the discontinuous TE-analysis of sharp-edged PEC targets or penetrable objects with moderate or high dielectric contrasts (above 10) with sharp wedges and corners, shows improved accuracy, versus the number of unknowns, with respect to the conventional schemes. Indeed, while the continuous piecewise linear implementations exhibit for the objects tested around $\mathcal{O}(h^{1.5})$ decrease in RCS or near-field errors, our nonconforming implementations exhibit smaller errors and decrease rates around $\mathcal{O}(h^{1.7})$ with an adequate choice of the height H of the testing elements. Our tests show, as a general trend, that the best performing H-ranges lie roughly between $h/10$ and $h/100$. The well-performing H-range rises, in the TE-scattering analysis, as the relative permittivity increments and the target becomes sharper. The improvements in the near- and far-field results are especially noticeable for the electrically small sharp-edged targets since in these cases the correct modelling of singular fields near sharp vertices play an important role in the overall accuracy of the results.

Our discontinuous numerical implementations of TM-PMCHWT for the 2D magnetic objects with moderate or high relative permeabilities show equal performance to our discontinuous TE-PMCHWT schemes in the analysis of the 2D dielectric targets and moderate or high dielectric contrasts, since the two implementations are dual to each other. We have used this fact to improve the accuracy in the scattering analysis of infinitely long ferromagnetic objects.

We attribute the observed improved TE-performance for sharp-edged high-contrast dielectrics or PEC targets, or TM-performance for sharp-edged high relative permeability objects to the better characterization of the singular-fields thanks to the discontinuous transition of the expanded currents at corner nodes and the convenient field testing inside the null-field regions of the associated homogeneous problems, especially over domains attached to corners, so that the null-field conditions assumed in the surface equivalence theorem are better enforced. Consistently, the discontinuous TM-analysis of smooth and/or low relative permeability 2D targets or the discontinuous TE-analysis of smooth and/or low contrast dielectric sections, with no singular field behaviour, does not exhibit improved accuracy versus the number of unknowns when compared with the continuous analysis.

In any case, our discontinuous EFIE-PMCHWT implementations are very useful in practice in the analysis of composite objects with piecewise homogeneous regions. The conventional node-based continuous schemes require elaborate management of junction-nodes, where several regions intersect. In contrast, the use of segment-based discontinuous basis functions in our nonconforming schemes, with no required knowledge about nodes over the boundary, circumvents the inconvenient management of junction-nodes associated with the continuous schemes.

Chapter 5

Discontinuous Method of Moments Discretization of Integral Equations Applied to 3D Problems

5.1 Introduction

The ideas and conclusions generated in Chapter 4 for the special cases of infinitely long 2D objects are extended, in this chapter, to arbitrarily shaped 3D geometries. Infinitely long 2D geometries are an abstract concept and an idealization which can not be encountered in nature, however, their analysis is of paramount importance since the conclusions, in many cases, can be extrapolated to the more practically valuable 3D problems. The concept of a *node* and *segment* in the tessellation of 2D cylinders extends to the *edge* and *facet* in the mesh of arbitrarily shaped geometries. Although a mesh of a single 2D target is always geometrically conformal (all the inner nodes are sharing two segments), a mesh of an object with an arbitrary shape can be geometrically nonconformal (two adjacent facets have more than one edge in common). Nonconformal meshes are more flexible than conformal counterparts since the two adjacent (flat) facets do not have to be connected with the same pair of vertices and share a common edge. Nonconformal meshes usually arise in the modular design of objects by juxtaposing open independently meshed triangulations. They also may be generated by a simple mistake in the construction of a conformal mesh, i.e. the two neighbouring facets may not be well connected and/or spurious slits may arise between the adjacent mesh elements. Standard edge-based divergence-conforming schemes can not be applied on a nonconformal mesh, hampering the versatility and the flexibility of integral equation schemes. For that reason, often a tedious and time-consuming task has to be undertaken in order to transform the nonconformal mesh to the geometrically conformal mesh, which is not always fruitful. Clearly, an integral equation scheme able to operate on conformal as well as nonconformal meshes would be a great asset.

In this chapter, we address the robust, accurate and versatile single-surface scattering analysis of PEC and penetrable objects with arbitrary shape and composite objects with junctions. For this, we employ the EFIE–PMCHWT integral-equation formulation [48], which follows from the application of the EFIE or PMCHWT formulations over boundary surfaces, respectively, enclosing PEC regions or separating penetrable regions. The proposed schemes rely on the expansion of the currents with the facet-based, discontinuous-

across-edges, monopolar-RWG set [11]. Similarly to the 2D problems, this discretization choice gives rise to integrals with hypersingular kernels, which we successfully handle with *volumetric* or *surface tangential-normal* testing schemes. The volumetric scheme of testing defines the testing functions over small volumetric domains, tetrahedral elements or wedges, attached to the boundary surface and lying in the region where the fields are zero according to the surface equivalence theorem. The surface tangential-normal scheme deploys RWG testing functions over pairs of adjacent triangles such that one triangle matches a boundary triangle and the other one is quasi-normally oriented into the null-field region. These implementations are nonconforming to the natural divergence function spaces since the finite-dimensional space spanned by the monopolar-RWG functions belongs to the space of square integrable functions, $L^2(\Gamma)$ [53]. However, similarly to the results presented in the previous chapter, our discontinuous implementations of EFIE and PMCHWT offer improved accuracy compared to standard RWG schemes in the scattering analysis of subwavelength sharp-edged PEC or penetrable targets. In the cases of penetrable objects, the relative permittivity/permeability has to be moderate or high in order for singular fields to be induced around sharp wedges and corners. A special case is the correct modelling of plasmonic subwavelength nanoparticles with sharp wedges and corners in the resonance domain, which requires the correct singular representation of the *localized surface plasmons*. Moreover, our discontinuous schemes manifest in general great flexibility in the single-surface analysis of composite objects with junctions as the special modelling of currents at junctions is not required. Also, as we will show in this chapter, the proposed implementations can handle nonconformal meshes when applied to piecewise (or fully) homogeneous arbitrarily shaped objects. Our schemes become also well suited for the enhancement of integral equation domain decomposition methods [31], [32], since the transmission conditions between contiguous subdomains may be satisfied through the off-boundary testing and the discontinuous monopolar-RWG expansion.
The concepts introduced in this chapter were partially published in [54], [55], [56] (Section 5.2), [57], [59], [60], [62], [63], [84] (Section 5.3 and Section 5.4), and [33] (Section 5.5).

5.2 Discontinuous discretization of the EFIE for conductors

We expand the electric current $\boldsymbol{J}$ over the boundary-surface of a PEC object with facet-based monopolar-RWG basis functions [11] $\boldsymbol{m}_n^p \in L^2(\Gamma)$ as follows

$$\boldsymbol{J} \simeq \sum_{p=1}^{3} \sum_{n=1}^{N_t} J_n^p \boldsymbol{m}_n^p \tag{5.1}$$

where N_t denotes the number of triangular facets arising from the polygonal representation of the boundary-surface and $\{J_n^p\}$ denotes the set of unknown coefficients associated with the expansion of the electric current. The monopolar-RWG and RWG basis functions share the same definition inside each triangle [11]. However, whereas the RWG set is edge-based, with a normally continuous transition across edges, the monopolar-RWG set is facet-based, with no continuity imposition across edges. In consequence, for a given closed triangulation, the RWG discretization handles as many unknowns as the number of edges, while the monopolar-RWG set gives rise to twice this amount of unknowns or,

equivalently, three times the number of triangles. The subsets $\{\boldsymbol{m}_n^1\}$, $\{\boldsymbol{m}_n^2\}$ and $\{\boldsymbol{m}_n^3\}$ denote the three monopolar-RWG contributions sharing the nth triangle S_n arising in the surface tessellation so that

$$\boldsymbol{m}_n^p(\boldsymbol{r}') = \frac{1}{2A_n}(\boldsymbol{r}' - \boldsymbol{r}_n^p), \quad \boldsymbol{r}' \in S_n \quad p = 1, 2, 3 \tag{5.2}$$

where $\boldsymbol{r}_n^1$, $\boldsymbol{r}_n^2$ and $\boldsymbol{r}_n^3$ represent the position vectors of the three vertices of S_n with area A_n. The approximated scattered electric field $\tilde{\boldsymbol{E}}_s$ radiated by the monopolar-RWG expansion of the current in (5.1) becomes

$$\tilde{\boldsymbol{E}}_s = \sum_{n=1}^{N_t} \eta \boldsymbol{\mathcal{T}}_n^p J_n^p \tag{5.3}$$

where the discretized monopolar-RWG electric field integral operator $\boldsymbol{\mathcal{T}}_n^p$ is defined as

$$\boldsymbol{\mathcal{T}}_n^p = \frac{1}{jk}\big[\nabla\nabla\cdot \iint_{S_n} G(\boldsymbol{r}, \boldsymbol{r}')\boldsymbol{m}_n^p(\boldsymbol{r}')dS' + k^2 \iint_{S_n} G(\boldsymbol{r}, \boldsymbol{r}')\boldsymbol{m}_n^p(\boldsymbol{r}')dS'\big] \tag{5.4}$$

The constants k and η represent the wave number and the impedance of the surrounding medium (usually free space), and G stands for the associated Green's function. The discretization of the EFIE with the monopolar-RWG basis functions is then defined on the meshed surface of the PEC target by invoking the tangential electric boundary condition as follows

$$\gamma_t \tilde{\boldsymbol{E}}_s = \sum_{n=1}^{N_t} \eta \gamma_t \boldsymbol{\mathcal{T}}_n^p J_n^p = -\gamma_t \boldsymbol{E}_{inc} \tag{5.5}$$

where $\boldsymbol{E}_{inc}$ stands for the incident time-harmonic electric field. We transform the discretized equation (5.5) into a matrix form by testing the tangential electric field with a set of testing functions. The commonly used Galerkin scheme leads to

$$\iint_{S_m} \eta \boldsymbol{m}_m^q(\boldsymbol{r}) \cdot \boldsymbol{\mathcal{T}}_n^p J_n^p dS = -\iint_{S_m} \boldsymbol{m}_m^q(\boldsymbol{r}) \cdot \boldsymbol{E}_{inc} dS, \quad q = 1, 2, 3 \quad 1 \leqslant n, m \leqslant N_t \tag{5.6}$$

However, since monopolar-RWG basis functions are not divergence- conforming, the Galerkin testing of the hypersingular part of the electric field integral operator, which is related to the gradient of electric scalar potential, leads to the following identity

$$\begin{aligned}
&\iint_{S_m} \boldsymbol{m}_m^q \cdot \big[\nabla\nabla\cdot \iint_{S_n} G(\boldsymbol{r}, \boldsymbol{r}')\boldsymbol{m}_n^p dS' dS\big] = -\iint_{S_m} \nabla\cdot \boldsymbol{m}_m^q \iint_{S_n} G\nabla'\cdot \boldsymbol{m}_n^p dS' dS \\
&+ \int_{l_m^q} \boldsymbol{m}_m^q \cdot \hat{n}_c^m \iint_{S_n} G\nabla'\cdot \boldsymbol{m}_n^p dS' dl + \iint_{S_m} \nabla\cdot \boldsymbol{m}_m^q \int_{l_n^p} G\boldsymbol{m}_n^p \cdot \hat{n}_c^n dl' dS \\
&- \int_{l_m^q} \boldsymbol{m}_m^q \cdot \hat{n}_c^m \int_{l_n^p} G\boldsymbol{m}_n^p \cdot \hat{n}_c^n dl' dl
\end{aligned} \tag{5.7}$$

In (5.7) l_m^q and l_n^p represent the edges opposite to the qth or the pth vertex in the field and the source triangles, respectively, with the corresponding unit normals $\hat{n}_c^m$ and $\hat{n}_c^n$

perpendicular to them. The double-surface and the contour-surface integrals appearing in (5.7) are easy-to-manage through well-known integration routines but, unfortunately, the double contour integral becomes unbounded as the field and the source points approach on the same line. In the integral equation discontinuous Galerkin (IEDG) method [53], Zhen Peng et al. avoid the direct computation of the troublesome integral by introducing two *penalty terms*. The first penalty term exactly cancels out the double-contour integral and the second one is introduced to weakly enforce the continuity of the current across the neighbouring mesh elements. The second penalty term comes with multiplicative factor β, dubbed *the interior penalty stabilization function*, which directly depends on the mesh size. However, the accuracy of the results and the stability of the formulation are greatly influenced by the choice of β, which often changes from case to case. Moreover, the second penalty term, which relies on the contour integrals between adjacent facets, is complicated to implement for geometrically nonconformal elements [64]. Finally, the accuracy of IEDG, when the interior stabilization function is well adjusted, is comparable to the RWG scheme but doubling the number of degrees of freedom.
In this chapter, we introduce two non-Galerkin testing schemes, volumetric and surface tangential-normal, carefully designed in order to transform the problematic double-contour integral into integrals with a lower degree of kernel singularity, readily computable with standard singularity subtraction techniques [85], [86]. From the practical point of implementation, our schemes are more complicated than IEDG method since additional contour or volumetric integrals have to be computed. Nonetheless, our discontinuous schemes are more flexible, especially for nonconformal meshes, since no additional contour penalty term has to be computed. Furthermore, our implementations produce more accurate results, in the number of unknowns, compared to RWG schemes, in the analysis of challenging problems involving singular fields.

5.2.1 Volumetric testing

The monopolar-RWG radiated scattered electric field is tested through a set of functions defined over a set of tetrahedral or wedge elements. Each volumetric element is attached to the particular boundary facet arising in the mesh and lying inside the PEC target where the fields are zero. The testing elements can be defined *conformal* or *nonconformal* to the meshed boundary. In the first case, the volumetric elements are shaped by the planes bisecting the angles formed by the corresponding field triangle and the three adjacent triangles. In the latter case, the definition of volumetric elements depends only on the field triangle where the element is attached. This choice appears as particularly flexible and versatile because no a priori knowledge of the boundary shape is required and because nonconformal meshes can be handled. However, for triangles with an edge touching a sharp corner, the testing element will break out of the null-field region and some numerical error may appear.

- *Tetrahedral testing functions*

  We define the volumetric tetrahedral testing functions as (see Fig. 5.1)

$$\boldsymbol{v}_m^q(\boldsymbol{r}) = \frac{1}{2A_m H_m^q}(\boldsymbol{r} - \boldsymbol{r}_m^q), \quad \boldsymbol{r} \in V_m^q \quad q = 1,2,3 \quad 1 \leqslant m \leqslant N_t \tag{5.8}$$

where H_m^q denotes the height of the qth tetrahedron associated with the field triangle S_m, defined as a fraction of the mesh parameter h_m^q, which represents the length of the qth side of the field triangle S_m. A_m denotes the area of S_m and $\boldsymbol{r}_m^q$ represents the position vector of the qth side of the field triangle's vertex (see Fig. 5.1). The volumetric testing functions are defined locally, inside the tetrahedral elements, in the same manner as the SWG functions [88], but without normal continuity imposition across common faces. Therefore, we call them *monopolar-SWG* testing functions. The triangle opposite to the vertex $\boldsymbol{r}_m^q$, in the definition of conformal testing tetrahedra, lies in the plane bisecting the angle between two adjacent triangles, while in the definition of nonconformal elements, this triangle is perpendicular to field facet.

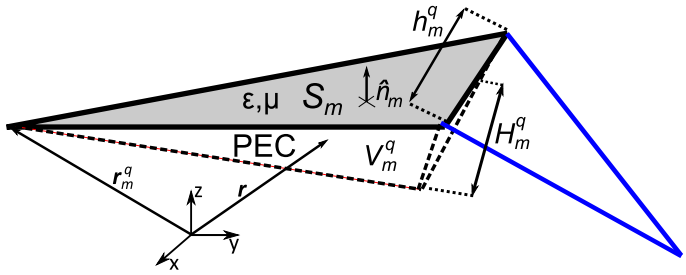

Figure 5.1: Volumetric testing over the tetrahedral element V_m^q attached to the mesh element S_m and lying inside PEC object (conformal to the boundary). The height of the testing tetrahedral element H_m^q is defined as a fraction of h_m^q the length of the associated edge in S_m

- *Wedge testing functions*

We define the volumetric wedge testing functions as (see Fig. 5.2)

$$\boldsymbol{w}_m^q(\boldsymbol{r}) = \frac{1}{2A_m H_m}\Big[\boldsymbol{\rho}_m^q - (\boldsymbol{r}_m^q - \boldsymbol{r})\cdot\hat{n}_m \tan\alpha_m^q \cdot \hat{\rho}_m^q\Big], \qquad \boldsymbol{r}\in V_m^q \quad q=1,2,3 \quad 1\leqslant m\leqslant N_t \tag{5.9}$$

where $\boldsymbol{\rho}_m^q$ represents the projection of the vector $(\boldsymbol{r}-\boldsymbol{r}_m^q)$ onto the plane of the triangle S_m, and H_m is the height of the wedge associated with the field triangle S_m. This parameter is defined as a fraction of the mesh parameter, which we set as the average length of the side segments of S_m. The unit vector $\hat{n}_m$ is oriented normally with respect to S_m pointing outwards. The angle of the side edge of the mth wedge associated with the qth vertex with respect to $\hat{n}_m$ is denoted by α_m^q (see Fig. 5.2). For the wedge testing elements nonconformal to the boundary, $\alpha_m^q = 0$, whereby the second term on the right hand side of (5.9) disappears, and the testing elements become triangular prisms. Note how, for the case of tetrahedral elements, three different testing functions are defined on three different tetrahedrons ($V_m^q,\ q=1,2,3$) attached to the same triangle, while for the case of wedge elements, three different testing functions are defined on the same wedge ($V_m^q = V_m,\ q=1,2,3$) attached to the mesh facet (see Figs. 5.1, 5.2).

The volumetrically tested monopolar-RWG discretization of the EFIE leads to the following matrix system

$$\iiint_{V_m^q} \eta \boldsymbol{M}_m^q(\boldsymbol{r}) \boldsymbol{\mathcal{T}}_n^p J_n^p dV = -\iiint_{V_m^q} \boldsymbol{M}_m^q(\boldsymbol{r}) \boldsymbol{E}_{inc} dV, \qquad q = 1,2,3 \quad 1 \leqslant n,m \leqslant N_t \tag{5.10}$$

where the wedge or tetrahedral testing functions $\boldsymbol{M}_m^q$ are defined on wedge or tetrahedral domains V_m^q. The volumetrically tested hypersingular part of the EFIO is now

$$\begin{aligned} &\iiint_{V_m^q} \boldsymbol{M}_m^q \cdot \left[\nabla\nabla \cdot \iint_{S_n} G(\boldsymbol{r},\boldsymbol{r}') \boldsymbol{m}_n^p dS' dV\right] = -\iiint_{V_m^q} \nabla \cdot \boldsymbol{M}_m^q \iint_{S_n} G \nabla' \cdot \boldsymbol{m}_n^p dS' dV \\ &+ \iint_{S_m^q} \boldsymbol{M}_m^q \cdot \hat{n}_s^m \iint_{S_n} G \nabla' \cdot \boldsymbol{m}_n^p dS' dS + \iiint_{V_m^q} \nabla \cdot \boldsymbol{M}_m^q \int_{l_n^p} G \boldsymbol{m}_n^p \cdot \hat{n}_c^n dl' dV \\ &- \iint_{S_m^q} \boldsymbol{M}_m^q \cdot \hat{n}_s^m \int_{l_n^p} G \boldsymbol{m}_n^p \cdot \hat{n}_c^n dl' dS, \quad p,q = 1,2,3 \quad 1 \leqslant n,m \leqslant N_t \end{aligned} \tag{5.11}$$

where S_m^q represents a facet in the wedge or tetrahedron opposite to the qth vertex with the unit normal $\hat{n}_s^m$ perpendicular to it. All the integrals in (5.11) have weakly singular kernels, computable with classical singularity subtraction schemes [85], [86]. The accuracy of this implementation can be adjusted by varying the height of the volumetric testing elements H.

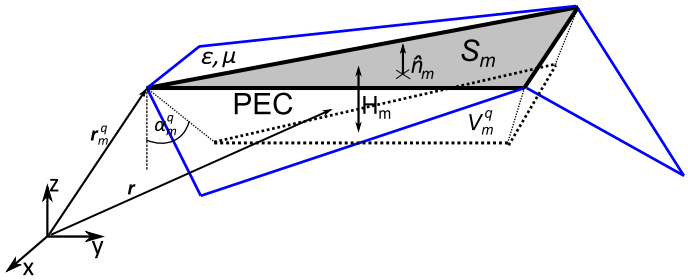

Figure 5.2: Volumetric testing over the wedge element V_m attached to the mesh element S_m and lying inside PEC object (conformal to the boundary). The height of the testing wedge element H_m is defined as a fraction of the mesh parameter, which we set as the average length of the side segments of S_m

5.2.2 Surface tangential-normal testing

The volumetric testing integrals in (5.11) are rather computationally expensive. In order to reduce this burden, we present an alternative, surface testing technique. The tangential fields are tested over a pair of edge-adjacent triangles such that one triangle matches a facet arising in the surface triangulation, and the other one is oriented quasi-normally inside the PEC target (see Fig. 5.3). This scheme can also be defined conformal or nonconformal to the boundary depending on whether the off-boundary triangle lies in the plane bisecting the angle between two edge-adjacent triangles or is oriented normally with respect to the matching triangle.

We define the tangential-normal testing functions as

$$\boldsymbol{t}_m^q(\boldsymbol{r}) = \begin{cases} \boldsymbol{f}_m^q(\boldsymbol{r}), & \boldsymbol{r} \in S_m \\ -\boldsymbol{g}_m^q(\boldsymbol{r}), & \boldsymbol{r} \in S_m^q, \quad q = 1,2,3 \quad 1 \leqslant m \leqslant N_t \end{cases} \tag{5.12}$$

where $\boldsymbol{f}_m^q(\boldsymbol{r})$ and $\boldsymbol{g}_m^q(\boldsymbol{r})$ denote the two RWG contributions, respectively, over the triangle S_m and over the triangle S_m^q, oriented along the bisecting plane inside the PEC target and defined as

$$\boldsymbol{g}_m^q(\boldsymbol{r}) = \frac{1}{2A_m^q}(\boldsymbol{r} - \boldsymbol{r}_m^{q,int}) \tag{5.13}$$

where $\boldsymbol{r}_m^{q,int}$ and A_m^q represent, respectively, the position vector of the interior off-boundary vertex and the area of S_m^q (see Fig. 5.3).

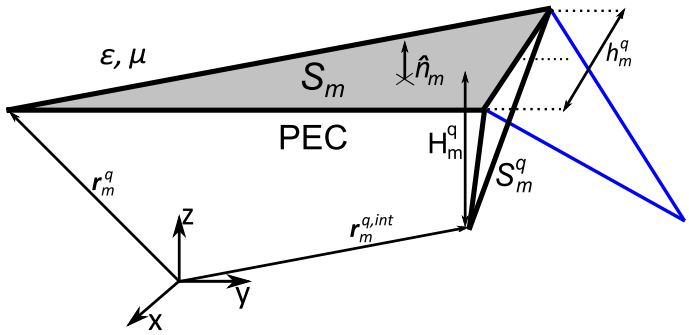

Figure 5.3: Tangential-normal testing over the pair of triangles $S_m \cup S_m^q$ defined conformal to the boundary. The height of the off-boundary element, H_m^q, is defined as a fraction of h_m^q, the length of the edge shared by S_m and S_m^q.

The monopolar-RWG discretization of the EFIE with tangential-normal testing gives rise to the following matrix system

$$\iint\limits_{S_m \cup S_m^q} \eta \boldsymbol{t}_m^q(\boldsymbol{r}) \boldsymbol{\mathcal{T}}_n^p J_n^p dS = -\iint\limits_{S_m \cup S_m^q} \boldsymbol{t}_m^q(\boldsymbol{r}) \boldsymbol{E}_{inc} dS, \qquad q = 1,2,3 \quad 1 \leqslant n, m \leqslant N_t \tag{5.14}$$

The hypersingular part of the EFIO tested with tangential-normal testing functions now becomes

$$\begin{aligned} \iint\limits_{S_m \cup S_m^q} \boldsymbol{t}_m^q \big[\nabla\nabla \cdot \iint_{S_n} G(\boldsymbol{r}, \boldsymbol{r}') \boldsymbol{m}_n^p(\boldsymbol{r}') dS' dV\big] &= -\iint\limits_{S_m \cup S_m^q} \nabla \cdot \boldsymbol{t}_m^q \iint_{S_n} G \nabla' \cdot \boldsymbol{m}_n^p dS' dS \\ + \iint\limits_{S_m \cup S_m^q} \nabla \cdot \boldsymbol{t}_m^q \int_{l_n^p} G \boldsymbol{m}_n^p \cdot \hat{n}_c^n dl' dS, \quad p,q = 1,2,3 \quad 1 \leqslant n, m \leqslant N_t \end{aligned} \tag{5.15}$$

and is in a considerably simpler form than the volumetrically tested counterpart due to the continuity of $\boldsymbol{t}_m^q$ across the common edge between the triangles S_m and S_m^q. Again, all the integrals in (5.15) have weakly singular kernels. Similarly to volumetric implementations, the accuracy of this implementation can be fine-tuned by adjusting the height H_m^q of the off-boundary testing triangle S_m^q, which we define as a fraction of h_m^q, the length of the shared edge between S_m and S_m^q.

5.2.3 Numerical results

In Section 5.2.3.1, we test the accuracy of our discontinuous discretizations of the EFIE on several canonical electrically small (subwavelength) sharp-edged PEC objects discretized with conformal meshes. Similarly to the 2D problems, we choose such targets, because singular or near-singular fields are induced around sharp edges and corners and our discontinuous schemes show accuracy improvements in the near-field and far-field regions compared to RWG implementation, EFIE[R], and the similar number of unknowns. In the scattering analysis of PEC targets with smooth boundaries where singular field behaviour does not occur [77], our schemes offer for a given meshing similar accuracy as the conventional RWG approach but doubling the number of degrees of freedom. As we will see in Section 5.2.3.1, the tangential-normal implementation of the EFIE, EFIE[tn], offers similar accuracy in near-field and far-field regions as our volumetrically tested implementations, EFIE[vol-wed](wedge tested discontinuous discretization of the EFIE) and EFIE[vol-tet](tetrahedrally tested discontinuous numerical implementation of the EFIE). Since the EFIE[tn] is considerably easier to implement than volumetric discontinuous discretizations, one may find the volumetric schemes useless. However, our volumetrically tested implementations offer better accuracy and stability in the analysis of nonconformal meshes, especially around spurious mesh defects like slits or cracks, which is a crucial advantage of facet-based methods when compared to the edge-based continuous techniques. The reason for this lies in the fact that tangential electric boundary condition is better enforced through volumetric testing, than with tangential-normal testing. Therefore, the nonconformal meshes will be analysed only with our volumetric implementations.
In Section 5.2.3.2 we prove the suitability of our volumetric monopolar-RWG EFIE implementations in the analysis of various single PEC targets discretized with nonconformal meshes, arising from the interconnection of different *open* triangulations, where the classical RWG-discretization cannot be adopted. Practically speaking, this choice makes sense because the modular analysis of multi-scale targets, of great interest nowadays, is often tackled through the interconnection of domains that are meshed with different mesh sizes according to local characteristics. The multi-trace continuous approach [30] can also analyse nonconformal meshes. However, these meshes have to be constructed from the interconnection of conformally meshed *closed* subdomains. Moreover, additional unknowns are assigned on the touching surfaces between the adjacent subdomains, which can dramatically increase the impedance matrix size for a problem of practical interest. The accuracy of our volumetric monopolar-RWG analysis of the single PEC objects meshed with geometrically nonconformal meshes is checked against the standard RWG-implementation and conformal meshing except for the sphere, for which the analytical solution is available [2].
We compute the volumetric integrals over wedges in our numerical tests through the decomposition of each wedge into three tetrahedral elements and the application of cuba-

ture rules of 11 points per tetrahedron. The surface and line integrals are computed with 9-point quadrature rules. The quasi-singular contributions of the kernel are computed analytically for the inner integrals of all the interactions. Whenever possible, for the sake of enhanced accuracy, the volumetric and surface field integrals are swapped with the line source integrals so that the well-known singularity subtraction techniques for triangles or tetrahedral elements [85] can be applied. In all the examples, the scattered fields are computed under an impinging $+z$ propagating x-polarized plane wave, and the free space wavelength λ_0 is set to 1m.

5.2.3.1 Conformal meshes

We test the accuracy of our monopolar-RWG EFIE-implementations on several small sharp-edged PEC targets; namely, a regular tetrahedron and a square pyramid, both with sides 0.1m long. We choose such testing examples because the singular field behaviour is observed at sharp edges and corners and, since the objects are electrically small, these singularities play an important role in the scattered fields.
We define the root-mean-square near-field relative error e_{near} as

$$e_{near} = \frac{\left[\sum_{j=1}^{K} |\tilde{\boldsymbol{E}}_s(\boldsymbol{r}_j) - \boldsymbol{E}_s^{REF}(\boldsymbol{r}_j)|^2 + \eta_0^2 \sum_{j=1}^{K} |\tilde{\boldsymbol{H}}_s(\boldsymbol{r}_j) - \boldsymbol{H}_s^{REF}(\boldsymbol{r}_j)|^2\right]^{1/2}}{\left[\sum_{j=1}^{K} |\boldsymbol{E}_s^{REF}(\boldsymbol{r}_j)|^2 + \eta_0^2 \sum_{j=1}^{K} |\boldsymbol{H}_s^{REF}(\boldsymbol{r}_j)|^2\right]^{1/2}} \tag{5.16}$$

where $\tilde{\boldsymbol{E}}_s$ and $\tilde{\boldsymbol{H}}_s$ denote the approximated scattered electric and magnetic fields computed with our EFIE implementations on a set of K points $\{\boldsymbol{r}_1....\boldsymbol{r}_K\}$ distributed around the target under analysis at very close distance (one tenth of the average mesh parameter adopted in the discretization for discontinuous implementations). Similarly, we compute the root-mean-square relative bistatic RCS-error e_{far} over a set of M observation angles $\{\theta_1....\theta_M\}$ in E and H plane as

$$e_{far} = \frac{\left[\sum_{j=1}^{M} |RCS_E(\theta_j) - RCS_E^{REF}(\theta_j)|^2 + \sum_{j=2}^{M-1} |RCS_H(\theta_j) - RCS_H^{REF}(\theta_j)|^2\right]^{1/2}}{\left[\sum_{j=1}^{M} |RCS_E^{REF}(\theta_j)|^2 + \sum_{j=2}^{M-1} |RCS_H^{REF}(\theta_j)|^2\right]^{1/2}} \tag{5.17}$$

where $\theta_1 = 0$ and $\theta_M = \pi - \pi/M$. All the errors are computed with respect to reference results (REF) obtained with the conventional RWG-implementation of the EFIE and very fine unstructured mesh (around 16300 triangles per target) with h-refinement near sharp edges and corners. The source integrals in the evaluation of near fields are computed with singularity subtraction technique and 9-point quadrature rules, while the integrals involved in the far-field expressions are computed with a three-point rule. In our numerical tests, we adopt $K = 400$ and $M = 60$, and all the testing elements in the monopolar-RWG implementations are defined conformal to the boundary to ensure maximum accuracy.

- *Accuracy versus H*

In Figs. 5.4-5.7 we show the normalized errors of our monopolar-RWG EFIE-implementations, for the PEC square pyramid (Figs. 5.4 and 5.6) and the PEC regular tetrahedron (Figs. 5.5 and 5.7). We define the normalized RCS-error in Figs. 5.4 and 5.5 similarly to the definitions for 2D problems (4.20) as

$$\bar{e}^{tn}_{far} = \frac{e^{tn}_{far}}{e^{R}_{far}}, \quad \bar{e}^{vol}_{far} = \frac{e^{vol}_{far}}{e^{R}_{far}} \tag{5.18}$$

and, analogously, the normalized near-field error in Figs. 5.6 and 5.7 as

$$\bar{e}^{tn}_{near} = \frac{e^{tn}_{near}}{e^{R}_{near}}, \quad \bar{e}^{vol}_{near} = \frac{e^{vol}_{near}}{e^{R}_{near}} \tag{5.19}$$

where the far-field errors e^{tn}_{far}, e^{vol}_{far} and the near-field errors e^{tn}_{near}, e^{vol}_{near} correspond to the definitions in (5.17) and (5.16), respectively, for the tangential-normal or volumetric EFIE implementations. Analogously, e^{R}_{far} and e^{R}_{near} denote the far-field and near-field errors computed with the RWG-discretization of the EFIE formulation and the similar number of unknowns as the monopolar-RWG implementations. Hence, our discontinuous implementations, which double the number of unknowns with respect to the continuous implementation, make use of a coarser mesh. Also, note how the normalized errors in Figs. 5.4–5.7 are plotted with respect to the height of the testing domains H, which in turn is set as a fraction of the mesh parameter h. In view of the definition of the normalized errors in (5.18) and (5.19), there is an improvement in far-field or near-field performance of the monopolar-RWG implementations with respect to the RWG-scheme as long as the corresponding normalized error, which is defined as the ratio between their respective relative errors, is smaller than one.

According to Figs. 5.4 and 5.5, our monopolar-RWG implementations outperform the conventional RWG implementation in the far-field computation over the following H-ranges: between $H = h/1000$ and $H = h$ (tangential-normal), between $H = h/1e4$ and $H = h/20$ (wedge-volumetric) or between $H = h/10$ and $H = h$ (tetrahedral-volumetric). Our best performing monopolar-RWG implementations (in terms of H) provide far-field normalized errors around five to ten times smaller than the normalized errors observed for EFIE[R] and the similar number of unknowns. Similarly, in light of Figs. 5.6 and 5.7, improved performance in the computation of the near fields is observed for the H-ranges between hand $h/1e4$ in all cases and the best normalized errors of our monopolar-RWG implementations, in terms of H, are around five times smaller than the normalized errors obtained with EFIE[R] and the similar number of unknowns.

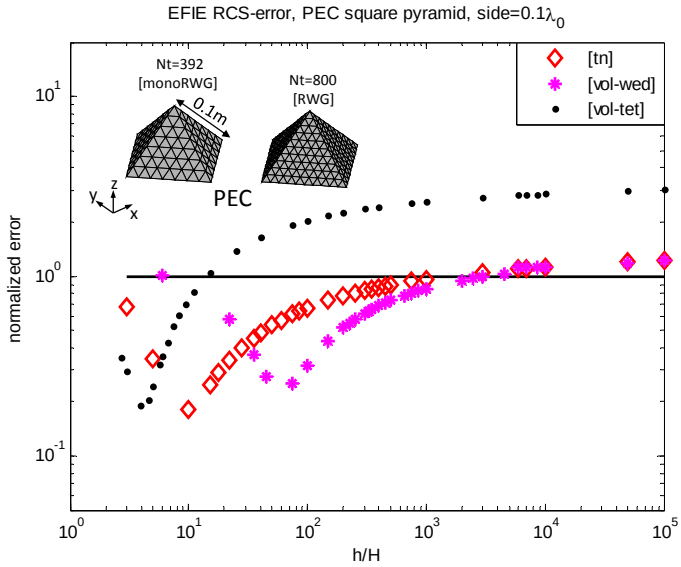

Figure 5.4: Normalized RCS error (5.18) computed for several nonconforming EFIE implementations, relative to EFIE[R], and the similar number of unknowns (around 1200) versus the height H of the testing domains for PEC square pyramid with side $0.1\lambda_0$ (λ_0=1m). The reference results are computed with EFIE[R] and very fine mesh (around 16300 facets)

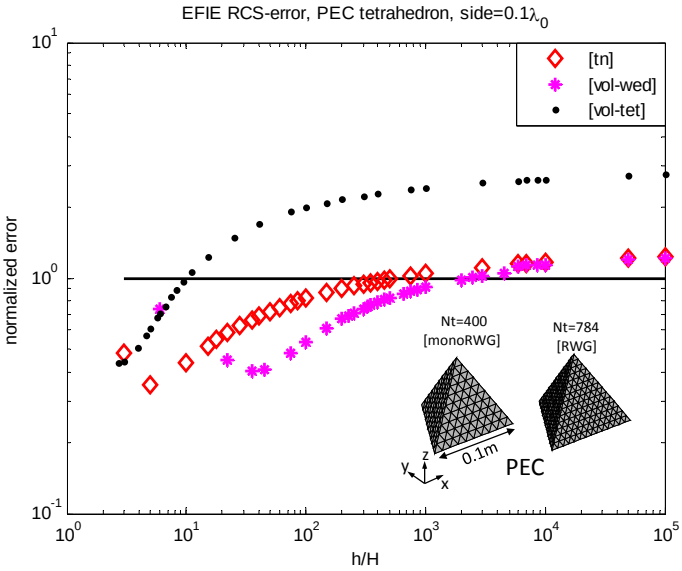

Figure 5.5: Normalized RCS error (5.18) computed for several discontinuous EFIE numerical implementations, relative to EFIE[R], and the similar number of unknowns (around 1200) versus the height H of the testing domains for PEC tetrahedron with side $0.1\lambda_0$ (λ_0=1m). The reference results are computed with EFIE[R] and very fine mesh (around 16300 facets)

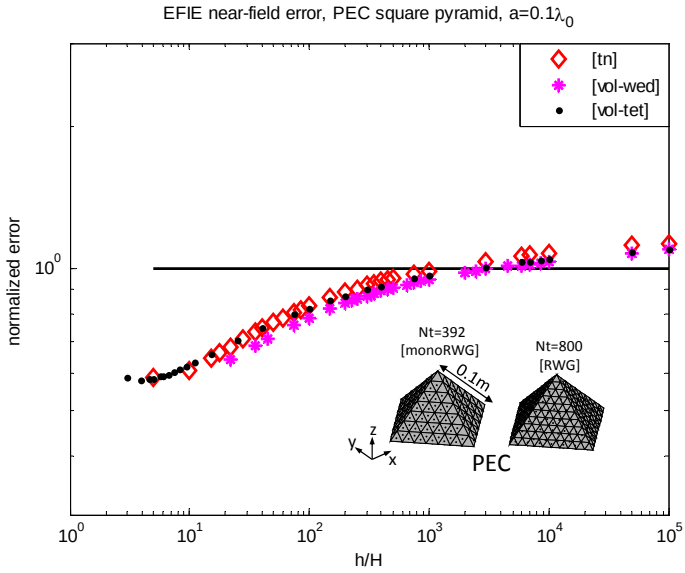

Figure 5.6: Normalized near-field error (5.19) computed for several discontinuous EFIE implementations, relative to EFIE[R], and the similar number of unknowns (around 1200) versus the height H of the testing domains for PEC square pyramid with side $0.1\lambda_0$ (λ_0=1m). The reference results are computed with EFIE[R] and very fine mesh (around 16300 facets)

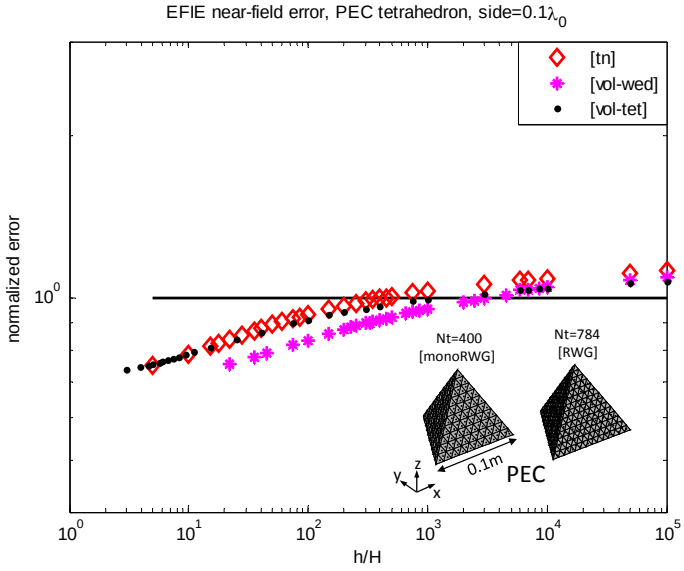

Figure 5.7: Normalized near-field error (5.19) computed for several discontinuous EFIE implementations, relative to EFIE[R], and the similar number of unknowns (around 1200) versus the height H of the testing domains for PEC tetrahedron with side $0.1\lambda_0$ (λ_0=1m). The reference results are computed with EFIE[R] and very fine mesh (around 16300 facets)

- *Accuracy versus N*

We show the relative far-field and near-field errors, with respect to the number of unknowns N, for the same two examples of perfectly conducting targets (square pyramid and tetrahedron with sides $0.1\lambda_0$). The height of the testing domains H is chosen from the range of best performing heights displayed in Figs. 5.4–5.7.

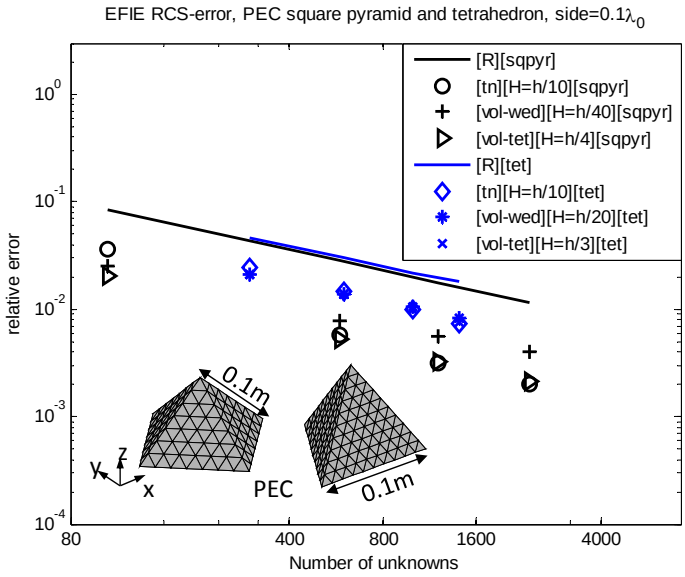

Figure 5.8: Relative RCS error (5.17) computed for several nonconforming EFIE implementations, versus the number of unknowns N for PEC square pyramid and tetrahedron and side $0.1\lambda_0$ (λ_0=1m). The reference results are computed with EFIE[R] and very fine meshing (around 16300 triangles).

For all those examples the far-field and near-field errors observed for our monopolar-RWG implementations are smaller than the errors exhibited by the RWG-implementation.

In Fig. 5.8, for the case of PEC square pyramid, we observe a decrease in the RCS-error around $\mathcal{O}(h^{0.3})$ for all implementations. For the case of PEC tetrahedron (Fig. 5.8) the reduction in the far-field error is around $\mathcal{O}(h^{1.3})$ for all schemes. In light of Fig. 5.9, all the implementations exhibit a reduction in the near-field errors around $\mathcal{O}(h^{0.4})$.

Analogously to the continuous-discontinuous hybrid TE-EFIE discretization for the analysis of single targets meshed with conformal meshes, monopolar-RWG basis functions and the off-boundary testing (tangential-normal or volumetric) can be applied only on the edges forming physical sharp edges and corners and the standard RWG basis functions elsewhere. By this choice, we maintain the accuracy of the fully discontinuous implementations and at the same time drastically reduce the number of degrees of freedom. Our hybrid EFIE implementations appear as an optimal and very accurate tool in the analysis of sharp-edged PEC targets.

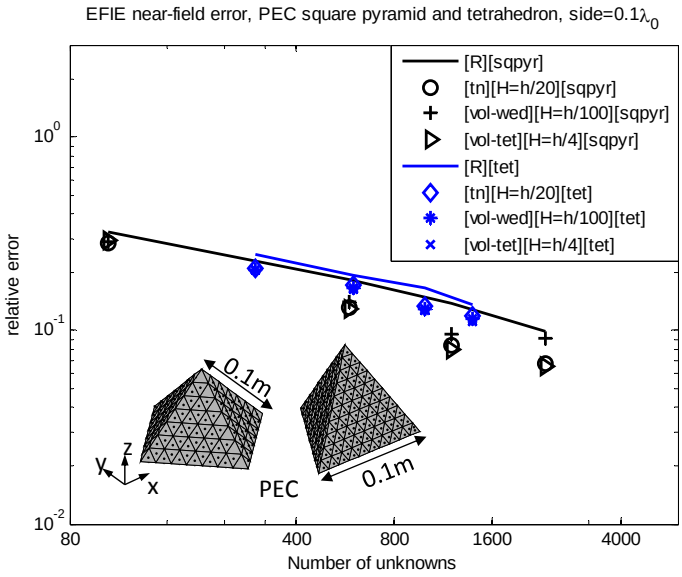

Figure 5.9: Relative near-field error (5.16) computed for several nonconforming EFIE implementations, versus the number of unknowns N for PEC square pyramid and tetrahedron and side $0.1\lambda_0$ (λ_0=1m). The reference results are computed with EFIE[R] and very fine meshing (around 16300 facets).

5.2.3.2 Nonconformal meshes

In this section, we present the scattering analysis of two PEC targets meshed with geometrically nonconformal meshes with our volumetric discontinuous EFIE discretizations. In Fig. 5.10 we show the bistatic RCS and the normalized absolute value of surface electric current for a PEC sphere with radius $r = 0.5\lambda_0$. Furthermore, on Fig. 5.11, we plot the bistatic RCS and the normalized absolute value of electric current for a PEC target consisting of a cube and a regular square pyramid with side $0.4\lambda_0$. These meshes are formed by juxtaposing independently meshed open triangulations, and as such, can not be analysed with RWG-scheme. For the case of a sphere, we compare our results with analytical Mie series solution [2], while for the cube-square pyramid we use a result computed with RWG discretization of the EFIE, conformal mesh and the similar number of unknowns as a reference. The testing domains in the monopolar-RWG volumetric EFIE implementations, for the sake of flexibility, are defined nonconformal to the boundary-surface.

Indeed, this definition depends only on the corresponding surface triangle, with no insight into the facets around, which is appropriate in general for geometrically nonconformal meshes. As for the height of volumetric testing elements H in the discontinuous analysis of the nonconformal PEC meshes we develop two strategies. If the connection between independently meshed subdomains contains slits (examples are curved objects like sphere or cone), the height of the testing elements should be bigger (in the range from $H = h/10$ to $H = h$) in order for the null-field to be better enforced around cracks. For the cases of connections without slits, any H choice from the range shown in Figs. 5.4 and 5.5 works satisfactory. In order to boost the efficiency and minimize the number of unknowns, we use

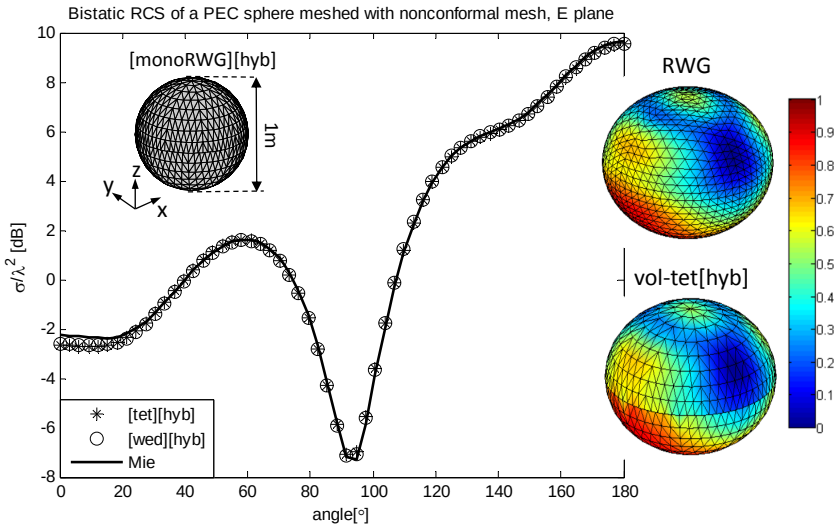

Figure 5.10: Bistatic RCS of a PEC sphere ($r = 0.5m$) and the normalized absolute value of the surface current under an impinging x-polarized z-propagating plane wave and λ_0=1m. The number of unknowns is 1700 for our hybrid monopolar-RWG EFIE-implementations. The Mie series solution is adopted as reference. Volumetric tetrahedral and volumetric-wedge implementations use $H = h/5$

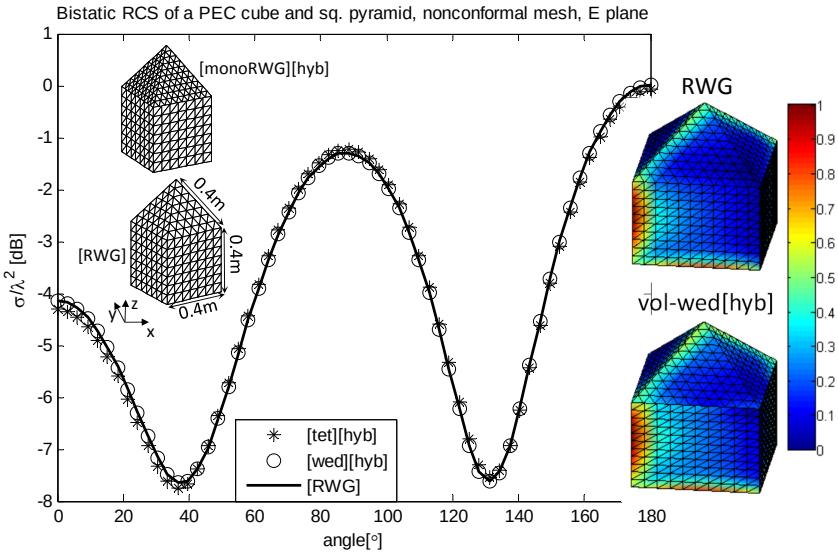

Figure 5.11: Bistatic RCS of a PEC object composed of cube and square pyramid with side $0.4m$ and the normalized absolute value of the surface current under an impinging x-polarized z-propagating plane wave and λ_0=1m. The number of unknowns is 2688 for our hybrid monopolar-RWG EFIE-implementations and 2772 for RWG implementation which is adopted as reference. Volumetric tetrahedral and volumetric-wedge implementations use $H = h/1e4$

the *hybrid* continuous-discontinuous formulation of our volumetric EFIE implementations. The hybrid EFIE schemes for nonconformal meshes use monopolar-RWG basis functions and volumetric testing only over the nonconformal part of the mesh, where adjacent triangles do not necessarily share a single edge, and RWG basis and testing functions elsewhere. Excellent agreement between the results is observed in both testing examples.

5.3 Discontinuous discretization of the PMCHWT for single penetrable targets

The scattering analysis of an arbitrarily shaped penetrable body immersed in a host medium is usually carried out through the equivalent definition of the original problem in terms of two homogeneous problems associated with each of the two regions, outside ($i = 1$) or inside ($i = 2$) the body (see Fig. 2.1). The scattered fields $\boldsymbol{E}_i^s$ and $\boldsymbol{H}_i^s$ are generated in the homogeneous problem associated with the region i by $\boldsymbol{J}_i$ and $\boldsymbol{M}_i$, respectively, the electric and magnetic currents defined at the side of the boundary surface Γ inside the region i. In light of the equivalence theorem, the total fields, resulting from the summation of the incident and scattered fields, are zero in the equivalent problem out of the corresponding regions (see Fig. 2.1). We expand the unknown surface currents, $\boldsymbol{J}_i$ and $\boldsymbol{M}_i$, with the monopolar-RWG set of basis functions (5.2) as follows

$$\boldsymbol{J}_i \simeq \sum_{p=1}^{3}\sum_{n=1}^{N_t} J_n^{p,i}\boldsymbol{m}_n^p \tag{5.20}$$

$$\boldsymbol{M}_i \simeq \sum_{p=1}^{3}\sum_{n=1}^{N_t} M_n^{p,i}\boldsymbol{m}_n^p \tag{5.21}$$

where $J_n^{p,i}$ and $M_n^{p,i}$ denote the sets of unknown coefficients in the expansion of the currents.

The approximated scattered fields generated in the homogeneous problem associated with the region i are defined as

$$\tilde{\boldsymbol{E}}_i^s = \sum_{n=1}^{N_t} \eta_i \boldsymbol{\mathcal{T}}_n^{p,i} J_n^{p,i} - \sum_{n=1}^{N_t} \boldsymbol{\mathcal{K}}_n^{p,i} M_n^{p,i} \tag{5.22}$$

$$\tilde{\boldsymbol{H}}_i^s = \sum_{n=1}^{N_t} \boldsymbol{\mathcal{K}}_n^{p,i} J_n^{p,i} + \sum_{n=1}^{N_t} \frac{1}{\eta_i} \boldsymbol{\mathcal{T}}_n^{p,i} M_n^{p,i} \tag{5.23}$$

with the associated integral operators defined as

$$\boldsymbol{\mathcal{T}}_n^{p,i} = -jk_i \iint_{S_n} G_i(\boldsymbol{r},\boldsymbol{r}')\boldsymbol{m}_n^p(\boldsymbol{r}')dS' - \frac{j}{k_i}\nabla\Psi_n^{p,i} \tag{5.24}$$

$$\boldsymbol{\mathcal{K}}_n^{p,i} = \nabla \times \iint_{S_n} G_i(\boldsymbol{r},\boldsymbol{r}')\boldsymbol{m}_n^p(\boldsymbol{r}')dS' \tag{5.25}$$

The scalar function $\Psi_n^{p,i}$, from which the discretized electric and magnetic scalar potentials are derived, is defined in general as [89]

$$\Psi_n^{p,i} = \iint_{S_n} G_i(\boldsymbol{r},\boldsymbol{r}')\nabla'\cdot\boldsymbol{m}_n^p(\boldsymbol{r}')dS' - \oint_{\partial S_n} G_i(\boldsymbol{r},\boldsymbol{r}')\boldsymbol{m}_n^p(\boldsymbol{r}')\cdot\hat{n}_c^n dl' \tag{5.26}$$

where ∂S_n and $\hat{n}_c^n$ denote, respectively, the closed contour around the source triangle and the unit vector perpendicular to this contour. The function G_i represents the Green's function of the homogeneous problem associated with the region i (2.23), and η_i and k_i are the impedance and the wave number of the homogeneous medium occupying region i.

The discretized PMCHWT formulation imposes the tangential electric-field and magnetic-field boundary conditions over the two sides ($i = 1, 2$) of the meshed boundary surface $\tilde{S} = \bigcup_{t=1}^{N_t} S_t$ so that

$$\gamma_t(\tilde{\boldsymbol{E}}_1^s - \tilde{\boldsymbol{E}}_2^s)_{\tilde{S}} = \sum_{n=1}^{N_t}\gamma_t(\eta_1\boldsymbol{\mathcal{T}}_n^1 + \eta_2\boldsymbol{\mathcal{T}}_n^2)_{\tilde{S}}J_n^p - \sum_{n=1}^{N_t}\gamma_t(\boldsymbol{\mathcal{K}}_n^1 + \boldsymbol{\mathcal{K}}_n^2)_{\tilde{S}}M_n^p \simeq -\gamma_t\boldsymbol{E}_{\tilde{S}}^{inc} \tag{5.27}$$

$$\gamma_t(\tilde{\boldsymbol{H}}_1^s - \tilde{\boldsymbol{H}}_2^s)_{\tilde{S}} = \sum_{n=1}^{N_t}\gamma_t(\boldsymbol{\mathcal{K}}_n^1 + \boldsymbol{\mathcal{K}}_n^2)_{\tilde{S}}J_n^p + \sum_{n=1}^{N_t}\gamma_t\left(\frac{1}{\eta_1}\boldsymbol{\mathcal{T}}_n^1 + \frac{1}{\eta_2}\boldsymbol{\mathcal{T}}_n^2\right)_{\tilde{S}}M_n^p \simeq -\gamma_t\boldsymbol{H}_{\tilde{S}}^{inc} \tag{5.28}$$

where $\boldsymbol{E}^{inc}$ and $\boldsymbol{H}^{inc}$ stand for the incident electric and magnetic fields, respectively, and the integral operators including differentiation should be interpreted in Cauchy principal value sense if the field point is on the surface of the target. The currents at both sides of the boundary-surface are related such that the tangential boundary conditions are satisfied; i.e. $J_n^p = J_n^{p,1} = -J_n^{p,2}$ and $M_n^p = M_n^{p,1} = -M_n^{p,2}$.

We cast the equations (5.27) and (5.28) into matrix form by testing the tangential field conditions with an appropriate set of testing functions. The commonly used Galerkin formulation, which adopts the same set for testing the fields and expanding the currents, gives rise to

$$\iint_{S_m}(\tilde{\boldsymbol{E}}_1^s - \tilde{\boldsymbol{E}}_2^s)\cdot\boldsymbol{m}_m^q(\boldsymbol{r})dS = -\iint_{S_m}\boldsymbol{E}^{inc}\cdot\boldsymbol{m}_m^q(\boldsymbol{r})dS \tag{5.29}$$

$$\iint_{S_m}(\tilde{\boldsymbol{H}}_1^s - \tilde{\boldsymbol{H}}_2^s)\cdot\boldsymbol{m}_m^q(\boldsymbol{r})dS = -\iint_{S_m}\boldsymbol{H}^{inc}\cdot\boldsymbol{m}_m^q(\boldsymbol{r})dS, \quad q = 1,2,3 \quad 1 \leqslant m \leqslant N_t \tag{5.30}$$

The integration by parts of the testing integrals involving gradient of scalar potentials, electric and magnetic, gives rise to double-contour integrals (5.7), which become unbounded for self-or edge-adjacent interactions. The penalty conditions derived in [53] can be applied to cancel out the problematic double-contour integrals appearing in (5.29) and (5.30) and to weakly enforce the continuity of the electric and magnetic currents across the adjacent mesh elements. However, to author's knowledge, this strategy (in the frequency domain) was applied only in the discontinuous Galerkin discretization of combined tangential formulation (CTF) [61]. In that work, the interior penalty stabilization function is set to zero, completely excluding the second penalty term, which weakly enforces continuity of the currents. The accuracy and stability of the discontinuous discretization

of CTF was explored manly on problems involving low contrast dielectrics, which are not very challenging since the singular fields are not induced around sharp wedges and corners.
Here, we adapt the non-Galerkin testing strategies introduced in our discontinuous discretization of the EFIE to the monopolar-RWG discretization of the PMCHWT. Since there are two equivalent problems involved now, the new testing functions have to be carefully designed in order to conform to the null-field condition arising from surface equivalence theorem. We test the performance of our discontinuous discretizations of PMCHWT on electromagnetically challenging problems, i.e. high relative permittivity contrast dielectrics, ferromagnetics, and plasmonic nanoparticles.

5.3.1 Volumetric testing

We test the scattered fields through a set of testing functions which we define over a set of wedge or tetrahedral elements attached to the boundary-surface inside the region i, where the null-field condition must be accomplished according to the equivalence principle (Fig. 5.12, 5.13). This scheme is analogous to the volumetric discontinuous EFIE numerical implementation for conductors introduced in section 5.2, where the volumetric testing domains are located inside the object. Equivalently to the volumetric elements used for the discontinuous discretization of the EFIE, the wedges or tetrahedra used in testing the discontinuous PMCHWT formulation can be defined either conformal or nonconformal to the boundary. In general, we use *conformal to the boundary* definition if we want maximum accuracy (analysis of single objects meshed with conformal meshes), and *nonconformal to the boundary* definition if we want to increase versatility (analysis of nonconformal meshes and piecewise homogeneous composite objects).
We define the volumetric tetrahedral testing functions over the two sides of the meshed boundary ($i = 1, 2$) analogously to the definition for PEC targets, as (see Fig. 5.12)

$$\boldsymbol{v}_m^{q,i}(\boldsymbol{r}) = \frac{1}{2A_m H_m^{q,i}}(\boldsymbol{r} - \boldsymbol{r}_m^q), \quad \boldsymbol{r} \in V_m^{q,i} \quad q = 1, 2, 3 \quad 1 \leqslant m \leqslant N_t \tag{5.31}$$

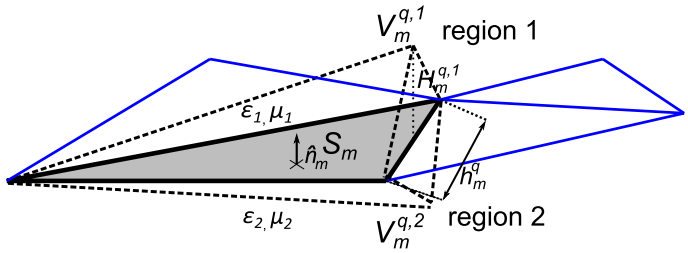

Figure 5.12: Volumetric testing over the tetrahedral elements $V_m^{q,i}$ attached to the mesh element S_m and defined conformal to the boundary. The height of the testing tetrahedral elements $H_m^{q,i}$ is defined as a fraction of h_m^q, the length of the associated edge in S_m, and with the same value at both sides of the surface

Alternatively, the volumetric wedge testing functions can be defined, similarly to (5.9) as (see Fig. 5.13)

$$\boldsymbol{w}_m^{q,i}(\boldsymbol{r}) = \frac{1}{2A_m H_m^i}\Big[\boldsymbol{\rho}_m^q - (\boldsymbol{r}_m^q - \boldsymbol{r})\cdot\hat{n}_m \tan\alpha_m^{q,i}\cdot\hat{\rho}_m^q\Big], \qquad \boldsymbol{r}\in V_m^{q,i} \quad q=1,2,3 \quad 1\leqslant m\leqslant N_t \tag{5.32}$$

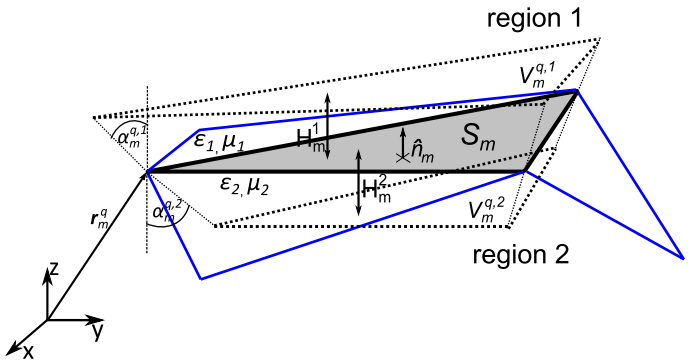

Figure 5.13: Volumetric testing over the wedge elements $V_m^{q,i}$ attached to the mesh element S_m and defined conformal to the boundary. The height of the testing wedge element H_m^i is defined as a fraction of the mesh parameter, which we set as the average length of the side segments of S_m, and with the same value at both sides of the boundary

The volumetrically tested monopolar-RWG discretization of the PMCHWT leads to the following matrix system

$$\iiint\limits_{V_m^{q,2}} \tilde{\boldsymbol{E}}_1^s\cdot\boldsymbol{M}_m^{q,2}(\boldsymbol{r})dV - \iiint\limits_{V_m^{q,1}} \tilde{\boldsymbol{E}}_2^s\cdot\boldsymbol{M}_m^{q,1}(\boldsymbol{r})dV = -\iiint\limits_{V_m^{q,2}} \boldsymbol{E}^{inc}\cdot\boldsymbol{M}_m^{q,2}(\boldsymbol{r})dV \tag{5.33}$$

$$\iiint\limits_{V_m^{q,2}} \tilde{\boldsymbol{H}}_1^s\cdot\boldsymbol{M}_m^{q,2}(\boldsymbol{r})dV - \iiint\limits_{V_m^{q,1}} \tilde{\boldsymbol{H}}_2^s\cdot\boldsymbol{M}_m^{q,1}(\boldsymbol{r})dV = -\iiint\limits_{V_m^{q,2}} \boldsymbol{H}^{inc}\cdot\boldsymbol{M}_m^{q,2}(\boldsymbol{r})dV \tag{5.34}$$

where again, equivalently to (5.10), the wedge or tetrahedral testing functions $\boldsymbol{M}_m^{q,i}$ are defined on wedge or tetrahedral domains $V_m^{q,i}$ on both sides of the tessellated boundary. Similarly to the volumetric discontinuous discretization of the EFIE, the problematic double-contour integrals arising in the Galerkin monopolar-RWG discretization of the EFIO are now avoided.
The accuracy of this implementation can be fine-tuned by adjusting the height of the volumetric testing elements.

5.3.2 Surface tangential-normal testing

The scattered electric and magnetic fields are tested over a pair of edge-adjacent triangles such that one triangle matches a facet arising in the surface triangulation, and the other one is oriented quasi-normally inside the region where the fields become zero according to the equivalence theorem (see Fig. 5.14). This scheme is analogous to the

tangential-normal discontinuous EFIE implementation introduced in (5.14) and can be defined conformal or nonconformal to the boundary. The testing integrals are now surface integrals, which alleviates the computational effort otherwise required for the volumetric integrals in (5.33) and (5.34).
We define the tangential-normal testing functions over the two sides of the boundary ($i = 1, 2$) analogously to the definition for PEC targets,

$$\boldsymbol{t}_m^{q,i}(\boldsymbol{r}) = \begin{cases} \boldsymbol{f}_m^q(\boldsymbol{r}), & \boldsymbol{r} \in S_m \\ -\boldsymbol{g}_m^{q,i}(\boldsymbol{r}), & \boldsymbol{r} \in S_m^{q,i}, \quad i = 1,2 \quad q = 1,2,3 \quad 1 \leqslant m \leqslant N_t \end{cases} \tag{5.35}$$

where $\boldsymbol{f}_m^q(\boldsymbol{r})$ and $\boldsymbol{g}_m^{q,i}(\boldsymbol{r})$ denote the two RWG contributions, respectively, over the triangle S_m and over the triangle $S_m^{q,i}$, oriented quasi-normally inside the region i (see Fig. 5.14) and defined as

$$\boldsymbol{g}_m^{q,i}(\boldsymbol{r}) = \frac{1}{2A_m^{q,i}}(\boldsymbol{r} - \boldsymbol{r}_m^{q,i}) \tag{5.36}$$

where $\boldsymbol{r}_m^{q,i}$ and $A_m^{q,i}$ represent, respectively, the position vector of the off-boundary vertex and the area of $S_m^{q,i}$ (see Fig. 5.14).

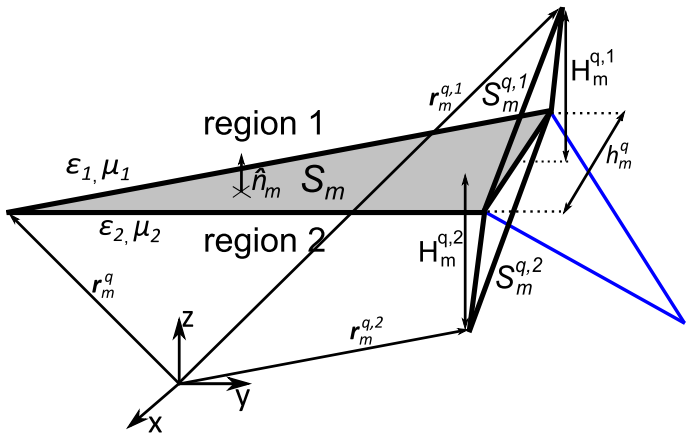

Figure 5.14: Tangential-normal testing over the pair of triangles $S_m \cup S_m^{q,i}$ defined conformal to the boundary. The height of the off-boundary element, $H_m^{q,i}$, is defined as a fraction of h_m^q, the length of the edge shared by S_m and $S_m^{q,i}$, with the same size on both sides

The monopolar-RWG discretization of the PMCHWT formulation with tangential-normal testing gives rise to the following matrix system

$$\iint\limits_{S_m \cup S_m^{q,2}} \tilde{\boldsymbol{E}}_1^s \cdot \boldsymbol{t}_m^{q,2}(\boldsymbol{r}) dS - \iint\limits_{S_m \cup S_m^{q,1}} \tilde{\boldsymbol{E}}_2^s \cdot \boldsymbol{t}_m^{q,1}(\boldsymbol{r}) dS = - \iint\limits_{S_m \cup S_m^{q,2}} \boldsymbol{E}^{inc} \cdot \boldsymbol{t}_m^{q,2}(\boldsymbol{r}) dS \tag{5.37}$$

$$\iint\limits_{S_m \cup S_m^{q,2}} \tilde{\boldsymbol{H}}_1^s \cdot \boldsymbol{t}_m^{q,2}(\boldsymbol{r}) dS - \iint\limits_{S_m \cup S_m^{q,1}} \tilde{\boldsymbol{H}}_2^s \cdot \boldsymbol{t}_m^{q,1}(\boldsymbol{r}) dS = - \iint\limits_{S_m \cup S_m^{q,2}} \boldsymbol{H}^{inc} \cdot \boldsymbol{t}_m^{q,2}(\boldsymbol{r}) dS \tag{5.38}$$

where the testing of the gradients of the scalar potentials can be simplified through

$$\iint\limits_{S_m \cup S_m^{q,i}} \boldsymbol{t}_m^{q,i} \cdot \nabla \Psi_n^{p,i} dS = - \iint\limits_{S_m \cup S_m^{q,i}} \Psi_n^{p,i} \nabla \cdot \boldsymbol{t}_m^{q,i} dS \tag{5.39}$$

because $\iint_{S_m \cup S_m^{q,i}} \nabla \cdot (\Psi_n^{p,i} \boldsymbol{t}_m^{q,i}) dS = 0$ thanks to the normal continuity of $\boldsymbol{t}_m^{q,i}$ across the common edge between the triangles S_m and $S_m^{q,i}$. The accuracy of this implementation is fine-tuned by adjusting the height $H_m^{q,i}$ of the testing triangle $S_m^{q,i}$, which we define with the same value in both regions as a fraction of h_m^q, the length of the qth side in S_m, which is shared with $S_m^{q,i}$ (see Fig. 5.14).

5.3.3 Numerical results

In Section 5.3.3.1, we focus on the scattering analysis with our single-surface monopolar-RWG PMCHWT-implementations of several single penetrable objects discretized with geometrically conformal meshes. Several schemes of testing are used: wedge volumetric, PMCHWT[vol-wed], tetrahedral volumetric, PMCHWT[vol-tet], or tangential-normal, PMCHWT[tn]. The accuracies are checked against the conventional RWG discretization of the PMCHWT, PMCHWT[R], which can be used because the adopted meshes are conformal. The tested objects have sharp edges and corners and moderate or high relative permittivity or permeability values because it is in these cases where the observed improved accuracy is especially evident. In the scattering analysis of penetrable targets with smooth boundaries and/or low relative permittivities/permeabilities, where singular field behaviour does not occur [77], our schemes offer for a given meshing similar accuracy as the conventional RWG approach but doubling the number of unknowns. Analogous observations have been reported in the scattering analysis of arbitrarily shaped conductors or 2D PEC or penetrable targets with our discontinuous implementations of the corresponding integral equations.
In Section 5.3.3.2 we show the suitability of our PMCHWT monopolar-RWG implementations in the analysis of various homogeneous penetrable objects discretized with nonconformal meshes, where the single-surface RWG-discretization cannot be adopted. Here we use only volumetrically tested discontinuous numerical implementations since better accuracy and stability was observed when compared to tangential-normal implementations. The accuracy of the volumetric monopolar-RWG techniques applied to the analysis of the single penetrable objects meshed with nonconformal meshes is checked against the standard RWG-implementation and conformal meshing except for the sphere, where the analytical solution is available [2]. The computation of volumetric, surface and line integrals is achieved with the same numerical routines as in the discontinuous volumetric discretization of the EFIE. In all the examples, the scattered fields are computed under an impinging $+z$ propagating x-polarized plane wave, and the free space wavelength λ_0 is set to 1m.

5.3.3.1 Conformal meshes

The accuracy of our discontinuous discretizations of the PMCHWT is tested on electrically small sharp-edged canonical targets: a tetrahedron and a square pyramid with side 0.1m and high relative permittivity/permeability constants. We chose such targets since singular fields are induced near sharp edges and corners, and the observed improvement of our schemes is especially remarkable.

The near-field and far-field relative errors, e_{near} and e_{far} are calculated with the expressions given in (5.16) and (5.17), respectively, identically as in the accuracy tests of our discontinuous discretizations of the EFIE. The source integrals in the evaluation of near fields are computed with singularity subtraction technique and 9-point quadrature rules, while the integrals involved in the far-field computations are computed with a three-point rule. All the testing elements are defined conformal to the boundary.

- *Accuracy versus H*

  In Figs. 5.15–5.18 we show the normalized errors of our monopolar-RWG PMCHWT-implementations, for the square pyramid (Figs. 5.15 and 5.17) and the regular tetrahedron (Figs. 5.16 and 5.18), and two moderately high dielectric contrasts ($\epsilon_r = 40$ and $\epsilon_r = 80$) for the square pyramid; ($\epsilon_r = 20$ and $\epsilon_r = 50$) for the regular tetrahedron. Furthermore, on Figs. 5.19 and 5.20, we show the normalized errors of our PMCHWT discretization schemes for a ferromagnetic square pyramid with side $0.1\lambda_0$. The normalized far-field and near-field errors are defined with the expressions (5.18) and (5.19), equivalently as for the PEC objects. For the comparison to be fair, our discontinuous implementations, which double the number of unknowns with respect to the continuous implementations, make use of a coarser mesh. We plot our errors with respect to the heights of volumetric testing entities, H. According to the definitions of normalized errors, (5.18) and (5.19), our discontinuous schemes show improvement in the near-field and far-field regions as long as the corresponding normalized error is smaller than one.

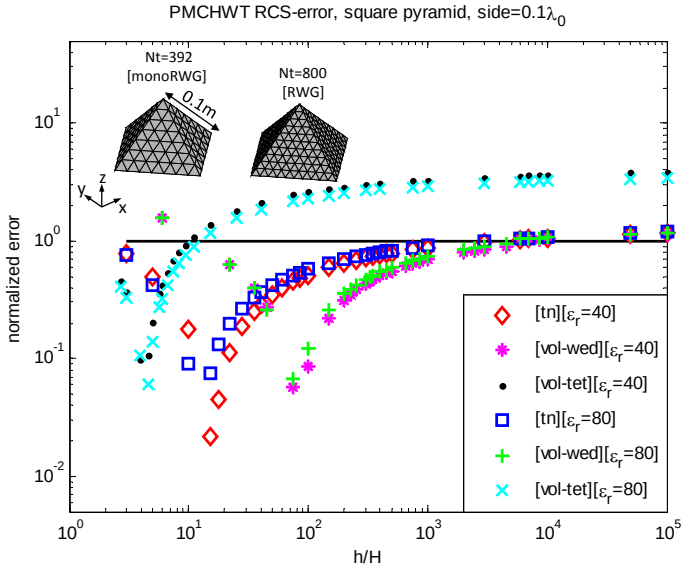

Figure 5.15: Normalized RCS-error (5.18) of our monopolar-RWG PMCHWT implementations, with respect to PMCHWT[R] and the similar number of unknowns (around 2400) versus the height H of the testing elements for a square pyramid with side $0.1m$ (λ_0=1m) and two relative permittivites (40 and 80). The reference results are obtained with PMCHWT[R] and a very fine mesh (around 16300 triangles)

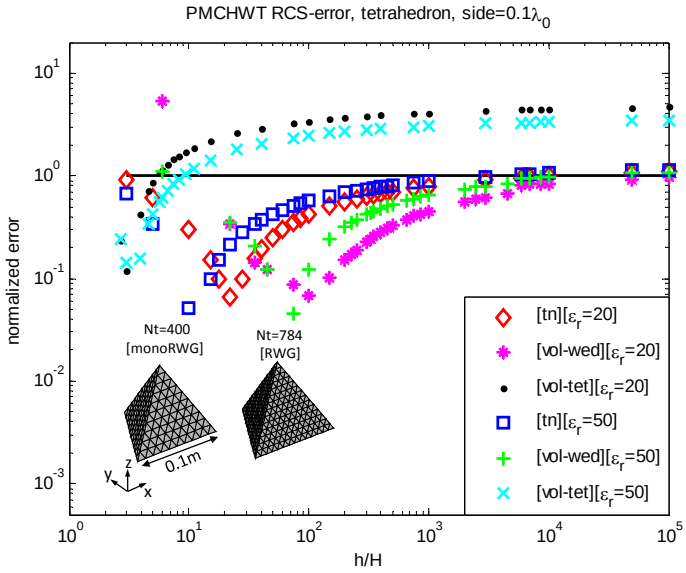

Figure 5.16: Normalized RCS-error (5.18) of our discontinuous PMCHWT numerical implementations, with respect to PMCHWT[R] and the similar number of unknowns (around 2400) versus the height H of the testing elements for a tetrahedron with side $0.1m$ (λ_0=1m) and two relative permittivites (20 and 50). The reference results are obtained with PMCHWT[R] and a very fine mesh (around 16300 triangles)

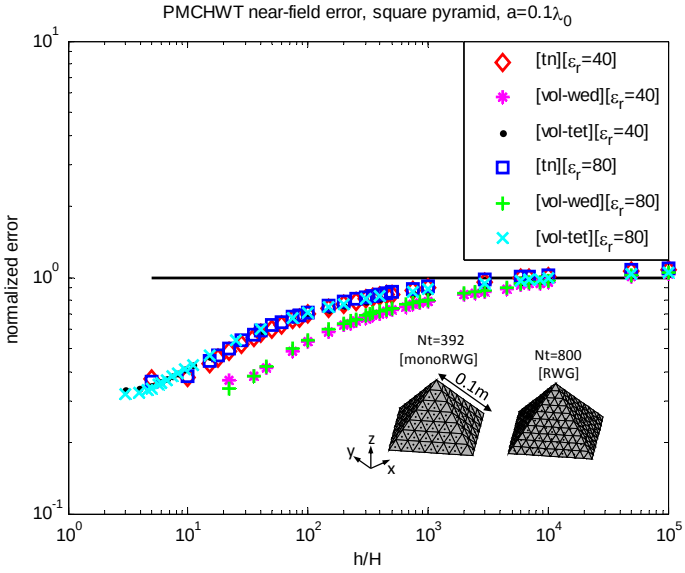

Figure 5.17: Normalized near-field error (5.19) of our discontinuous PMCHWT numerical schemes, with respect to PMCHWT[R] and the similar number of unknowns (around 2400) versus the height H of the testing elements for a square pyramid with side 0.1m (λ_0=1m) and two relative permittivites (40 and 80). The reference results are obtained with PMCHWT[R] and a very fine mesh (around 16300 triangles)

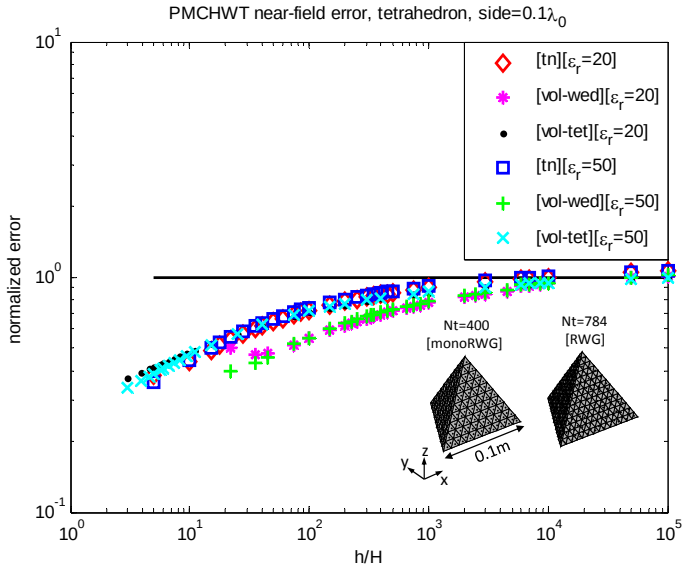

Figure 5.18: Normalized near-field error (5.19) of our monopolar-RWG PMCHWT implementations, with respect to PMCHWT[R] and the similar number of unknowns (around 2400) versus the height H of the testing elements for a tetrahedron with side 0.1m (λ_0=1m) and two relative permittivites (20 and 50). The reference results are obtained with PMCHWT[R] and a very fine mesh (around 16300 triangles)

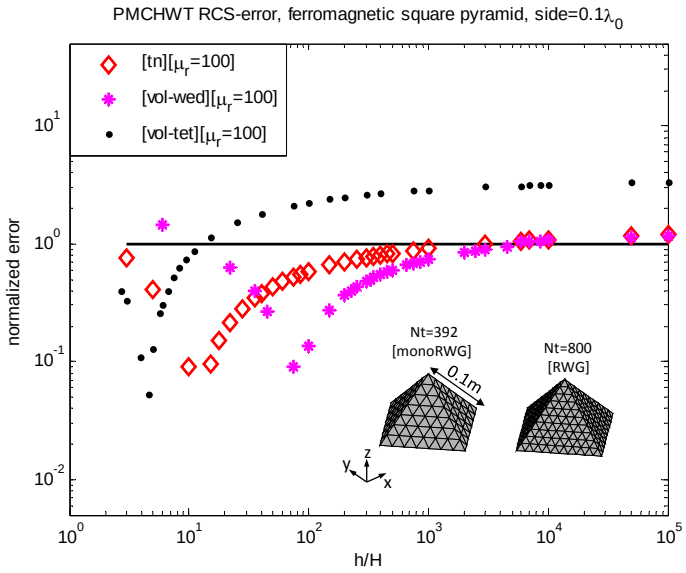

Figure 5.19: Normalized RCS-error (5.18) of our discontinuous PMCHWT implementations, with respect to PMCHWT[R] and the similar number of unknowns (around 2400) versus the height H of the testing elements for a ferromagnetic square pyramid with side 0.1m (λ_0=1m, $\mu_r = 100$). The reference results are obtained with PMCHWT[R] and a very fine mesh (around 16300 triangles)

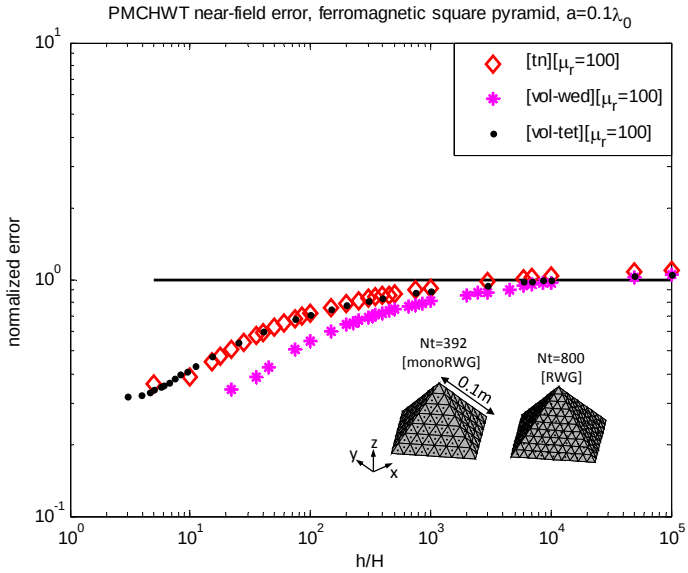

Figure 5.20: Normalized near-field error (5.19) of our discontinuous PMCHWT implementations, with respect to PMCHWT[R] and the similar number of unknowns (around 2400) versus the height H of the testing elements for a ferromagnetic square pyramid with side 0.1m (λ_0=1m, $\mu_r = 100$). The reference results are obtained with PMCHWT[R] and a very fine mesh (around 16300 triangles)

In light of Figs. 5.15, 5.16, and 5.19 the best performing H-ranges of our monopolar-RWG implementations in the far-field computation are: between $H = h/1000$ and $H = h$ (surface tangential-normal), between $H = h/1e5$ and $H = h/20$ (wedge-volumetric), or between $H = h/10$ and $H = h$ (tetrahedral-volumetric). The best performing discontinuous implementations (in terms of H) provide far-field normalized errors around 50 times smaller than the normalized errors computed with PMCHWT[R] and the similar number of unknowns. Similarly, in light of Figs. 5.17, 5.18, and 5.20 our discontinuous implementations show improved performance in the computation of the near fields for the H ranges between h and $h/1e4$ in all cases and the best performing monopolar-RWG implementations, with well chosen value of H, are around eight times smaller than the normalized errors obtained with PMCHWT[R] and the similar number of degrees of freedom.

- *Accuracy versus N*
  Here we present the relative far-field (Fig. 5.21) and near-field errors (Fig. 5.22), with respect to the number of unknowns N, for two sharp-edged targets with moderate dielectric contrasts and side $0.1\lambda_0$; namely, a regular tetrahedron with $\epsilon_r = 50$ and a square pyramid with $\epsilon_r = 40$. The height of the testing domains H is carefully adjusted in order to maximize the accuracy.

  The computed relative errors of our discontinuous implementations are smaller than the errors exhibited by the RWG-implementation in all examples. In light of Fig. 5.21 we detect a decrease in the RCS-error between $\mathcal{O}(h)$ and $\mathcal{O}(h^{1.5})$ with the tangential-

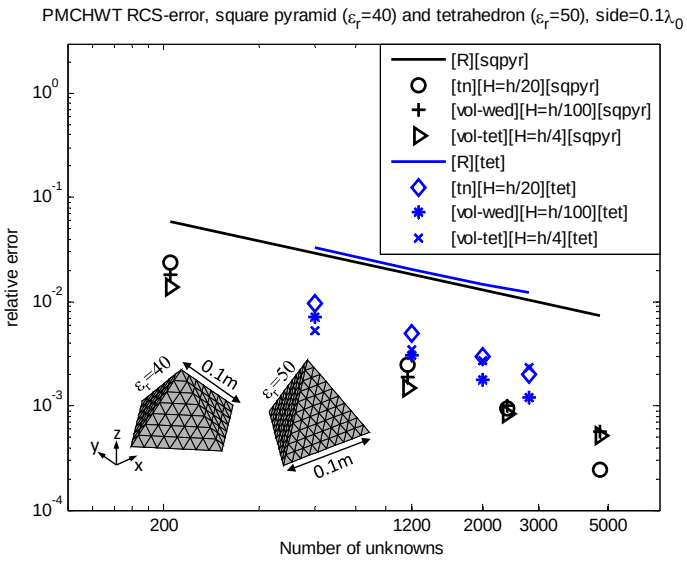

Figure 5.21: RCS relative error (5.17) of several monopolar-RWG PMCHWT implementations versus the number of unknowns for a regular tetrahedron with side 0.1m and square pyramid with side 0.1m (λ_0 =1m), and relative permittivities 40 and 50, respectively, for several values of testing heights H. The reference results are computed with PMCHWT[R] and very fine meshing (around 16300 triangles)

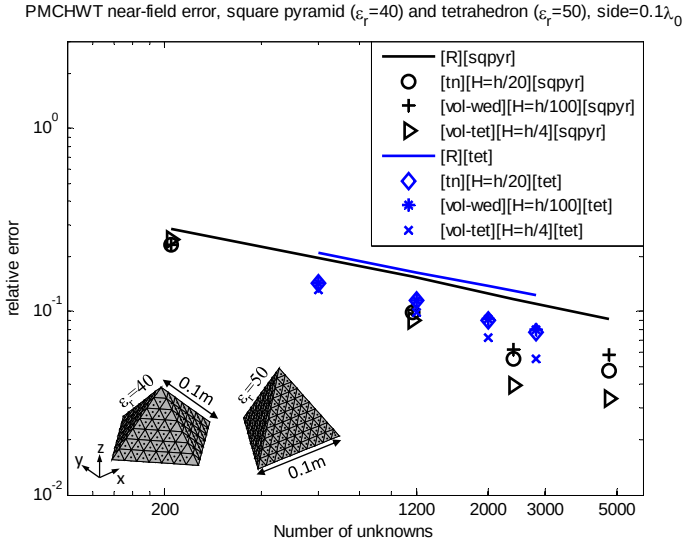

Figure 5.22: Near-field relative error (5.16) of several discontinuous PMCHWT numerical implementations versus the number of unknowns for a regular tetrahedron with side 0.1m and square pyramid with side 0.1m (λ_0 =1m), and relative permittivities 40 and 50, respectively, for several values of testing heights H. The reference results are computed with PMCHWT[R] and very fine meshing (around 16300 triangles)

normal and wedge testings and around $\mathcal{O}(h^{0.7})$ with the tetrahedral testing. The continuous low-order implementation of the PMCHWT formulation exhibits an error reduction around $\mathcal{O}(h^{0.6})$. According to Fig. 5.22, all the implementations exhibit a reduction in the near-field errors around $\mathcal{O}(h^{0.4})$.

Singular field behaviour is expected to occur only near sharp edges and corners of the penetrable targets under analysis. Therefore, it is reasonable to use *hybrid* continuous-discontinuous PMCHWT numerical formulations, where the monopolar-RWG basis functions and corresponding off-boundary testing is defined only on edges forming sharp wedges, and RWG basis and testing functions on (quasi) coplanar pairs of triangles. These hybrid PMCHWT formulations maintain the accuracy of the fully discontinuous PMCHWT implementations, but drastically reduce the number of unknowns. They appear as appropriate choices in the accurate analysis of single sharp-edged penetrable targets with high relative permittivity/permeability contrasts.

5.3.3.2 Nonconformal and defective meshes

- *Nonconformal meshes*

  We show bistatic RCS results and normalized absolute values of surface field quantities of our discontinuous PMCHWT implementations for the scattering analysis of several single objects, discretized with nonconformal meshes. In Figs. 5.23 and 5.24, we show the bistatic RCS and normalized absolute values of currents for two single dielectric targets, respectively, a dielectric sphere, with radius of 0.4m and $\epsilon_r = 20$, and a dielectric cone-cylinder, with radius 0.4m, height of 0.6m and $\epsilon_r = 3$. The nonconformal meshes adopted in Figs. 5.23 and 5.24 arise from the interconnection of independently meshed open triangulations. The testing entities in the volumetric monopolar-RWG PMCHWT-implementations, for the sake of flexibility, are defined nonconformal to the boundary-surface.

  The conventional RWG-discretization cannot manipulate the nonconformal meshes in Figs. 5.23 and 5.24 because some adjacent triangles do not have single matching edges.

  For the case of the dielectric sphere in Fig. 5.23, the RCS results computed with our monopolar-RWG schemes are compared with the Mie series solution [2] while for the case of dielectric cone-cylinder, in Fig. 5.24, we compare our results with the solution obtained using the RWG-implementation of the PMCHWT formulation, a geometrically conformal mesh and the similar number of unknowns.

  As for the choice of the height of volumetric testing elements, H, similarly to the analysis of nonconformally meshed PEC targets, we develop two strategies. If there are slits between independently meshed subdomains (curved objects like cylinders, cones or spheres) and/or the relative permittivity/permeability of the penetrable target is high (a more challenging electromagnetic problem), we choose bigger heights of testing elements (in the range from $H = h/10$ to $H = h$). For the cases of nonconformal meshes without slits and low relative permittivity/permeability values, any choice from the H-ranges shown in Figs. 5.15 and 5.16 works good. In order to reduce the number of unknowns, in the analysis of single penetrable objects meshed with nonconformal meshes, we use a hybrid version of our volumetric nonconforming PMCHWT

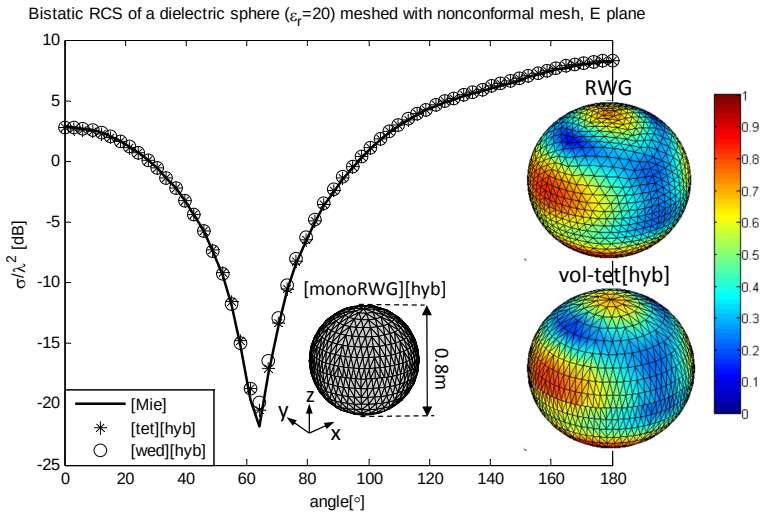

Figure 5.23: Bistatic RCS of a dielectric sphere ($r = 0.4$m, $\epsilon_r = 20$) and the normalized absolute value of the surface electric current under an impinging x-polarized z-propagating plane wave and $\lambda_0 = 1$m. The number of unknowns is 5292 for our hybrid monopolar-RWG PMCHWT-implementations. The Mie series solution is adopted as reference. Volumetric tetrahedral and volumetric-wedge implementations use $H = h/2$

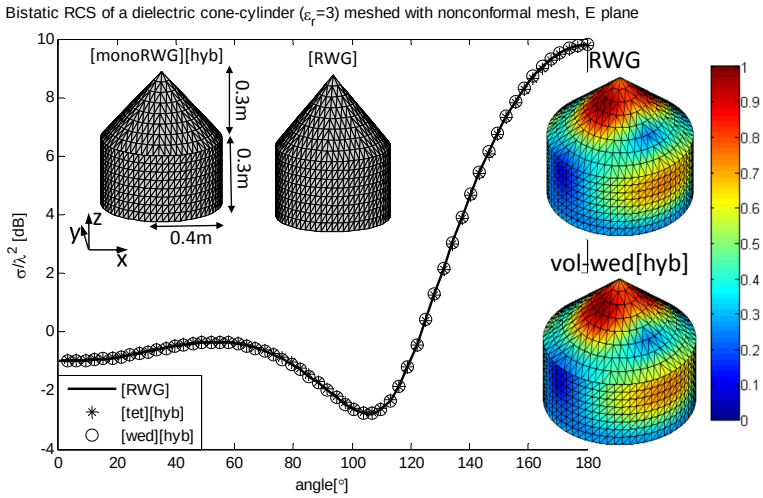

Figure 5.24: Bistatic RCS of a dielectric object composed of cone and cylinder with radius 0.4m and height 0.6m and the normalized absolute value of the surface magnetic current under an impinging x-polarized z-propagating plane wave and $\lambda_0 = 1$m. The number of unknowns is 6010 for our hybrid monopolar-RWG PMCHWT-implementations and 6144 for RWG implementation which is adopted as reference. Volumetric tetrahedral and volumetric-wedge implementations use $H = h/5$

schemes. Analogously to the hybrid version of the nonconforming EFIE for nonconformal meshes, this hybrid version of our nonconforming PMCHWT techniques assumes the monopolar-RWG expansion of the currents and volumetric testing of the fields only on the nonconformal part of the mesh, where adjacent triangles do not share the same edge, and RWG basis and testing elsewhere.

- *Defective meshes*
  A common unambiguous manner to describe a triangular mesh is the connectivity file [3], which comprises a list of the vertices arising in the triangulation and a list of facets, assigning to each facet the three involved vertices as indexed in the vertex list. Whereas the connectivity file alone is enough for the facet-based discontinuous schemes to compute the electromagnetic response, the edge-based (divergence-conforming) schemes require, prior to the scattering analysis, the execution of edge finding algorithms, which may actually become rather time-consuming for electrically large meshes. These algorithms focus exclusively on the search of *interior* edges, shared by pairs of well-connected triangles, and discard *boundary* edges, belonging to a single triangle each. The identification of interior edges allows the proper expansion of the currents through divergence-conforming sets, which require a normally continuous transition across interior edges.

  Defected meshes form a subclass of geometrically nonconformal meshes which may arise from the simple error in the construction of a conformal mesh; e.g. two edges may not be properly connected forming two vertices instead of one, unwanted spurious slits may arise between the edges etc. [90]. The edge search algorithms in these cases normally misclassify interior edges as boundary edges, thereby modelling wrongly the currents and perhaps giving rise to inaccuracies. Flaws in the mesh generation may become unnoticed by the engineer, especially in the analysis of complex non-canonical structures. In practice, the management of defective meshes constrains engineers to spend much time in strenuous tasks such as stitching surfaces together or connecting disjointed vertices.

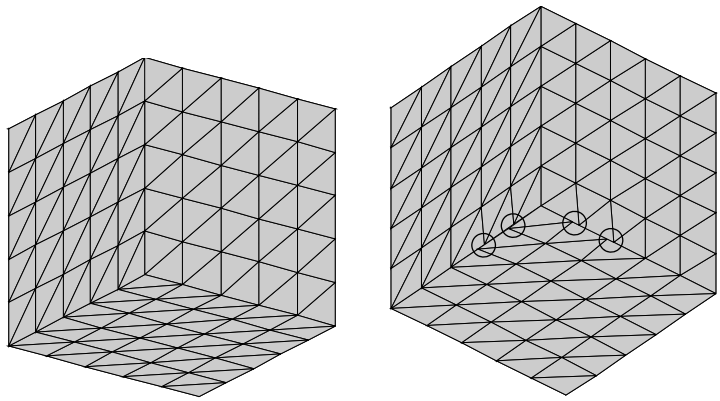

Figure 5.25: Schemes of meshing for the cube with 300 triangles. (a): geometrically conformal mesh, (b): defective mesh (shifting $0.006m$ two vertices on top of sharp wedges)

Our facet-based discontinuous schemes ignore by definition the edges arising from the discretization, whereby they excel as grid-robust schemes, as shown in [91] for smooth conductors.

A slightly defective mesh definition on sharp-edged objects, with just a few unconnected vertices on top of a physical wedge, may be enough for the edge-based schemes to exhibit important RCS-inaccuracies. On contrary, the RCS computed with our volumetric monopolar-RWG PMCHWT schemes for such cases is similar to the RCS computed with the RWG-schemes and well-connected conformal meshes, which is a proof of their robustness.

In Fig. 5.26, we show the computed RCS and normalized absolute value of surface electric current for two dielectric cubes with side 0.3m under an impinging x-polarized z-propagating plane wave and: (a)$\epsilon_r = 2$, (b)$\epsilon_r = 40$. We make use of two meshes, conformal and defective, of 300 triangles. The defective mesh results from shifting 0.006m four vertices of the conformal mesh along the sharp wedges (see Fig. 5.25). Four vertices from the original conformal mesh become then four pairs of unconnected vertices in the defective meshes (see circled vertices on Fig. 5.25(b)). Equivalently, six interior edges of the conformal mesh are ignored by edge search algorithms in the management of defective mesh. In light of Fig. 5.26, the hybrid continuous-discontinuous discretization of the PMCHWT formulation with tetrahedral [tet][hyb] or wedge [wed][hyb] testing, where the monopolar-RWG basis functions and volumetric testing are assigned only on the defective parts of the mesh, exhibit similar accuracy as RWG-PMCHWT with the conformal mesh.

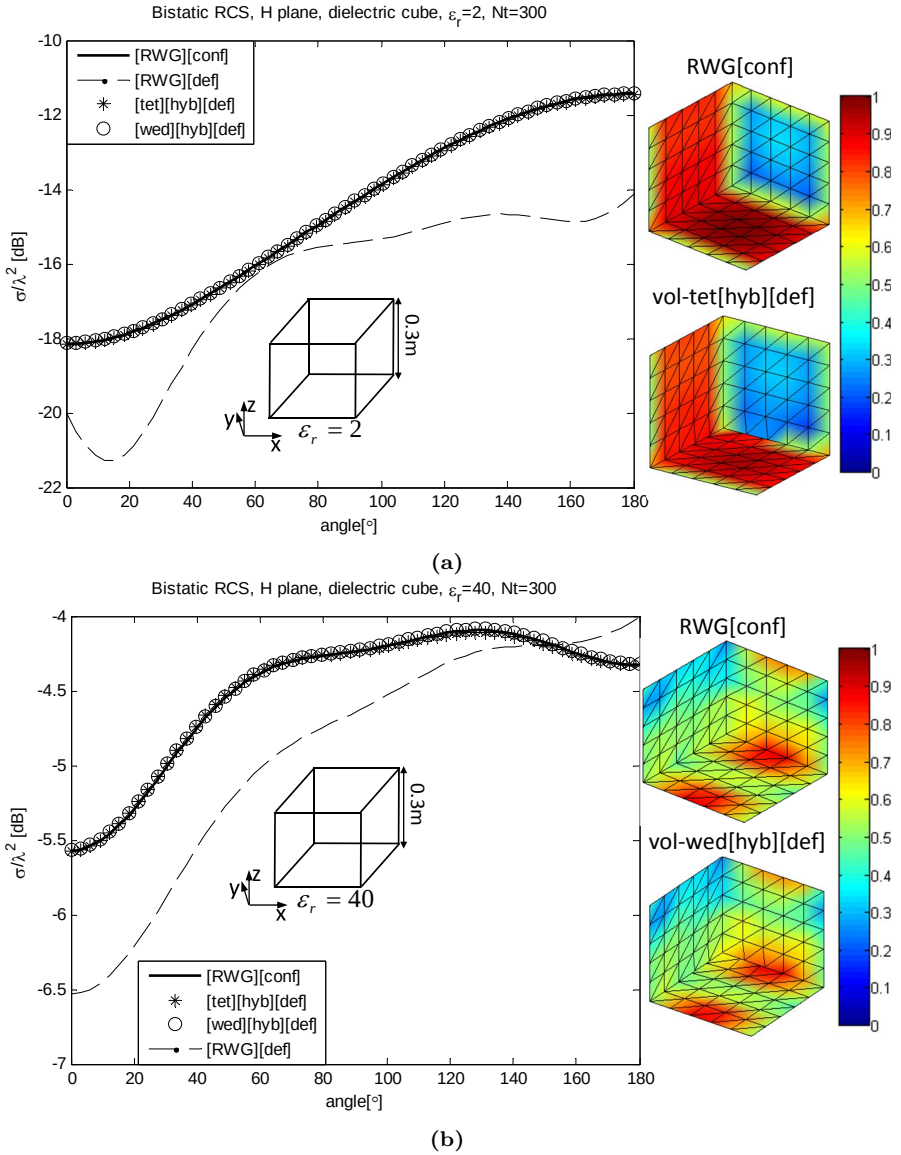

Figure 5.26: Computed RCS and normalized absolute value of surface electric current for a dielectric cube with: (a) $\epsilon_r = 2$ and (b) $\epsilon_r = 40$ for two schemes of meshing (conformal and defective), and 300 triangles. [RWG][conf] and [RWG][def] denote the RCS computed with RWG-PMCHWT on both meshes, conformal and defective. [tet][hyb][def] and [wed][hyb][def] denote the computed RCS with volumetric monopolar-RWG PMCHWT implementations and $H = h/10$ on the defective mesh. The impinging plane wave is x-polarized and z-propagating ($\lambda_0 = 1$m).

5.4 Discontinuous discretization of EFIE-PMCHWT for arbitrarily shaped piecewise homogeneous objects with junctions

Our single-trace discontinuous implementation of the EFIE-PMCHWT for the scattering analysis of arbitrarily shaped piecewise homogeneous objects with junctions is defined in a similar manner as the discontinuous TE/TM-EFIE-PMCHWT discretizations (see section 4.5) except for the fact that both electric and magnetic boundary conditions are tested volumetrically. Here we omit the tangential-normal testing strategy since the composite objects are usually meshed with nonconformal meshes arising from the juxtaposition of independently meshed homogeneous subdomains. Similarly to the PEC problems, we have observed that volumetrically tested implementations deliver better accuracy and stability in the analysis of nonconformal triangulations when compared to tangential-normal schemes. The junction-nodes defined in section 4.5 translate now to junction-edges and the implementation of single-trace continuous EFIE-PMCHWT becomes awkward since Kirchhoff current continuity conditions have to be satisfied around them [46]- [50]. However, this conforming technique has become widespread over the last decades because of the observed good accuracy and the restrained number of unknowns. The use of a moderate number of unknowns was particularly compelling in earlier times, when the computational resources were limited. However, the establishment of the continuity conditions at junctions demands some previous insight into the mesh topology in order to identify edges and junctions, which may actually be rather time-consuming for intricate or fine meshes, and gives rise in general to additional bookkeeping effort in the matrix generation.

The single-surface RWG-discretization of the EFIE–PMCHWT formulation can handle meshes, such as Fig. 5.27(a), where the intersecting regions at junctions are conformal at the junction as long as the appropriate treatment at junctions is applied [46]- [50]. However, this approach cannot address the analysis of nonconformal meshes meeting at junctions, arising very often from the juxtaposition of independently meshed targets, such as for example Fig. 5.27(c). Alternative conforming implementations of the EFIE–PMCHWT formulation, double-surface or multi-trace, are obtained by representing the composite object as a union of disjoint homogeneous regions immersed in the host medium with separation distances (δ) tending to zero (see Fig. 5.27(b) and Fig. 5.27(d)). The original interfaces between two regions are now considered as two contact surfaces and thus junction-edges, which result from the intersection of more than two regions, do not exist. The programming burden of these approaches is alleviated when compared with the single-surface approach because the treatment of junction-edges is avoided. However, the number of unknowns rises because of the definition of redundant unknowns over touching interfaces. Although nowadays, in a context of sufficient memory resources, this requirement may seem of minor importance, in earlier times could become prohibitive. Moreover, the two-surface analysis [51] requires the computation of the residues of the integrals in (5.25), in addition to the Cauchy principal values, so that the tangential field continuity conditions are satisfied between touching regions. This becomes especially tricky if the touching meshes are nonmatching, as in Fig. 5.27(d).

Since the monopolar-RWG basis functions and the volumetric testing schemes are facet-based, these approaches by construction ignore junctions. This is very advantageous

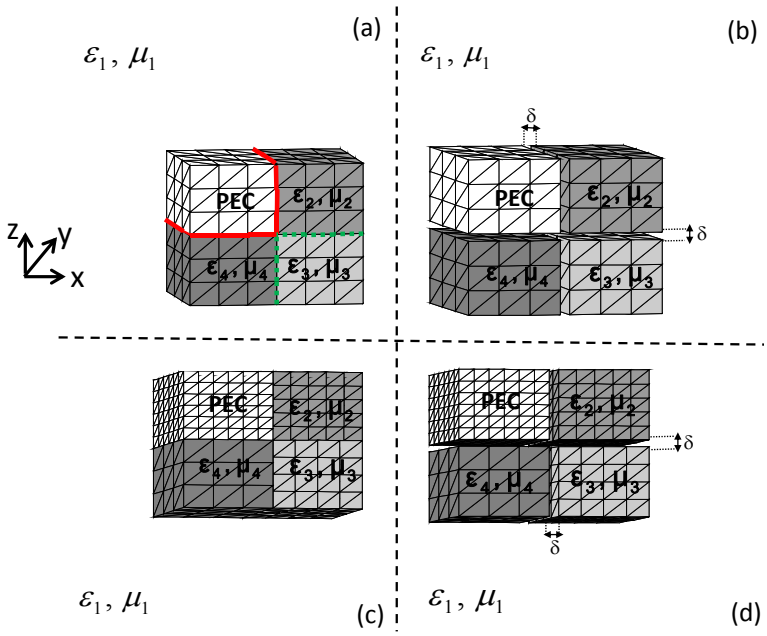

Figure 5.27: Analysis of arbitrarily shaped composite objects. (a) Single-surface interfaces and geometrically conformal segmentations. (b) Interfaces with two contact surfaces and conformal segmentations ($\delta \to 0$). (c) Single-surface interfaces and nonconformal segmentations. (d) Two-surface interfaces and nonconformal segmentations ($\delta \to 0$)

because, unlike junction-edges, which arise from the intersection of several regions, all the facets arising from the discretization of an arbitrary composite object separate two regions only. Therefore, these schemes invoke the same number of homogeneous problems in the analysis of composite objects as in the analysis of single objects. Namely, two if the bordering regions are penetrable and one if one region is PEC. In general, our approach exhibits great flexibility when handling composite objects discretized with conformal meshes, as in Fig. 5.27(a), because the special treatment of junctions of the conventional schemes is avoided. Moreover, the single-surface discontinuous analysis of the nonconformal mesh in Fig. 5.27(c), where the single-surface RWG implementation fails because the two overlapping meshes do not match, is carried out through the expansion (or testing) of the electric or magnetic currents (or fields) over a different overlapping triangulation each.

The generation of the impedance matrix elements in our discontinuous schemes becomes more elaborate than with the conventional RWG-schemes because line or volumetric integrals are computed. However, in our experience, this computational load is counterbalanced with the easier management of facet-to-facet interactions and one or two invoked homogeneous problems for each interaction. Furthermore, it is well understood that these facet-based schemes do not demand a search for edges or junctions as is required for the edge-based schemes. Note that the edge-search procedures become difficult and time-consuming for intricate and dense meshes and are bound to be fruitless for nonconformal or defective meshes.

5.4.1 Numerical results

Here we show the suitability of our single-surface monopolar-RWG implementations in the analysis of various composite objects discretized with nonconformal meshes, where the single-surface RWG-discretization cannot be adopted. The computed results with volumetrically tested discontinuous schemes, wedge, EFIE-PMCHWT[vol-wed] and tetrahedra, EFIE-PMCHWT[vol-tet], are compared with the two-surface RWG-discretization of the EFIE–PMCHWT formulation. The composite targets are impinged by an x-polarized $+z$-propagating plane wave and the free-space wavelength (λ_0) is set to 1m.

We show far-field results of our single-surface monopolar-RWG EFIE–PMCHWT implementations for the scattering analysis of several composite objects with junctions, discretized with nonconformal meshes. In Figs. 5.28(a) and 5.28(b), we show the computed bistatic RCS for two composite objects with dielectric or PEC regions. The nonconformal meshes employed in the composite objects of Figs. 5.28(a) and 5.28(b) arise from overlapping two nonmatching triangulations (see Fig. 5.27(c)). The volumetric testing elements are defined nonconformal to the boundary-surface.

The standard single-surface RWG-implementation of the EFIE–PMCHWT formulation cannot handle the nonconformal meshes in Figs. 5.28(a) and 5.28(b) because the two triangulations sharing an interface do not match. For this reason, the RCS results computed with our single-surface monopolar-RWG implementations in Figs. 5.28(a) and 5.28(b) are compared with the two-surface RWG-implementation ($\delta \to 0$) and the similar number of unknowns.

Note that here we do not include the basic test example of a composite object discretized with a conformal mesh (see Fig. 5.27(a)). Indeed, the circumvention of junctions in the discontinuous analysis without sacrificing accuracy is already implicit in the observed results for the analysis of composite objects discretized with nonconformal meshes in Figs. 5.28(a) and 5.28(b), which are actually more challenging. The H-choice strategy for the single surface discontinuous analysis of composite objects follows the plan developed for the analysis of single penetrable targets developed in Section 5.3.3.2. Here we use full monopolar-RWG volumetric EFIE-PMCHWT implementations in order to completely ignore the search for junction-edges in the preprocessing stage, which substantially increases the flexibility of the method.

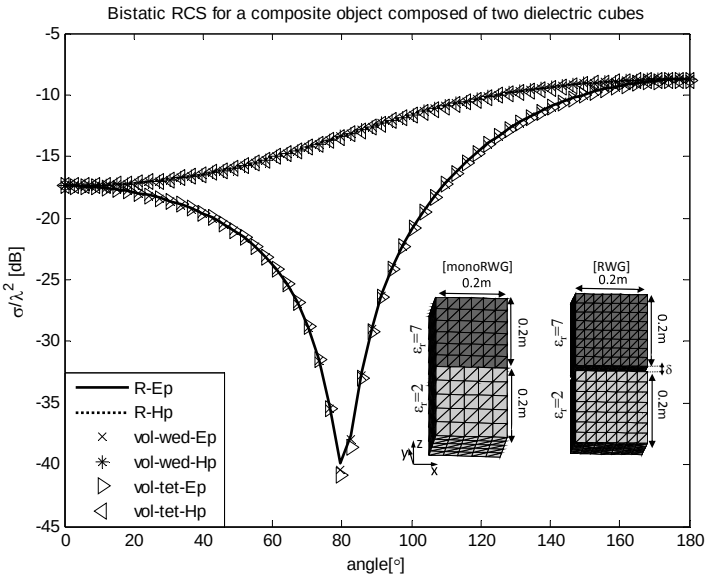

(a)

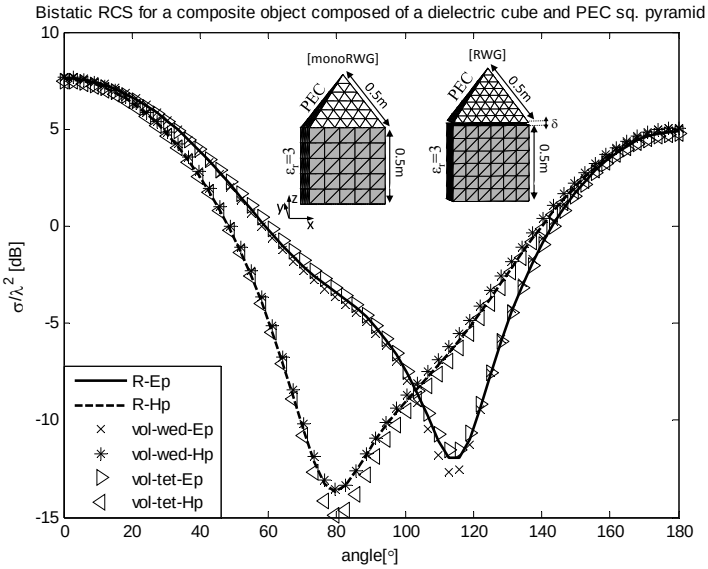

(b)

Figure 5.28: Computed RCS for two composite objects: (a) composite object comprised of two dielectric cubes ($\epsilon_r = 2$ and $\epsilon_r = 7$) with sides of 0.2m and (b) composite object comprised of a dielectric cube ($\epsilon_r = 3$, side = 0.5m) and a PEC square pyramid (side = 0.5m). The number of unknowns are similar in our discontinuous single-surface approach and continuous double-surface implementation ($\delta \to 0$), which is adopted as reference. The implementation with wedge testing uses $H = h/1e4$ while the implementation with tetrahedral testing uses $H = h/5$

5.5 Discontinuous discretization of the PMCHWT formulation for domain decomposition strategy

Divergence-conforming techniques are able to operate only on a conformal mesh, which is a very stringent condition. Generating such a mesh for a realistic multi-scale structure composed of parts with disparate electrical sizes is a daunting task. Moreover, the successful construction of such meshes often leads to ill-conditioned impedance matrices, which slows down the iterative search of the solution with Krylov subspace methods. Recently, integral-equation domain decomposition method (DDM) has been introduced for the scattering analysis of large and multi-scale perfectly conducting (PEC) targets [30]. The convergence of DDM is strongly dependent on the transmission conditions established between adjacent sub-domains. Usually, each independently meshed sub-domain arising from the tearing of the original problem is enclosed with an artificial surface. Then, auxiliary unknowns need to be defined on it in order to enforce the continuity of the tangential fields. In this section, we introduce a discontinuous PMCHWT domain decomposition method for the efficient analysis of multi-scale penetrable targets which does not require the definition of artificial enclosing surfaces and auxiliary unknowns in the process of tearing the original domain. The ability to deal with open surfaces represents a clear advantage since no additional mesh manipulation is needed in order to enclose the sub-domains and, subsequently, no auxiliary unknowns are required. This can significantly reduce the memory requirements. The transition of the electric and magnetic currents between adjacent sub-domains is enforced with the monopolar- RWG basis functions along with volumetric testing procedure, introduced in Section 5.3.1, over the tearing contour. The facet-based monopolar- RWG basis functions allow for the touching triangulations between sub-domains to be geometrically nonconformal, which enables the flexibility and modularity in the mesh generation associated to domain decomposition methods. To further accelerate the iterative search of the solution, for large problems, a block-diagonal preconditioner is implemented, with the blocks accounting for the self sub-domain interactions.

We decompose the original penetrable target (Ω) into a number of non-overlapping sub-domains (Ω_k), so that $\Omega = \bigcup_{k=1}^{M} \Omega_k$ holds. Each sub-domain is now an open surface bounded with closed contour (Γ_k), and M is the number of sub-domains (see Fig. 5.29).

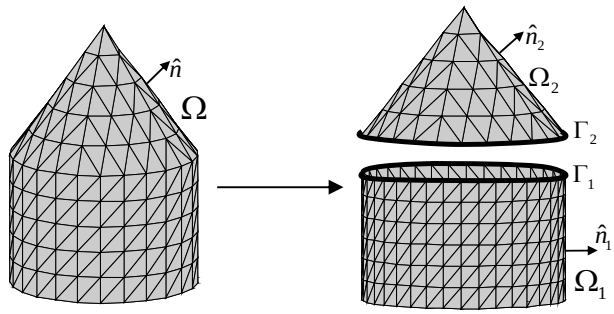

Figure 5.29: Partition of the original geometry into two sub-domains

We approximate the unknown electric and magnetic currents with RWG basis functions

$\{\boldsymbol{f}^{k,n}\}$ over N_{Ω_k} interior edges arising in the tessellation of each open surface (Ω_k), corresponding to every particular sub-domain, as follows

$$\boldsymbol{J}_\Omega \simeq \sum_{k=1}^{M} \sum_{n=1}^{N_{\Omega_k}} J_\Omega^{k,n} \boldsymbol{f}^{k,n} \tag{5.40}$$

$$\boldsymbol{M}_\Omega \simeq \sum_{k=1}^{M} \sum_{n=1}^{N_{\Omega_k}} M_\Omega^{k,n} \boldsymbol{f}^{k,n} \tag{5.41}$$

where $\{J_\Omega^{k,n}\}$ and $\{M_\Omega^{k,n}\}$ represent the sets of unknown RWG-coefficients in the expansion of the currents over the interior edges forming the sub-domain surfaces.
Furthermore, the transition of the tangential fields between the sub-domains is enforced by expanding the associated electric and magnetic currents with the monopolar-RWG basis functions $\{\boldsymbol{m}^{k,p}\}$ over N_{Γ_k} boundary edges arising in the discretization of the closed contours (Γ_k) bounding the surfaces (Ω_k) as

$$\boldsymbol{J}_\Gamma \simeq \sum_{k=1}^{M} \sum_{p=1}^{N_{\Gamma_k}} J_\Gamma^{k,p} \boldsymbol{m}^{k,p} \tag{5.42}$$

$$\boldsymbol{M}_\Gamma \simeq \sum_{k=1}^{M} \sum_{p=1}^{N_{\Gamma_k}} M_\Gamma^{k,p} \boldsymbol{m}^{k,p} \tag{5.43}$$

and $\{J_\Gamma^{k,p}\}$ and $\{M_\Gamma^{k,p}\}$ denote the sets of unknown monopolar-RWG coefficients associated with the expansion of the electric and magnetic currents over the boundary edges. The total expanded currents, $\boldsymbol{J}$ and $\boldsymbol{M}$, are the sum of their RWG and monopolar-RWG components; $\boldsymbol{J} = \boldsymbol{J}_\Omega + \boldsymbol{J}_\Gamma$, $\boldsymbol{M} = \boldsymbol{M}_\Omega + \boldsymbol{M}_\Gamma$.
The monopolar-RWG Galerkin testing of the discretized electric field integral operator $\boldsymbol{\mathcal{T}}^{k,p}$ arising in the discretization of the PMCHWT equation gives rise to double contour integrals linked to the gradient of the scalar potentials (see Section 5.3). These integrals become unbounded when the field point approaches the source point. To circumvent this problem we test the fields with tetrahedral or wedge elements attached to the facets forming the sub-domain boundary contours and lying inside the region where, in accordance with the equivalence theorem, fields must be null (for the elaborate definition of these testing schemes see Section 5.3.1). Note that, although the surfaces arising in tearing the original domain are individually open, they are part of a closed domain, whereby the surface equivalence theorem holds.

5.5.1 Numerical results

We study the electromagnetic scattering from an electrically small sharp-edged object consisting of a cube and a regular square pyramid with side 0.2m and high relative dielectric contrast ($\epsilon_r = 40$). Note that this is a challenging problem since singular fields are induced around sharp wedges and corners due to the high relative permittivity of the target. For the sake of simplicity, we partition the original geometry into two sub-domains and mesh them separately with different mesh sizes. We compare the far-field results obtained with our discontinuous PMCHWT domain decomposition method, with wedge

[DDM][wed] or tetrahedral [DDM][tet] testing (988 facets) to the result computed with the standard RWG-PMCHWT implementation, [RWG], and a conformal mesh (784 facets). Furthermore, we precondition the linear system with block diagonal preconditioner, as

$$\begin{bmatrix} \mathbf{A}_1 & 0 \\ 0 & \mathbf{A}_2 \end{bmatrix}^{-1} \begin{bmatrix} \mathbf{A}_1 & \mathbf{A}_{12} \\ \mathbf{A}_{21} & \mathbf{A}_2 \end{bmatrix} \begin{bmatrix} \mathbf{x}_1 \\ \mathbf{x}_2 \end{bmatrix} = \begin{bmatrix} \mathbf{A}_1 & 0 \\ 0 & \mathbf{A}_2 \end{bmatrix}^{-1} \begin{bmatrix} \mathbf{b}_1 \\ \mathbf{b}_2 \end{bmatrix} \tag{5.44}$$

where

$$\mathbf{P}^{-1} = \begin{bmatrix} \mathbf{A}_1 & 0 \\ 0 & \mathbf{A}_2 \end{bmatrix}^{-1} \tag{5.45}$$

is the proposed preconditioner and the blocks $\mathbf{A}_1$ and $\mathbf{A}_2$ account for the self sub-domain interactions. Note that this preconditioning scheme is highly parallelizable in nature because operations involving different sub-domains can be performed independently.
The target is impinged by an x-polarized plane wave propagating in the $+z$ direction, and the free-space wavelength λ_0 is set to 1m. In view of Fig. 5.30, an excellent agreement between far-field results as well as much faster solution convergence of the preconditioned linear system obtained with GMRES solver are observed (residual required to the iterative solver is set to 0.001).

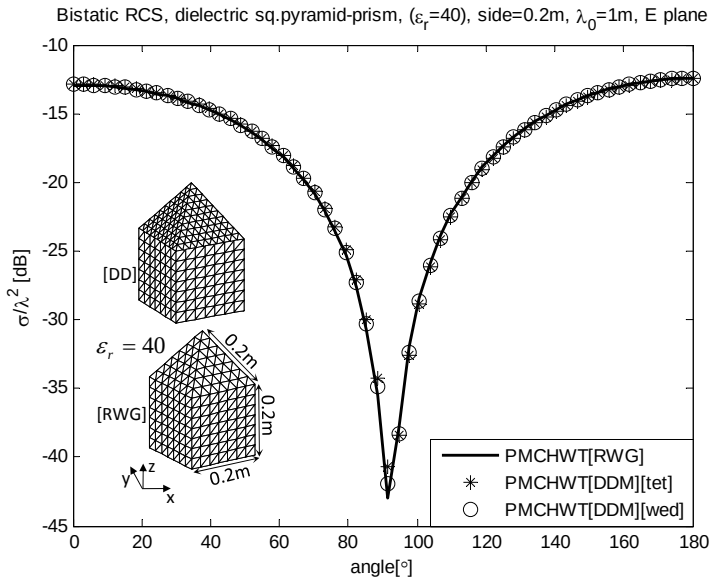

(a)

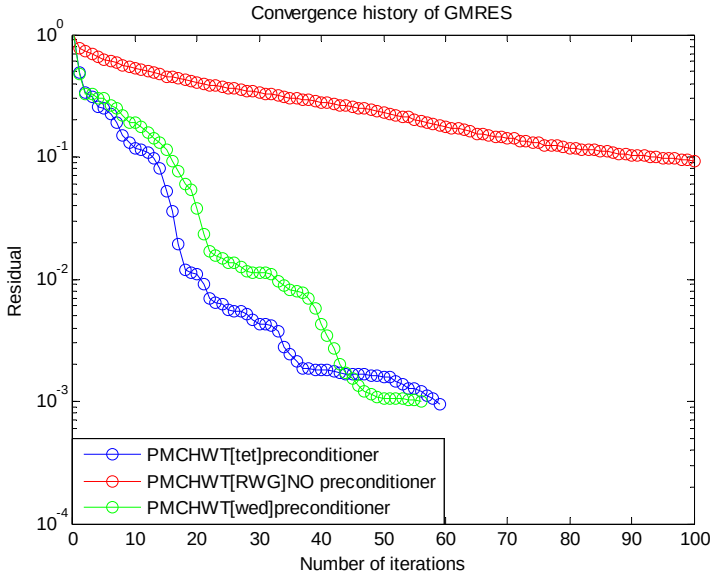

(b)

Figure 5.30: (a): computed bistatic RCS for a dielectric target consisting of a cube and regular square pyramid, $\epsilon_r = 40$. (b): convergence history of the GMRES solver. The number of facets is 988 for our discontinuous volumetric PMCHWT-implementations and 784 for RWG implementation which is adopted as reference. Volumetric tetrahedral and volumetric-wedge implementations use $H = h/10$

Chapter 6

Hierarchical Rearrangement of the Monopolar-RWG Space Applied to the Scattering Analysis of Sharp-Edged Plasmonic Nanoparticles

6.1 Introduction

When metallic nanoscale particles are excited with electromagnetic fields at optical frequencies, localized free charge oscillations, known as localized surface plasmons, are induced on metal interfaces [92]. Plasmonic effects at the nanoscale are especially interesting because they produce strong near-field enhancement giving rise to new interesting applications in photovoltaic systems, waveguiding, optical metamaterials, nanoantennas, photodetectors and nonlinear optics [93]- [101]. Therefore, efficient and accurate electromagnetic modelling of these phenomena is called for.

Among the plethora of numerical methods available for the analysis of plasmonic nanostructures, such as the discrete dipole approximation (DDA) [102]- [104] and the finite difference time domain (FDTD) [105] method, the surface integral equation approach, sometimes referred as the boundary element method, is particularly attractive for open-region (scattering) problems and for problems where the important physical phenomena take place close to the boundaries. At lower frequencies (radio or microwave frequencies) metals can be well approximated as perfect electric conductors. In optical regime, however, the penetration of the fields into the particle and the plasmonic effects have to be accurately taken into account.

For penetrable objects, SIE can be expressed in many alternative forms. One of the most popular formulation is the PMCHWT integral equation formulation [19]- [21], recently applied widely also in the analysis of nanoplasmonic systems [106]- [108]. In the standard Galerkin method of moments discretization of the PMCHWT equations [9] the unknown equivalent electric and magnetic surface current densities are expanded with the low order divergence-conforming RWG basis functions [34]. Then, the discretized equations are cast into a matrix form by means of testing the tangential field components with

the same set of functions. As elaborated in Chapter 3, this discretization of PMCHWT equations is *conforming* with respect to fractional order vector Sobolev space mappings, hence providing converging solutions as the number of degrees of freedom is increased.
However, the RWG-PMCHWT scheme is no panacea. Recent advances in nanofabrication have allowed the manipulation of the shape of nanoparticles up to the subnanometer scale [109]- [112] introducing atomically sharp tips around which electromagnetic energy can be successfully confined (so called "hot-spots") [113]. Therefore, accurate modelling of the singular field quantities induced around abrupt geometrical singularities is of great importance [114]- [117]. Unfortunately, standard divergence-conforming bases, including the higher order versions, have difficulties with modelling this phenomenon efficiently [41], [82]. In turn, slow convergence in the scattering and absorption spectra in the resonance domain has been reported with respect to the number of degrees of freedom [106], [117]. It is clear that a better representation of the singular field quantities is needed. Singular higher order divergence-conforming bases of the additive kind proposed by Graglia and Lombardi [41], [82] are constructed for this purpose. In addition to the regular div-conforming subset, they incorporate *Meixner* subset in order to capture singular behaviour of the currents and charges near sharp corners better. However, these bases have been applied to PEC objects only. Furthermore, the singular coefficients of the singular terms have to be known *a priori*, and they directly depend on the angle and the material properties of the associated wedge.
In Chapter 5, Section 5.3.1, the discretization of the PMCHWT integral equation formulation with facet-based monopolar-RWG basis functions, discontinuous across edges, in conjunction with volumetric-tetrahedral testing has been introduced. This discretization scheme is *nonconforming* to the corresponding function spaces. Despite of that, as it has been shown by several examples in Chapter 5, Section 5.3.3, the monopolar-RWG discretization of PMCHWT equations produces more accurate results in the near-field and far-field than the standard RWG approach for the cases of dielectric or ferromagnetic objects that exhibit singular or near-singular field distribution near sharp edges. Unfortunately, the improved performance of the monopolar-RWG PMCHWT approach was observed for a restricted range of heights of the tetrahedral testing elements (see for example Fig. 5.15). In this chapter we propose a hierarchical rearrangement of the monopolar-RWG space into *even* monopolar-RWG (non-normalized RWG) and *odd* monopolar-RWG subspaces. Although this discretization scheme is edge-based, wider tetrahedral testing element height ranges with improved accuracy have been noticed when compared to the monopolar-RWG PMCHWT technique [118]. Furthermore, this hierarchical discretization of PMCHWT is beneficial since it can be made free from the low-frequency breakdown after an appropriate solenoidal-nonsolenoidal rearrangement of the space of currents. The performance of this even-odd (EO) monopolar-RWG discretized PMCHWT formulation has been tested on subwavelength canonical sharp-edged ferromagnetic targets out of the resonance domain [118]. The improvement in the far-field accuracy, when compared to the standard RWG approach with the same number of unknowns, was attributed to the better singular field modelling near sharp edges.
In this chapter, we focus on the scattering analysis of subwavelength sharp-edged plasmonic nanoparticles in the resonance domain. We show with several numerical examples, including hexahedral, octahedral or tetrahedral silver inclusions, that better convergence in the scattering and absorption spectra with the proposed discontinuous EO-monopolar-RWG PMCHWT implementation is achieved compared to the standard RWG-PMCHWT

technique. Also, we show improved near-field results for the case of a hexahedral silver inclusion computed with our discontinuous implementation and compared to the RWG discretization. The convergence of the resonances of sharp-vertex particles is a particularly interesting example of plasmonic enhancement with a long history [119] used as a testbed for current physics and application-oriented plasmonic research [120]- [127]. Moreover, the presented methodology could be extended for cases, such as sub-nano particles and gaps, where enhanced quantum phenomena affect the observed spectrum requiring quantum-corrected classical approaches [128].
The work presented in this chapter is submitted for publication to *Physical Review B*.

6.2 Mathematical formulation

6.2.1 Surface integral equation formulation of the problem

Consider an arbitrarily shaped plasmonic nanoparticle with the orientable surface (Γ) and electromagnetic parameters (ϵ_2, μ_2) embedded in a surrounding medium (usually free-space) with parameters (ϵ_1, μ_1). Here, we assume that the particles are made of silver and modelled according to the Drude model [129]

$$\epsilon_2(\lambda) = \epsilon_0 \epsilon_{Ag}(\lambda) = \epsilon_0 \left(\epsilon_\infty - \frac{(\lambda/\lambda_p)^2}{1 - j\lambda/\lambda_d} \right) \tag{6.1}$$

where $\epsilon_\infty = 5.5$, $\lambda_p = 130$nm, $\lambda_d = 30\mu$m, and ϵ_0 is the electric permittivity of vacuum. The time-harmonic incident electromagnetic field ($\boldsymbol{E}^{inc}$, $\boldsymbol{H}^{inc}$) with angular frequency ω is impinging upon the particle and time-dependency $e^{j\omega t}$ for the fields and currents is assumed and suppressed. By invoking surface equivalence theorem, the total fields in region Ω_i, outside (i=1) or inside (i=2) the particle, ($\boldsymbol{E}_i$, $\boldsymbol{H}_i$), can be represented as the sum of the incident fields generated in region Ω_1 and the scattered fields ($\boldsymbol{E}_i^s$, $\boldsymbol{H}_i^s$) which in turn are generated by equivalent electric and magnetic surface currents $\boldsymbol{J}_i = \hat{\boldsymbol{n}}_i \times \boldsymbol{H}_i$ and $\boldsymbol{M}_i = -\hat{\boldsymbol{n}}_i \times \boldsymbol{E}_i$ residing on the boundary-surface (Γ) inside region Ω_i (see Fig. 2.1). Here $\hat{\boldsymbol{n}}_i$ is the unit normal vector of Γ pointing into region Ω_i. By exploiting appropriate tangential boundary conditions and the integral representations of the fields, PMCHWT integral equation formulation can be derived (for the derivation details see Chapter 2, Section 2.6).
To summarize, we note that the original problem of finding the electromagnetic fields $\boldsymbol{E}_i$ and $\boldsymbol{H}_i$ everywhere outside and inside the particle is reformulated as SIE for the equivalent surface current densities. Once these currents are found they can be used to evaluate the scattered electromagnetic fields everywhere in space. These fields, in turn, can be used to determine, e.g., the scattering and absorption efficiency of the particle.

6.2.2 Discretization strategy

In a usual MoM strategy, the surface of the target is partitioned into N_t triangular elements and the unknown currents are expanded with the set of known subsectional basis functions with the local support on the mesh. In this chapter we approximate the currents with two subsets resulting from the hierarchical decomposition of the space spanned by triangle-based monopolar-RWG set ($\boldsymbol{m}_n$), namely even monopolar-RWG subset ($\boldsymbol{m}_n^e$) and

odd monopolar-RWG subset ($\boldsymbol{m}_n^o$) [54]. Even and odd monopolar-RWG basis functions are edge-based and defined on two triangles ($S_n^1 \cup S_n^2$) sharing the nth edge as follows

$$\boldsymbol{m}_n^e(\boldsymbol{r}') = \begin{cases} \frac{1}{2A_n^1}(\boldsymbol{r}' - \boldsymbol{r}_n^1), & \boldsymbol{r}' \in S_n^1 \\ -\frac{1}{2A_n^2}(\boldsymbol{r}' - \boldsymbol{r}_n^2), & \boldsymbol{r}' \in S_n^2 \end{cases} \tag{6.2}$$

$$\boldsymbol{m}_n^o(\boldsymbol{r}') = \begin{cases} \frac{1}{2A_n^1}(\boldsymbol{r}' - \boldsymbol{r}_n^1), & \boldsymbol{r}' \in S_n^1 \\ \frac{1}{2A_n^2}(\boldsymbol{r}' - \boldsymbol{r}_n^2), & \boldsymbol{r}' \in S_n^2 \end{cases}, \quad 1 \leqslant n \leqslant N_e \tag{6.3}$$

where A_n^1 and A_n^2 denote the areas of the corresponding edge-adjacent triangles, S_n^1 and S_n^2, respectively. The position vectors of the free vertices opposite to the nth edge are designated by $\boldsymbol{r}_n^1$ and $\boldsymbol{r}_n^2$, and N_e is the number of edges in the mesh of the surface. According to (6.2), even monopolar-RWG subset can be interpreted as a non-normalized RWG set because it maintains the continuity of the normal component of the current across the edges. On the other hand, in light of equation (6.3), the odd monopolar-RWG subset enforces the normal component of the current on both sides of the common edge to have the same absolute value but opposite sign.

We approximate the unknown equivalent electric and magnetic currents, $\boldsymbol{J}_i$ and $\boldsymbol{M}_i$, over the two sides of the boundary of a plasmonic target (i=1,2) with the even and odd monopolar-RWG subsets as follows [118]

$$\boldsymbol{J}_i(\boldsymbol{r}') \simeq \sum_{n=1}^{2N_e} J_n^i \boldsymbol{m}_n = \sum_{n=1}^{N_e} a_n^{i,e} \boldsymbol{m}_n^e + \sum_{n=1}^{N_e} a_n^{i,o} \boldsymbol{m}_n^o \tag{6.4}$$

$$\boldsymbol{M}_i(\boldsymbol{r}') \simeq \sum_{n=1}^{2N_e} M_n^i \boldsymbol{m}_n = \sum_{n=1}^{N_e} b_n^{i,e} \boldsymbol{m}_n^e + \sum_{n=1}^{N_e} b_n^{i,o} \boldsymbol{m}_n^o \tag{6.5}$$

where the sequences $\{J_n^i\} = \{a_n^{i,e}, a_n^{i,o}\}$ and $\{M_n^i\} = \{b_n^{i,e}, b_n^{i,o}\}$ represent the sets of unknown coefficients in the expansion of the currents. In view of expressions (6.4) and (6.5), our discontinuous nonconforming implementation defines two basis functions for each edge originating from the discretization, thus leading to twice the number of degrees of freedom compared to the standard RWG expansion, which defines one basis function per edge. The approximated scattered electric and magnetic fields generated by the even and odd monopolar-RWG subsets yield

$$\tilde{\boldsymbol{E}}_i^{s,e/o} = \sum_{n=1}^{N_e} \eta_i \boldsymbol{\mathcal{T}}_n^{i,e/o} a_n^{i,e/o} - \sum_{n=1}^{N_e} \boldsymbol{\mathcal{K}}_n^{i,e/o} b_n^{i,e/o} \tag{6.6}$$

$$\tilde{\boldsymbol{H}}_i^{s,e/o} = \sum_{n=1}^{N_e} \boldsymbol{\mathcal{K}}_n^{i,e/o} a_n^{i,e/o} + \sum_{n=1}^{N_e} \frac{1}{\eta_i} \boldsymbol{\mathcal{T}}_n^{i,e/o} b_n^{i,e/o} \tag{6.7}$$

with associated integral operators defined as

$$\boldsymbol{\mathcal{K}}_n^{i,e/o} = \nabla \times \iint\limits_{S_n^1 \cup S_n^2} G_i(\boldsymbol{r}, \boldsymbol{r}') \boldsymbol{m}_n^{e/o}(\boldsymbol{r}') dS' \tag{6.8}$$

$$\boldsymbol{\mathcal{T}}_n^{i,e/o} = \frac{1}{jk_i}\Bigg(\nabla\nabla\cdot\iint\limits_{S_n^1\cup S_n^2} G_i(\boldsymbol{r},\boldsymbol{r}')\boldsymbol{m}_n^{e/o}(\boldsymbol{r}')dS' + k_i^2\iint\limits_{S_n^1\cup S_n^2} G_i(\boldsymbol{r},\boldsymbol{r}')\boldsymbol{m}_n^{e/o}(\boldsymbol{r}')dS'\Bigg) \tag{6.9}$$

The hierarchical discontinuous PMCHWT formulation imposes the tangential electric and magnetic field boundary conditions over the meshed boundary of the target $\tilde{S} = \bigcup\limits_{t=1}^{N_t} S_t$ as follows

$$\sum_{n=1}^{N_e}\gamma_t(\eta_1\boldsymbol{\mathcal{T}}_n^1+\eta_2\boldsymbol{\mathcal{T}}_n^2)_{\tilde{S}}^{e/o}\,a_n^{e/o} - \sum_{n=1}^{N_e}\gamma_t(\boldsymbol{\mathcal{K}}_n^1+\boldsymbol{\mathcal{K}}_n^2)_{\tilde{S}}^{e/o}\,b_n^{e/o} \simeq -\gamma_t\boldsymbol{E}_{\tilde{S}}^{inc} \tag{6.10}$$

$$\sum_{n=1}^{N_e}\gamma_t(\boldsymbol{\mathcal{K}}_n^1+\boldsymbol{\mathcal{K}}_n^2)_{\tilde{S}}^{e/o}\,a_n^{e/o} + \sum_{n=1}^{N_e}\gamma_t\left(\frac{1}{\eta_1}\boldsymbol{\mathcal{T}}_n^1+\frac{1}{\eta_2}\boldsymbol{\mathcal{T}}_n^2\right)_{\tilde{S}}^{e/o}\,b_n^{e/o} \simeq -\gamma_t\boldsymbol{H}_{\tilde{S}}^{inc} \tag{6.11}$$

where $a_n^{e/o} = a_n^{1,e/o} = -a_n^{2,e/o}$ and $b_n^{e/o} = b_n^{1,e/o} = -b_n^{2,e/o}$ is assumed such that the continuity of the surface currents is satisfied. We cast the discretized equations (6.10) and (6.11) into matrix form by means of testing the tangential fields with appropriate set of testing functions. The standard Galerkin MoM procedure, which adopts the same set for testing the fields and for the expansion of the unknown currents, leads to the following statements

$$\iint\limits_{S_m^1\cup S_m^2}(\tilde{\boldsymbol{E}}_1^{s,e/o}-\tilde{\boldsymbol{E}}_2^{s,e/o})\cdot\boldsymbol{m}_m^{e/o}dS = -\iint\limits_{S_m^1\cup S_m^2}\boldsymbol{E}^{inc}\cdot\boldsymbol{m}_m^{e/o}dS \tag{6.12}$$

$$\iint\limits_{S_m^1\cup S_m^2}(\tilde{\boldsymbol{H}}_1^{s,e/o}-\tilde{\boldsymbol{H}}_2^{s,e/o})\cdot\boldsymbol{m}_m^{e/o}dS = -\iint\limits_{S_m^1\cup S_m^2}\boldsymbol{H}^{inc}\cdot\boldsymbol{m}_m^{e/o}dS, \qquad 1\leqslant m\leqslant N_e \tag{6.13}$$

Since the odd monopolar-RWG functions are not divergence-conforming, moving the gradients to the basis and testing functions in the testing of $\boldsymbol{\mathcal{T}}_n^{i,e/o}$ operator leads to double contour strongly singular integrals that are not integrable in Cauchy principal value sense. In fact, these integrals become unbounded for self or edge-adjacent interactions. In this work we circumvent this problem by the introduction of non-Galerkin testing scheme defined over a pair of facet-adjacent tetrahedral elements attached to the corresponding edge-adjacent triangles arising in the tessellation of the boundary. The testing elements are confined inside the region where, in accordance with the surface equivalence theorem, the fields must be zero (see Fig. 6.1) [118]. These odd monopolar volumetric testing functions [118] $\{\boldsymbol{M}_m^{i,o}\}$ are designed to best couple with odd monopolar-RWG basis functions. They are defined over two facet-adjacent tetrahedral elements as follows

$$\boldsymbol{M}_m^{i,o}(\boldsymbol{r}) = \begin{cases}\frac{1}{3v_m^{i,1}}(\boldsymbol{r}-\boldsymbol{r}_m^1), & \boldsymbol{r}\in V_m^{i,1}\\ \frac{1}{3v_m^{i,2}}(\boldsymbol{r}-\boldsymbol{r}_m^2), & \boldsymbol{r}\in V_m^{i,2}\end{cases} \tag{6.14}$$

Here $v_m^{i,1}$ and $v_m^{i,2}$ stand for the volumes of the facet-adjacent tetrahedrons $V_m^{i,1}$ and $V_m^{i,2}$ attached to the boundary, lying in the region i and sharing the mth mesh edge.

We define the discretized EO-monopolar-RWG PMCHWT equations directly from expressions (6.12) and (6.13) by keeping the even surface testing and interchanging the odd surface testing with odd volumetric testing strategy. The odd volumetrically tested components of the matrix equation now become

$$\begin{aligned}\iiint\limits_{V_m^{2,1}\cup V_m^{2,2}} \tilde{\boldsymbol{E}}_1^{s,e/o}\cdot\boldsymbol{M}_m^{2,o}dV - \iiint\limits_{V_m^{1,1}\cup V_m^{1,2}} \tilde{\boldsymbol{E}}_2^{s,e/o}\cdot\boldsymbol{M}_m^{1,o}dV \\ = -\iiint\limits_{V_m^{2,1}\cup V_m^{2,2}} \boldsymbol{E}^{inc}\cdot\boldsymbol{M}_m^{2,o}dV\end{aligned} \tag{6.15}$$

$$\begin{aligned}\iiint\limits_{V_m^{2,1}\cup V_m^{2,2}} \tilde{\boldsymbol{H}}_1^{s,e/o}\cdot\boldsymbol{M}_m^{2,o}dV - \iiint\limits_{V_m^{1,1}\cup V_m^{1,2}} \tilde{\boldsymbol{H}}_2^{s,e/o}\cdot\boldsymbol{M}_m^{1,o}dV \\ = -\iiint\limits_{V_m^{2,1}\cup V_m^{2,2}} \boldsymbol{H}^{inc}\cdot\boldsymbol{M}_m^{2,o}dV, \\ 1\leqslant m\leqslant N_e\end{aligned} \tag{6.16}$$

6.2.3 Numerical Implementation

There are a couple of important points related to the numerical implementation of the proposed discontinuous hierarchical discretization technique. Firstly, special care has to be taken when defining the geometry of volumetric testing elements near sharp wedges and corners since they may break out of the null-field region and numerical error may appear (see Fig. 6.1). In this work we define their geometry *conformal* to the boundary (see Chapter 5, Section 5.3.1) taking into account the angles formed by the corresponding field triangle originating from the surface tessellation and the three neighbouring triangles. The accuracy of this implementation can be fine-tuned by adjusting the height of the testing tetrahedral elements (H_m) which in turn is defined with the same value in both regions as a fraction of the length of the *mth* edge, h_m, shared by the corresponding field triangles where the volumetric elements are constructed.

Another important point is that in order to minimize the number of degrees of freedom and keep similar accuracy as in the EO-monopolar-RWG approach, we use the *hybrid* version of the EO-monopolar-RWG discretization scheme of PMCHWT formulation, EO-PMCHWT[hyb]. This scheme assumes the odd monopolar expansion of the currents and the volumetric testing of the fields just over the edges forming the physical sharp wedges and corners, and the conventional RWG-expansion of the currents and testing of the fields over all the mesh edges. Therefore, for a given discretization, this formulation handles a number of degrees of freedom comparable to the RWG-PMCHWT strategy, PMCHWT[R].

In the nonconforming EO-PMCHWT[hyb] scheme, we compute the volumetric integrals over tetrahedra with 11-point cubature rules. The surface and line integrals are computed with a 9-point quadrature rule and the quasi-singular contributions of the kernel are computed analytically for the inner integrals of all the interactions. In the RWG-PMCHWT implementation, the quasi-singular kernel contributions are computed analytically for inner integrals and near interactions only, while the far interaction integrals are computed directly with a 4-point rule.

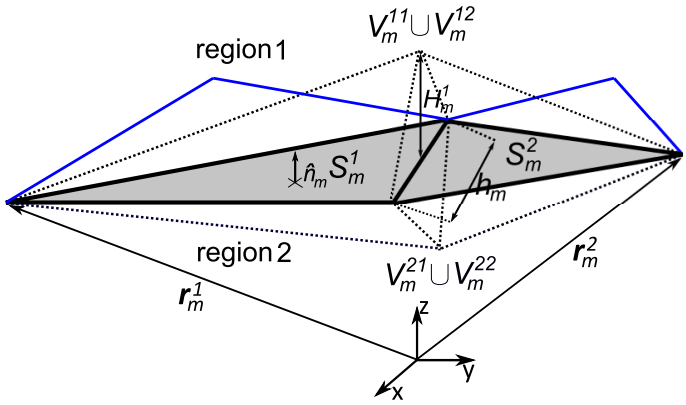

Figure 6.1: Odd monopolar volumetric testing functions defined over a pair of facet-adjacent tetrahedra attached to the corresponding triangular facets and defined inside the region 1 (free-space) and region 2 (plasmonic nanoparticle)

6.3 Numerical results

We present numerical results of the scattering analysis of three sharp-edged plasmonic nanoparticles, namely, a hexahedron, an octahedron, and a tetrahedron, discretized with geometrically conformal meshes. We choose such particles since their modelling is especially convoluted due to the singular field behaviour induced near sharp edges and corners. In addition, for these particles, the redshift (resonances shift to the higher wavelengths) in scattering and absorption spectra and the improvements in near-field computed with our nonconforming EO-PMCHWT[hyb] implementation when compared to the PMCHWT[R] implementation is especially evident. In all examples, the scattered fields are computed under an impinging $+z$ propagating x-polarized plane wave. All particles analyzed here are of equal volume ($V = 50^3$ nm^3).

6.3.1 Scattering and absorption spectra in resonance domain

We focus on scattering and absorption spectra around two main resonances. For all three particles, we present three different sets of results. First, we compute the resonant efficiencies with our nonconforming EO-PMCHWT[hyb] implementation and several values of the heights of the testing elements H to illustrate the effect of H on the accuracy of the results. We compare these results to the ones computed with the PMCHWT[R] discretization technique. Next, we plot the induced electric and magnetic surface charges and currents for the first two resonances, indicating the strongly singular behaviour over the sharp edges and corners of the particle. Finally, a comparative convergence plot of the main resonant peaks is presented, illuminating further the achieved enhancement of the proposed new discretization technique versus the standard scheme. The scattering and absorption efficiencies are computed directly from the surface currents and MoM matrices according to the expressions given in [130]. All the meshes used in the computation of scattering and absorption spectra are structured without h-refinements.

6.3.1.1 Plasmonic hexahedron (cube)

The electromagnetic response of a hexahedron, or commonly known as the cube, has been studied intensively during the last 50 years (see [117] and references therein). From Fig. 6.2 we can notice the redshift of the first (dipole) and second (quadrupole) resonances obtained with nonconforming EO-PMCHWT[hyb] and N=7440 when compared to the resonances obtained with PMCHWT[R] and $N = 8712$ unknowns for both electric and magnetic currents. Furthermore, for the best performing H, where the height of testing elements is equal to the mesh parameter, H=h, the observed redshift is even more pronounced, surpassing the spectra computed with PMCHWT[R] and 18432 unknowns. In Fig. 6.3 we can notice singular surface currents and charges around sharp corners. In particular, the surface electric charge density and surface magnetic current density show extremely singular nature around sharp vertices for both resonances. In Fig. 6.4 we show the convergence trends of the resonant wavelengths for the first two resonances in the scattering and absorption spectra, respectively, versus the number of degrees of freedom N. The results are computed with the EO-PMCHWT[hyb] and best performing H and compared to the results computed with the standard PMCHWT[R] discretization. Our hybrid discontinuous scheme exhibits faster convergence of resonant wavelengths compared to the RWG implementation when the number of unknowns is increased. In particular, the dipole and quadrupole resonances computed with our nonconforming scheme, and H=h, have been marked around the incident wavelengths of 428nm and 393nm, respectively, using around 16560 unknowns for the electric and magnetic currents (see Fig. 6.4).

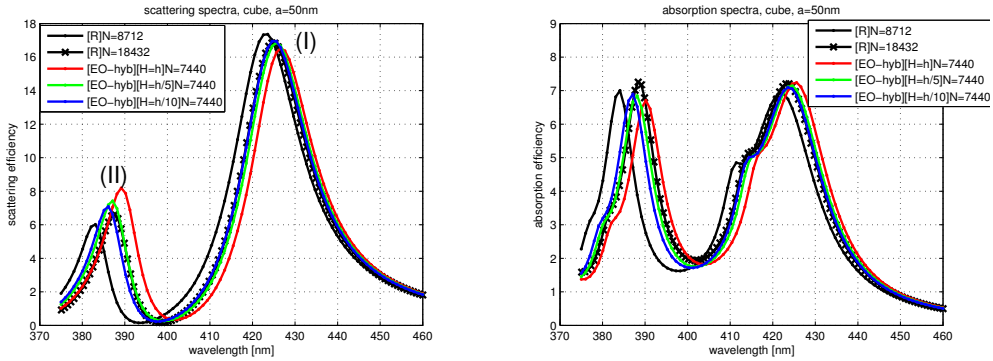

(a) **(b)**

Figure 6.2: Scattering (a) and absorption (b) spectra for a hexahedron (cube) with edge length a = 50nm. The first resonance (I) exposes strong coupling with the incident field (scattering efficiency $\approx$ 17). Resonance (II) shows moderate scattering amplitude (scattering efficiency $\approx$ 7), but the absorption maximum is about the same magnitude as with the first resonance

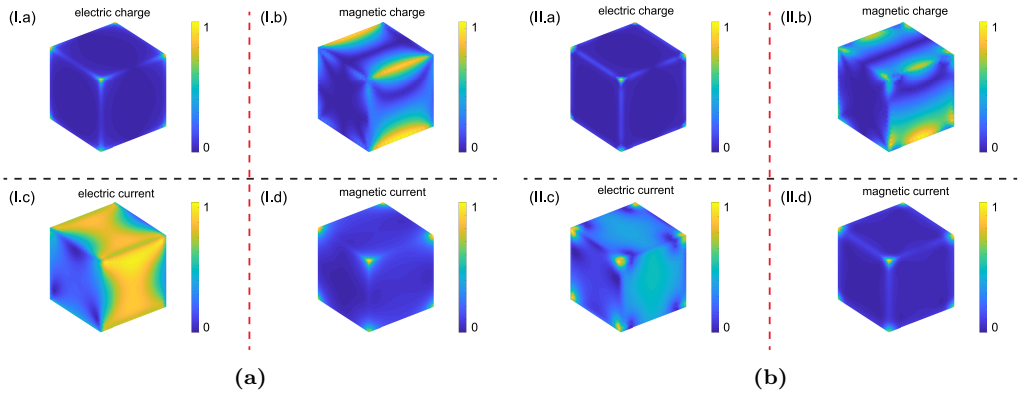

Figure 6.3: Normalized absolute values of electric and magnetic charges and currents around dipole (I) and quadrupole (II) resonances for a cube with edge length $a = 50$nm. The colors indicate minimum (blue) to maximum (yellow) normalized charge and current values. Electric charge densities (I.a and II.a) and magnetic current densities (I.d and II.d) exhibits extremely singular nature around corners for both resonances

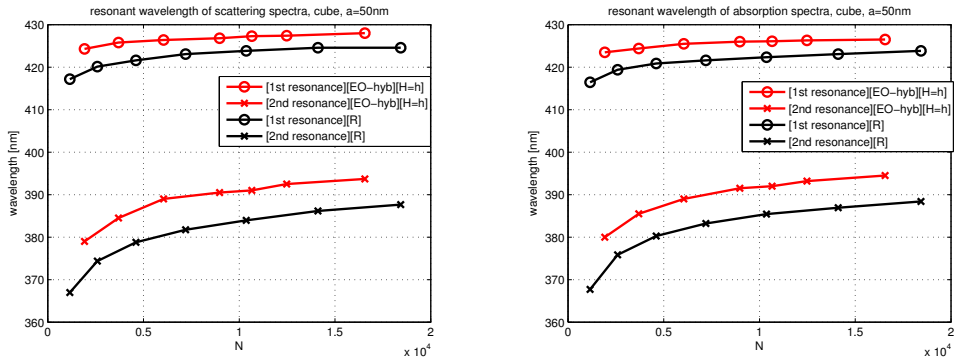

Figure 6.4: Convergence of the resonant wavelengths of two main resonances in scattering spectra (a) and absorption spectra (b) versus the number of degrees of freedom for the same hexahedron inclusion as in Fig. 6.2

6.3.1.2 Plasmonic octahedron

The octahedron has the dual shape of the cube and the solid angle sharper than the cube, however, smoother than the one of the tetrahedron [117]. Therefore, we expect that its two main resonances are going to be redshifted when compared to the cube, but blueshifted (shifted to lower wavelengths) when compared to the tetrahedron [117]. Similarly to the cube, the redshift of the two main resonances computed with EO-PMCHWT[hyb] and different values of H with N=6528 degrees of freedom compared to the resonances computed with PMCHWT[R] and N=7776 degrees of freedom is recognized in Fig. 6.5. In light of Fig. 6.6, a strong concentration of surface field quantities is found around sharp corners. The two resonances can not be distinguished solely by looking in electric

charge and magnetic current distributions because they are too singular and concentrated around vertices. However, the surface magnetic charge and electric current show different nature for the dipole and quadrupole resonance. Furthermore, in view of Fig. 6.7, faster convergence of the resonant wavelengths computed with EO-PMCHWT[hyb] and $H{=}h$ when compared to the resonant wavelengths computed with PMCHWT[R] is observed when the number of unknowns is increased. We were able to spot the resonant wavelengths of the first and second resonances around 436nm and 400nm, respectively, with our nonconforming implementation and around 16840 degrees of freedom for the electric and magnetic currents (see Fig. 6.7).

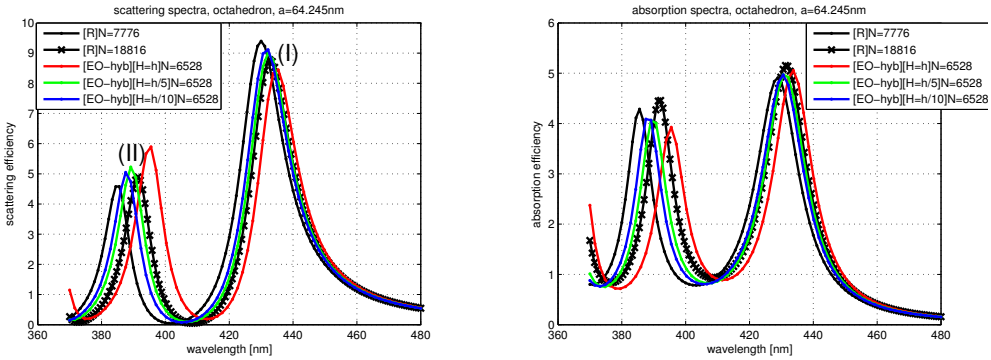

Figure 6.5: Scattering (a) and absorption (b) efficiency spectra for the octahedral inclusion of edge length $a = 64.245$nm. In this case the maximum scattering and absorption efficiency values are close to 10 and 5, respectively

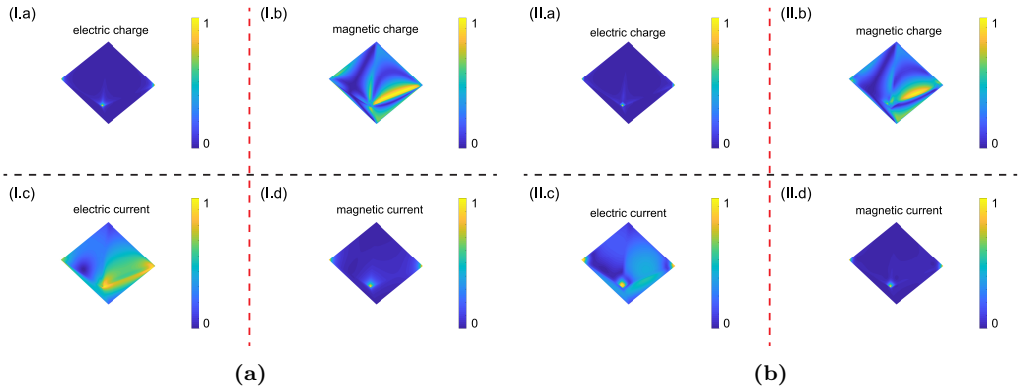

Figure 6.6: Normalized absolute values of electric and magnetic charges and currents around two main resonances for an octahedron with edge length $a = 64.245$nm. Similarly to cube, we notice strong singular field quantities near sharp edges and corners. The two resonances can be distinguished by looking at the surface magnetic charge and electric current distributions

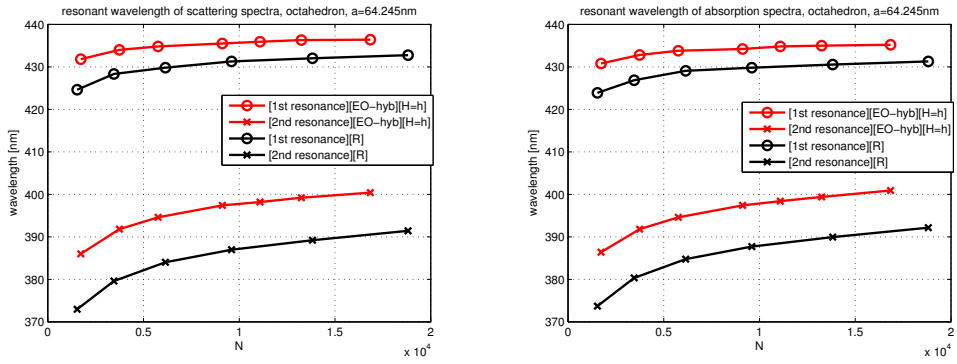

(a) **(b)**

Figure 6.7: Convergence of the resonant wavelengths of two main resonances versus the number of degrees of freedom for the scattering (a) and absorption (b) efficiency of the octahedral inclusion. The EO-PMCHWT[hyb] scheme indicates faster convergence with respect to the standard RWG discretization scheme

6.3.1.3 Plasmonic tetrahedron

The tetrahedron is the sharpest member of the Platonic solids and its plasmonic resonances are redshifted compared to the other members [117]. In view of Fig. 6.8, we can notice the redshift of the scattering and absorption spectra computed with our hybrid discontinuous implementations and N=4104 unknowns with respect to the RWG implementation and N=4800 unknowns. Similarly to the cube and octahedron, strong singular fields are present near sharp features of the particle (Fig. 6.9).

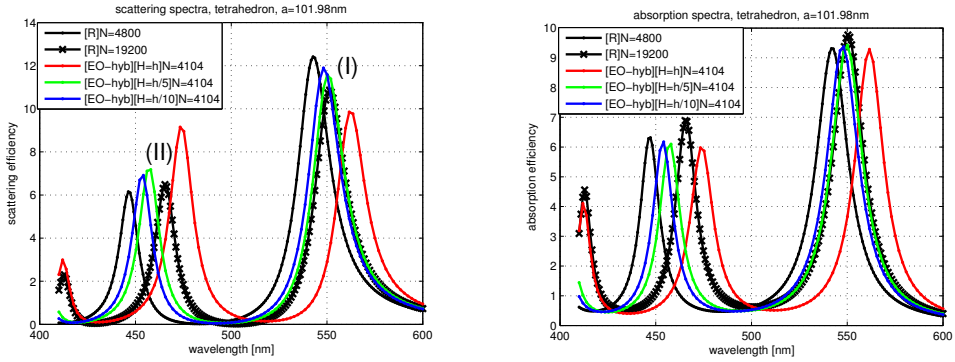

(a) **(b)**

Figure 6.8: The scattering (a) and absorption (b) efficiency spectra for the tetrahedral particle of edge length a = 101.98nm depicting the first two resonances. We can spot the maximum scattering and absorption efficiency values around 12 and 10, respectively

Again, the two resonances are indistinguishable from the plots of surface electric charge and magnetic current since they are focused near sharp vertices. Instead, one should look

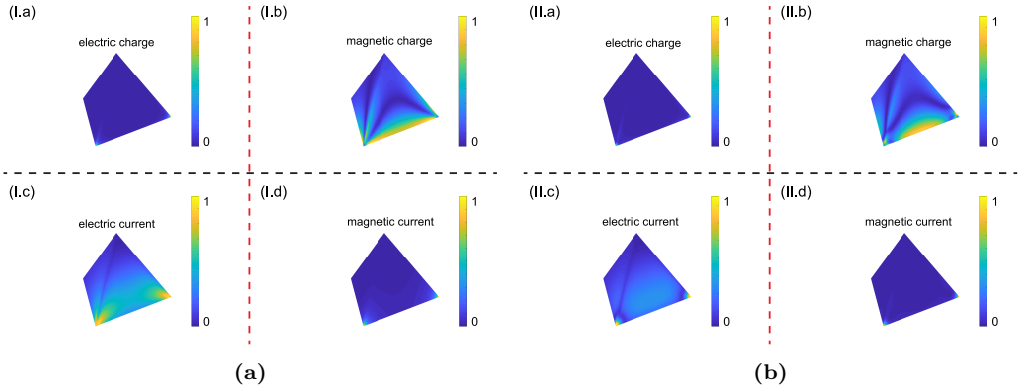

Figure 6.9: Normalized absolute values of electric and magnetic charges and currents around first (I) and second (II) resonances for a tetrahedron with edge length $a = 101.98$nm. Very strong singular behaviour of surface electric charge and magnetic current densities is visible near the sharp vertices

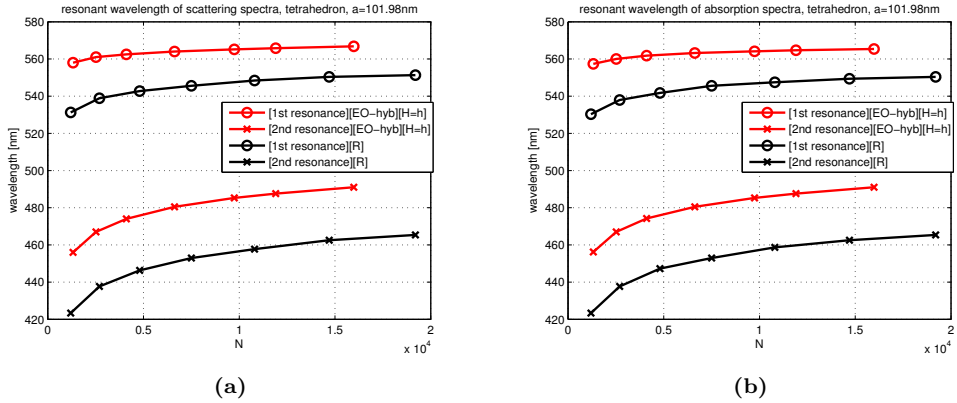

Figure 6.10: Convergence of the resonant wavelengths of two main resonances in scattering (a) and absorption (b) efficiency spectra versus the number of degrees of freedom for the same tetrahedron as in Fig. 6.8

at the surface magnetic charge and electric current distributions, which show distinct nature for particular resonance. According to Fig. 6.10, we can detect faster convergence of the resonant wavelengths computed with EO-PMCHWT[hyb] when compared to the resonant wavelengths computed with PMCHWT[R] as the number of degrees of freedom is increased. In particular, we were able to spot the first and second resonance in the scattering and absorption spectra around the incident wavelengths of 565nm and 490nm, respectively, using our EO-PMCHWT[hyb] implementation with $H{=}h$ and around 16000 unknowns for the electric and magnetic currents (see Fig. 6.10).

6.3.2 Near-field computations in resonance domain

The results of the previous section indicate that faster convergence in the far field region can be obtained with the proposed EO-PMCHWT[hyb] scheme than with PMCHWT[R]. Next, we test the near-field accuracy of our EO-PMCHWT[hyb] formulation around two main resonances in the scattering spectra of a plasmonic cube with edge length $a = 50$nm. For this purpose we define the root-mean-square (rms) near-field relative error e_{near} as follows

$$e_{near} = \frac{\left[\sum_{j=1}^{K} \left|\tilde{\boldsymbol{E}}_s(\boldsymbol{r}_j) - \boldsymbol{E}_s^{REF}(\boldsymbol{r}_j)\right|^2 + \eta_0^2 \sum_{j=1}^{K} \left|\tilde{\boldsymbol{H}}_s(\boldsymbol{r}_j) - \boldsymbol{H}_s^{REF}(\boldsymbol{r}_j)\right|^2\right]^{1/2}}{\left[\sum_{j=1}^{K} \left|\boldsymbol{E}_s^{REF}(\boldsymbol{r}_j)\right|^2 + \eta_0^2 \sum_{j=1}^{K} \left|\boldsymbol{H}_s^{REF}(\boldsymbol{r}_j)\right|^2\right]^{1/2}} \tag{6.17}$$

where $\tilde{\boldsymbol{E}}_s$ and $\tilde{\boldsymbol{H}}_s$ denote the scattered electric and magnetic fields, respectively, computed with the EO-PMCHWT[hyb] or PMCHWT[R] implementation. The reference scattered fields, $\boldsymbol{E}_s^{REF}$ and $\boldsymbol{H}_s^{REF}$, are computed with standard PMCHWT[R] implementation on an unstructured mesh with h-refinement around sharp edges and corners and maximum number of degrees of freedom (18432) for the electric and magnetic currents. The near-fields are computed on a set of K points distributed along the line with length 100nm defined 2.5nm above the edge of the cube (see Fig. 6.11(a)). In our experiment we adopt $K = 200$ and the fields $\tilde{\boldsymbol{E}}_s$ and $\tilde{\boldsymbol{H}}_s$ are computed using a structured mesh without h-refinement.

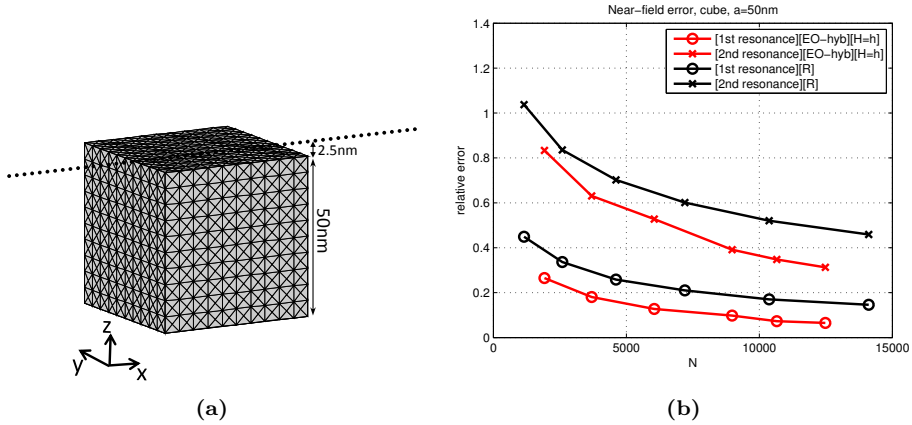

(a) **(b)**

Figure 6.11: (a): Distribution of the points near a plasmonic cube, above one of the edges, that are used in the near-field accuracy tests. (b): Near-field relative error at the first and second resonances computed with the nonconforming [EO-hyb] and standard [R] implementations versus the number of degrees of freedom N for a plasmonic cube with side $a = 50$nm

In Fig. 6.11(b) we show the relative rms near-field errors versus the number of degrees of freedom N computed with EO-PMCHWT[hyb] ($H = h$) and PMCHWT[R] implementations. In light of Fig. 6.11(b), we can observe smaller near-field errors obtained with

the EO-PMCHWT[hyb] scheme and fewer number of unknowns when compared to PMCHWT[R].

6.4 Conclusions

We have introduced a hierarchical discontinuous method of moments discretization of PMCHWT integral equation formulation applied to the scattering analysis of plasmonic subwavelength nanoparticles with sharp-vertices in their resonance domain. The unknown electric and magnetic surface current densities are expanded with edge-based even and odd monopolar-RWG subsets, which stand for a hierarchical rearrangement of the monopolar-RWG set. To make the problematic singular kernel contributions numerically manageable, the fields are tested over pairs of small tetrahedral elements attached to the triangles on the boundary-surface and lying in the null-field region.
The proposed technique appears to have improved performance features in the scattering analysis of plasmonic nanoparticles with sharp edges and corners. For these particles singular field quantities around geometric singularities dominate the physical result, creating a slow (or no) convergent solutions, particularly if standard discretization techniques are applied. The observed accuracy-boost of the proposed implementation is attributed to the better singular charge and current modelling near the sharp edges and corners with a discontinuous expansion of the currents together with the volumetric testing of the fields close to the boundary of the target. The accuracy of our results was tested for both far-field and near-field characteristics, supporting an overall improvement in both domains.
In particular, we observe that the redshift in the scattering and absorption spectra around two main resonances, for the cases of canonical sharp-edged targets considered here, becomes more evident as the height of testing elements H increases up to the maximum value of the mesh parameter h. Additionally, we noticed a slower convergence of the second resonance compared to the resonant wavelength of the first resonance as the number of degrees of freedom increases. This indicates that the higher order modes experience slower convergence than the lower ones.
Three different particles were purposefully presented in an increasing sharpness manner, i.e., the solid vertex for the cube is $\pi/2$ (rad), for the octahedron 1.359 (rad), and for the tetrahedron 0.551 (rad). With this categorization, we can deduce that the proposed nonconforming EO-PMCHWT[hyb] scheme exhibits faster convergence compared to the conventional PMCHWT[R] scheme as the solid vertex decreases, i.e., sharper particles. Alternatively, the sharper the solid, the less degrees of freedom are required for our nonconforming implementation to reach the same accuracy as with the standard RWG implementation. This fact can be of particular interest for modelling even sharper naturally or artificially occurring particles reducing at the same time the required mesh burden, paving the way towards the efficient computational exploration of the resonant physics and the design prospects of sharp nanoscatterers. The same methodology could also be utilized in incorporating quantum corrected classical models that require a hybrid surface-volume treatment that capture electron tunnelling and electron spill-out effects.

Chapter 7
Conclusions and Future Lines

7.1 Conclusions

In this work, we have presented innovative schemes of discretization for most prominent surface integral equations, EFIE for the scattering analysis of PEC targets, and PMCHWT for the scattering analysis of homogeneous penetrable targets. We expand the unknown currents with discontinuous vector facet-based monopolar-RWG basis functions. This discretization technique is much more flexible than standard edge-based divergence-conforming scheme since it allows the analysis of geometrically nonconformal meshes and alleviates the preprocessing burden in the single-trace study of piecewise homogeneous composite objects with junctions. Furthermore, the discontinuous transition of the currents allows for more flexible integral equation domain decomposition methods reducing in the same time the number of degrees of freedom and the preprocessing load.
However, the discontinuous discretization of associated integral operators comes with an additional computational cost. In the Galerkin discretization with discontinuous basis functions of the hypersingular part of the electric field integral operator, which is associated with the EFIE and the PMCHWT, problematic unbounded integrals arise. In order to avoid this problem, we build the monopolar-RWG discretized equations with two types of specifically tailored testing approaches. In the volumetric testing scheme, we define our testing functions on volumetric elements, tetrahedra or wedges, attached to the meshed boundary and lying in the null-field region. This strategy is rather computationally expensive since additional volumetric and line integrals have to be computed. The second testing technique, tangential-normal, carries out the testing of the scattered fields with RWG basis functions over two edge-adjacent triangles such that one triangle matches the facet arising in the mesh of the surface and another lies in the region where the fields are constrained to be zero according to the equivalence principle. The tangential-normal monopolar-RWG scheme of discretization avoids the computation of volumetric integrals and becomes computationally cheaper when compared to the volumetric scheme.
Both discretization approaches, volumetric and tangential-normal, involve only weakly singular integrals that can be readily computed with standard available numerical libraries. Our extensive numerical tests show that the volumetric discontinuous discretization approach offers more accuracy and stability in the analysis of geometrically nonconformal or defective meshes when compared to the tangential-normal technique. Apart from the inherent flexibility, our discontinuous schemes show superior accuracy and convergence in both near-field and far-field regions compared to standard RWG-schemes in

the analysis of sharp-edged targets where singular surface field quantities are induced around abrupt geometrical singularities.
Therefore, with this work, we advance the state of the art in three directions:

- Flexible analysis of nonconformal meshes that often arise in the modular design of complex objects is made possible.
- The programming burden in the analysis of piecewise homogeneous composite objects with junctions is alleviated.
- The accuracy in the electromagnetic scattering analysis of targets with sharp edges and corners (electrically small PEC or penetrable) is improved.

7.2 Future research lines

Future research in the discontinuous discretization of integral equations may encompass the following topics:

- Discontinuous discretization of the CFIE for PEC targets with monopolar-RWG basis functions and testing of the fields with tangential-normal or volumetric testing functions can be implemented. An exhaustive study of the accuracy and convergence of the new formulation should be conducted. This research is underway.
- New schemes of testing the monopolar-RWG discretized integral equations that will produce, similarly to tangential-normal and volumetric testing, weakly singular integrals and better accuracy in the analysis of sharp-edged targets can be explored.
- Further research in the modelling of plasmonic nanoantennas with our discontinuous approaches should be conducted. There are possible improvements in the accurate computation of the forces and torques in the plasmonic systems involving sharp-edged nanoparticles.
- Discontinuous discretization of other integral equations used in the scattering analysis of penetrable targets such are CTF or NMüller formulation is possible and can be studied.
- Automatic h-refinement based on the local residual error and our discontinuous schemes can be implemented.

Bibliography

[1] J. C. Maxwell, "A Dynamical Theory of the Electromagnetic Field," *Philosophical Transactions of the Royal Society of London* 155, 459–512 (1865)

[2] G. Mie, "Beitrage zur Optik trüber Medien, speziell kolloidaler Metallösungen," *Ann. Phys.* 330(3) (1908) 377–445.

[3] J. M. Jin, *The Finite Element Method in Electromagnetics*, Wiley-IEEE Press, April 2014.

[4] P. P. Silvester and R. L. Ferrari, *Finite Elements for Electrical Engineers*, 3rd ed. Cambridge: Cambridge University Press, 1996.

[5] K. Yee, "Numerical solution of initial boundary value problems involving Maxwell's equations in isotropic media," *IEEE Trans. Antennas Propag.*, vol. AP-14, No. 8, pp. 302-307, May 1966.

[6] P. Johns and R. Beurle, "Numerical solution of 2-dimensional scattering problems using a transmission-line matrix," *Proc. IEE*, vol. 118, pp. 1203–1208, Sept. 1971.

[7] J. Berenger, "A perfectly matched layer for the absorption of electromagnetic waves," *J. Comput. Phys.* 114(2) (1994) 185–200.

[8] G. Green, "An essay on the application of mathematical analysis to the theories of electricity and magnetism," Nottingham (1828)

[9] R. F. Harrington, *Field Computation by Moment Methods*, Krieger Publishing Co., Inc., 1968.

[10] J. M. Rius, E. Ubeda, and J. Parron, "On the testing of the magnetic field integral equation with RWG basis functions in method of moments," *IEEE Trans. Antennas Propag.*, vol. 49, no. 11, pp. 1550–1553, Nov. 2001.

[11] E. Ubeda and J. M. Rius, "Novel monopolar MoM-MFIE discretization for the scattering analysis of small objects," *IEEE Trans. Antennas Propag.*, vol. 54, no. 1, pp. 50–57, Jan. 2006

[12] K. Cools, F. P. Andriulli, D. De Zutter, and E. Michielssen, "Accurate and conforming mixed discretization of the MFIE," *IEEE Antennas Wireless Propag. Lett.*, vol. 10, pp. 528–531, Jun. 2011.

[13] F. P. Andriulli, K. Cools, H. Bagci, F. Olyslager, A. Buffa, S. Christiansen, and E. Michielssen, "A multiplicative Calderón preconditioner for the electric field integral equation," *IEEE Trans. Antennas Propag.*, vol. 56, no. 8, pp. 2398–2412, Aug. 2008.

[14] D. R. Wilton and A. W. Glisson, "On improving the electric field integral equation at low frequencies," in *Radio Science Meeting Dig.*, Los Angeles, CA, 1981, pp. 24–24.

[15] W. L. Wu, A. W. Glisson, and D. Kajfez, "A study of two numerical solution procedures for the electric field integral equation at low frequency," *Appl. Comput. Soc. J.*, vol. 10, no. 3, 69–80, 1995.

[16] G. Vecchi, "Loop-star decomposition of basis functions in the discretization of the EFIE," *IEEE Trans. Antennas Propag.*, vol. 47, no. 2, pp. 339–346, Feb. 1999.

[17] J. F. Lee, R. Lee, and R. J. Burkholder, "Loop star basis functions and a robust preconditioner for EFIE scattering problems," *IEEE Trans. Antennas Propag.*, vol. 51, no. 8, pp. 1855–1863, Aug. 2003.

[18] P. Ylä-Oijala, J. Markkanen, S. Järvenpää, and S. P. Kiminki, "Surface and volume integral equation methods for time-harmonic solutions of Maxwell's equations," *Progress In Electromagnetics Research*, vol. 149, pp. 15–44, 2014.

[19] A. J. Poggio and E. K. Miller, "Integral equation solutions of three dimensional scattering problems," in *Computer Techniques for Electromagnetics*, R. Mittra, Ed. Oxford, U.K.: Pergamon, 1973, ch. 4.

[20] T. K. Wu and L. L. Tsai, "Scattering from arbitrarily-shaped lossy dielectric bodies of revolution," *Radio Sci.*, vol. 12, pp. 709–718, Sep./Oct. 1977.

[21] Y. Chang and R. F. Harrington, "A surface formulation for characteristic modes of material bodies," *IEEE Trans. Antennas Propag.*, vol. 25, no. 6, pp. 789–795, Nov. 1977.

[22] P. Ylä-Oijala, M. Taskinen, and S. Järvenpää, "Surface integral equation formulations for solving electromagnetic scattering problems with iterative methods," *Radio Science*, vol. 40, no. 6, 2005.

[23] C. Müller, *Foundations of the mathematical theory of electromagnetic waves*, Springer, Berlin, 1969.

[24] J. Song, C. C. Lu, and W. C. Chew, "Multilevel fast multipole algorithm for electromagnetic scattering by large complex objects," *IEEE Trans. Antennas Propag.*, vol. 45, no. 10, pp.1488–1493, Oct. 1997.

[25] E. Michielssen and A. Boag, "A multilevel matrix decomposition algorithm for analyzing scattering from large structures," *IEEE Trans. Antennas Propag.*, vol. 44, pp. 1086- 1093, Aug. 1996.

[26] J. M. Rius, J. Parron, E. Ubeda, and J. R. Mosig, "Multilevel matrix decomposition algorithm for analysis of electrically large electromagnetic problems in 3-D," *Microwave and Optical Technology Letters*, vol. 22, pp. 177-182, Aug. 1999.

[27] M. Bebendorf, "Approximation of boundary element matrices," *Numer.Math.*, vol. 86, no. 4, pp. 565–589, 2000.

[28] M. Taskinen and P. Ylä-Oijala, "Current and charge integral equation formulation," *IEEE Trans. Antennas Propag.*, vol. 54, no. 1, 58–67, 2006.

[29] G. C. Hsiao and R. E. Kleinman, "Mathematical foundation for error estimation in numerical solution of integral equations in electromagnetics," *IEEE Trans. Antennas Propag.*, vol. 45, no. 3, pp. 316-328, March 1997.

[30] Z. Peng, X. C. Wang, and J.F. Lee, Integral equation based domain decomposition method for solving electromagnetic wave scattering from non-penetrable objects, *IEEE Trans. Antennas Propag.*, vol. 59, no. 9, pp. 3328—3338, Sep. 2011.

[31] M. A. E. Bautista, F. Vipiana, M. A. Francavilla, J. A. T. Vasquez, and G. Vecchi, "A nonconformal domain decomposition scheme for the analysis of multiscale structures," *IEEE Trans. Antennas Propag.*, vol. 63, no. 8, pp. 3548–3560, Aug. 2015.

[32] Z. Peng, R. Hiptmair, Y. Shao, and B. MacKie-Mason, "Domain decomposition preconditioning for surface integral equations in solving challenging electromagnetic scattering problems," *IEEE Trans. Antennas Propag.*, vol. 64, no. 1, pp. 210–223, Jan. 2016.

[33] I. Sekulic, E. Ubeda, and J. M. Rius, "Nonconforming domain decomposition method for the flexible analysis of multiscale penetrable structures," *Computing and Electromagnetics International Workshop (CEM)*, Stellenbosch, South Africa, 2018.

[34] S. M. Rao, D. R. Wilton, and A. W. Glisson, "Electromagnetic scattering by surfaces of arbitrary shape," *IEEE Trans. Antennas Propag.*, vol. 30, no. 3, pp. 409–418, May 1982.

[35] P. Monk, *Finite Element Methods for Maxwell's Equations*. Oxford, U.K.: Clarendon, 2003.

[36] B. M. Kolundzija and B. D. Popovic, "Entire-domain Galerkin method for analysis of metallic antennas and scatterers," *IEE Proceedings-H*, vol. 140, no. 1, pp. 1–10, Feb. 1993.

[37] B. D. Popovic and B. M. Kolundzija, *Analysis of Metallic Antennas and Scatterers*, The Institution of Electrical Engineers, London, UK, 1994.

[38] B. M. Notaros and B. D. Popovic "General entire-domain method for analysis of dielectric scatterers," *IEE Proc.-Microw. Antennas Propag.*, vol. 143, no. 6, pp. 498–504, Dec. 1996.

[39] R. D. Graglia, D. R. Wilton, and A. F. Peterson, "Higher order interpolatory vector bases for computational electromagnetics," *IEEE Trans. on Antennas Propag.*, vol. 45, no. 3, pp. 329–342, March 1997.

[40] A. F. Peterson, *Mapped Vector Basis Functions for Electromagnetic Integral Equations*, Morgan & Claypool Publishers, February, 2006.

[41] R. D. Graglia and G. Lombardi, "Singular higher order divergence conforming bases of additive kind and moments method applications to 3D sharp-wedge structures," *IEEE Trans. Antennas Propag.*, vol. 56, no. 12, pp. 3768–3788, Dec. 2008.

[42] P. Ylä-Oijala, S. P. Kiminki, J. Markkanen, and S. Järvenpää, "Error-controllable and well-conditioned MoM solutions in computational electromagnetics: Ultimate surface integral-equation formulation," *IEEE Antennas Propag. Mag.*, vol. 55, no. 6, pp. 310–331, Dec. 2013.

[43] P. Ylä-Oijala, S. P. Kiminki, and S. Järvenpää, "Conforming testing of electromagnetic surface-integral equations for penetrable objects," *IEEE Trans. Antennas Propag.*, vol. 64, no. 6, pp. 2348–2357, Jun. 2016.

[44] R. Hiptmair and C. Schwab, "Natural boundary element methods for the electric field integral equation on polyhedra," *SIAM J. Numer. Anal.*, vol. 40, no. 1, pp. 66–86, 2002.

[45] A. Buffa, R. Hiptmair, T. von Petersdorff, and C. Schwab, "Boundary element methods for Maxwell transmission problems in Lipschitz domains," *Numer. Math.*, vol. 95, no. 3, pp. 459–485, 2003.

[46] J. M. Putnam, L. N. Medgyesi-Mitschang, "Combined field integral equation formulation for inhomogeneous two-and three-dimensional bodies: the junction problem," *IEEE Trans. Antennas Propag.*, vol. 39, no. 5, pp. 667–672, May 1991.

[47] L. N. Medgyesi-Mitschang, J. M. Putnam, and M. B. Gedera, "Generalized method of moments for three-dimensional penetrable scatterers," *J. Opt. Soc. Am. A*, vol. 11, no. 4, pp. 1383–1398, Apr. 1994.

[48] B. M. Kolundzija, "Electromagnetic modeling of composite metallic and dielectric structures," *IEEE Trans. Microw. Theory Tech.*, vol. 47, no. 7, pp. 1822–1825, Jul. 1999.

[49] M. Carr, E. Topsakal, and J. L. Volakis, "A procedure for modeling material junctions in 3-D surface integral equation approaches," *IEEE Trans. Antennas Propag.*, vol. 52, no. 5, pp. 1374–1379, May 2004.

[50] P. Ylä-Oijala, M. Taskinen, and J. Sarvas, "Surface integral equation method for general composite metallic and dielectric structures with junctions," *Progress In Electromagnetics Research*, vol. 52, pp. 81–108, 2005.

[51] Y. Chu, W. C. Chew, J. Zhao, and S. Chen, "A surface integral equation formulation for low-frequency scattering from a composite object," *IEEE Trans. Antennas Propag.*, vol. 51, no. 10, pp. 2837–2844, Oct. 2003.

[52] Z. Peng, K. H. Lim, and J. F. Lee, "Computations of electromagnetic wave scattering from penetrable composite targets using a surface integral equation method with multiple traces," *IEEE Trans. Antennas Propag.*, vol. 61, no. 1, pp. 256–270, Jan. 2013.

[53] Z. Peng, K. H. Lim, and J. F. Lee, "A discontinuous Galerkin surface integral equation method for electromagnetic wave scattering from nonpenetrable targets," *IEEE Trans. Antennas Propag.*, vol. 61, no. 7, pp. 3617–3628, Jul. 2013.

[54] E. Ubeda, J. M. Rius, and A. Heldring, "Nonconforming discretization of the electric-field integral equation for closed perfectly conducting objects," *IEEE Trans. Antennas Propag.*, vol. 62, no. 8, pp. 4171–4186, Aug. 2014.

[55] E. Ubeda, J. M. Rius, A. Heldring, and I. Sekulic, "Volumetric testing parallel to the boundary surface for a nonconforming discretization of the electric field integral equation," *IEEE Trans. Antennas Propag.*, vol. 63, no. 7, pp. 3286–3291, Jul. 2015.

[56] E. Ubeda, I. Sekulic, A. Heldring, and J. M. Rius, "Tangential-normal surface testing for the nonconforming discretization of the electric field integral equation," *IEEE Antennas Wireless Propag. Lett.*, vol. 15, pp. 1581–1584, Jan. 2016.

[57] I. Sekulic, E. Ubeda, and J. M. Rius, "Nonconforming discretization of the PMCHWT integral equation applied to arbitrarily shaped dielectric objects," *Proc. European Conference on Antennas and Propagation (EuCAP)*, Paris, Mar. 2017, pp. 311-314.

[58] I. Sekulic, E. Ubeda, and J. M. Rius, "Versatile and accurate schemes of discretization in the scattering analysis of 2D composite objects with penetrable or perfectly conducting regions," *IEEE Trans. Antennas Propag.*, vol. 65, no. 5, pp. 2494–2506, May 2017.

[59] I. Sekulic, E. Ubeda, and J. M. Rius, "Improved accuracy in the scattering analysis of arbitrarily shaped ferromagnetic objects,"*Proc. International Conference on Numerical Electromagnetic and Multiphysics Modeling and Optimization for RF, Microwave, and Terahertz Applications (NEMO)*, Sevilla, May 2017, pp. 167-169.

[60] I. Sekulic, E. Ubeda, and J. M. Rius, "Volumetric testing with wedges for a nonconforming discretization of the PMCHWT formulation,"*Proc. Computing and Electromagentics International Workshop (CEM)*, Barcelona, June 2017, pp. 7-8.

[61] B. B. Kong and X. Q. Sheng, "A discontinuous Galerkin surface integral equation method for scattering from multiscale homogeneous objects," *IEEE Trans. Antennas Propag.*, vol. 66, no. 4, pp. 1937–1946, April 2018.

[62] I. Sekulic, E. Ubeda, and J. M. Rius, "Versatile and accurate schemes of discretization for the electromagnetic scattering analysis of arbitrarily shaped piecewise homogeneous objects," *J. Comput. Phys.*, vol. 374, pp. 478-494, Dec. 2018.

[63] I. Sekulic, E. Ubeda, and J. M. Rius, "Versatile and accurate electromagnetic analysis of piecewise homogeneous composite objects," *Proc. European Conference on Antennas and Propagation (EuCAP)*, London, April 2018, pp. 1-4.

[64] K. Han, Y. Chen, X. Que, M. Jiang, J. Hu, and Z. Nie, "A domain decomposition scheme with curvilinear discretizations for solving large and complex PEC scattering problems," *IEEE Antennas Wireless Propag. Lett.*, vol. 17, no. 2, pp. 242–246, Feb. 2018.

[65] O. Heaviside, "On electromagnetic waves, especially in relation to the vorticity of the impressed forces, and the forced vibration of electromagnetic systems," *Philos. Mag.*, vol. 25, pp. 130–156, 1888.

[66] A. Einstein, "Zur Elektrodynamik bewegter Körper," *Annalen der Physik* vol. 17, pp. 891-921, 1905.

[67] J. D. Jackson, *Classical Electrodynamics*, John Wiley & Sons, New York, 1962.

[68] A. Guissard, "On the surface field integral equations," *IEEE Trans. Educ.*, vol. 46, no. 4, pp. 486-495, Nov. 2003.

[69] J. R. Mautz and R. F. Harrington, "H-field, E-field, and combined-field solutions for conducting bodies of revolution," Archiv für Elektronik und Übertragungstechnik (Electronics and Communication), vol. 32, no. 4, pp. 157–164, 1978.

[70] A. Buffa and S. H. Christiansen, "A dual finite element complex on the barycentric refinement," *Math. Comput.*, vol. 260, pp. 1743–1769, 2007.

[71] Ö. Ergül and L. Gürel, "The use of curl-conforming basis functions for the magnetic-field integral equation," *IEEE Trans. Antennas Propag.*, vol. 54, no. 7, pp. 1917–1926, July 2006.

[72] K. Umashankar, A. Taflove, and S. M. Rao, "Electromagnetic scattering by arbitrary shaped three-dimensional homogeneous lossy dielectric objects," *IEEE Trans. Antennas Propag.*, vol. 34, no. 6, pp. 758–766, June 1986.

[73] R. F. Harrington, *Time-Harmonic Electromagnetic Fields*, Piscataway, NJ, USA: IEEE Press, 2001.

[74] A. F. Peterson, S.L. Ray, and R. Mittra, *Computational Methods for Electromagnetics*, Piscataway, NJ, USA: IEEE Press, 1998.

[75] E. Arvas, Y. Qian, T. K. Sarkar, and F. Aslan, "TE scattering from a conducting cylinder of arbitrary cross section covered by multiple layers of lossy dielectrics," *IEE Proc. H-Microw. Antennas Propag.*, vol. 136, no. 6, pp. 425–430, Dec. 1989.

[76] A. A. Kishk, W. A. Glisson, and M. P. Goggans, "Scattering from conductors coated with materials of arbitrary thickness," *IEEE Trans. Antennas Propag.*, vol. 40, no. 1, pp. 108–112, Jan. 1992.

[77] J. Van Bladel, *Singular Electromagnetic Fields and Sources*, Oxford, U.K.: Clarendon, 1991.

[78] R. Mittra and S. W. Lee, *Analytical Techniques in the Theory of Guided Waves*, New York, NY, USA: Macmillan, 1971.

[79] J. Meixner, "The behavior of electromagnetic fields at edges," *IEEE Trans. Antennas Propag.*, vol. 20, no. 4, pp. 442–446, Jul. 1972.

[80] B. V. Budaev and D. B. Bogy, "On the electromagnetic field singularities near the vertex of a dielectric wedge," *Radio Sci.*, vol. 42, no. 6, p. RS6S08, 2007.

[81] M. M. Bibby, A. F. Peterson, and C. M. Coldwell, "High-order representations for singular currents at corners," *IEEE Trans. Antennas Propag.*, vol. 56, no. 8, pp. 2277–2287, Aug. 2008.

[82] R. D. Graglia and G. Lombardi, "Singular higher order complete vector bases for finite methods," *IEEE Trans. Antennas Propag.*, vol. 52, no. 7, pp. 1672–1685, Jul. 2004.

[83] G. Lombardi and R. D. Graglia, "Modeling junctions in sharp edge conducting structures with higher order method of moments," *IEEE Trans. Antennas Propag.*, vol. 62, no. 11, pp. 5723–5731, Nov. 2014.

[84] E. Ubeda, I. Sekulic, and J. M. Rius, "Grid-robust discretization of integral equations in the electromagnetic scattering analysis of homogeneous targets with geometric singularities", *accepted for publication in European Conference on Antennas and Propagation (EuCAP)*, Krakow, April 2019.

[85] D. R. Wilton, S. M. Rao, A. W. Glisson, D. H. Schaubert, O. M. Al-Bundak, and C. M. Butler, "Potential integrals for uniform and linear source distributions on polygonal and polyhedral domains," *IEEE Trans. Antennas Propag.*, vol. 32, no. 3, pp. 276–281, Mar. 1984.

[86] R. Graglia, "On the numerical integration of the linear shape functions times the 3-D Green's function or its gradient on a plane triangle," *IEEE Trans. Antennas Propag.*, vol. 41, no. 10, pp. 1448–1455, Oct. 1993.

[87] D. A. Dunavant, "High degree efficient symmetrical Gaussian quadrature rules for the triangle," *Int. J. Numer. Meth. Eng.*, vol. 21, pp. 1129–1148, 1985.

[88] D. H. Schaubert, D. R. Wilton, and A. W. Glisson, "A tetrahedral modeling for electromagnetic scattering by arbitrarily shaped inhomogeneous dielectric bodies," *IEEE Trans. Antennas Propag.*, vol. 32, no. 1, pp. 77–85, Jan. 1984.

[89] E. Ubeda, J. M. Tamayo, and J. M. Rius, Taylor-orthogonal basis functions for the discretizations in method of moments of second kind integral equations in the scattering analysis of perfectly conducting or dielectric objects, *Prog. Electromagn. Res.* vol. 119 pp. 85–105, 2011.

[90] M. B. Stephanson and J. F. Lee, "Automatic basis function regularization for integral equations in the presence of ill-shaped mesh elements", *IEEE Trans. Antennas Propag.*, vol. 61, no. 8, pp. 4139-4147, August 2013.

[91] G. Kang, J. Song, W. C. Chew, K. C. Donepudi, and J. M. Jin, "A novel grid-robust higher order vector basis function for the method of moments," *IEEE Trans. Antennas Propag.*, vol. 49, no. 6, pp. 908-914, June 2001.

[92] S. A. Maier, *Plasmonics: Fundamentals and Applications* (Springer, 2007).

[93] K. L. Kelly, E. Coronado, L. L. Zhao, and G. C. Schatz, "The optical properties of metal nanoparticles: The influence of size, shape, and dielectric environment," J. Phys. Chem. B, vol. 107, no. 3, 668-677, (2003).

[94] J. Homola, "Surface plasmon resonance sensors for detection of chemical and biological species," Chem. Rev. 108, 462-493 (2008).

[95] K. R. Catchpole and A. Polman, "Plasmonic solar cells," Opt. Express 16, 21793-21800 (2008).

[96] J. A. Schuller, E. S. Barnard, W. Cai, Y. C. Jun, J. S. White, and M. L. Brongersma, "Plasmonics for extreme light concentration and manipulation," Nat. Mater. 9(3), 193-204 (2010).

[97] S. Kawata, *Near-field optics and surface plasmon polaritons* (Springer, 2010).

[98] A. L. González, C. Noguez, and A. S. Barnard, "Map of the structural and optical properties of gold nanoparticles at thermal equilibrium," J. Phys. Chem. C, vol. 116, no. 26, 14170-14175 (2012).

[99] M. Kauranen and A. V. Zayats, "Nonlinear plasmonics," Nat. Photonics, vol. 6, p. 737 (2012).

[100] X. Fan, W. Zheng, and D. J. Singh, "Light scattering and surface plasmons on small spherical particles," Light Sci. Appl., vol. 3, no. 6, p. e179, (2014).

[101] D. C. Tzarouchis, P. Ylä-Oijala, and A. Sihvola, "Light Scattering by a Dielectric Sphere: Perspectives on the Mie Resonances," Appl. Sci., vol. 8, no. 2, p. 184, (2018).

[102] I. Sosa, C. Noguez, and R. Barrera, "Optical properties of metal nanoparticles with arbitrary shapes" J. Phys. Chem. B, 107, 6269-6275. (2003)

[103] V. Amendola, O. Bakr, and F. Stellacci, "A study of the surface plasmon resonance of silver nanoparticles by the discrete dipole approximation method: effect of shape, size, structure, and assembly," Plasmonics, 5 85-97 (2010).

[104] O. S. Vartia, P. Ylä-Oijala, J. Markkanen, S. Puupponen, A. Seppälä, A. Sihvola, and T. Ala-Nissila, "On the applicability of discrete dipole approximation for plasmonic particles," J. Quant. Spectrosc. Radiat. Transf., vol. 169, 23-35 (2016).

[105] F. Hao and P. Nordlander, "Efficient dielectric function for FDTD simulation of the optical properties of silver and gold nanoparticles," Chem. Phys. Lett., vol. 446, no. 1-3, 115-118 (2007).

[106] A. M. Kern and O. J. F. Martin, "Surface integral formulation for 3D simulations of plasmonic and high permittivity nanostructures," J. Opt. Soc. Am. A 26, 732-740 (2009).

[107] M. G. Araújo, J. M. Taboada, D. M. Solís, J. Rivero, L. Landesa, and F. Obelleiro, "Comparison of surface integral equation formulations for electromagnetic analysis of plasmonic nanoscatterers," Opt. Express 20, 9161-9171 (2012).

[108] C. Forestiere, G. Iadarola, G. Rubinacci, A. Tamburrino, L. Dal Negro, and G. Miano, "Surface integral formulations for the design of plasmonic nanostructures," J. Opt. Soc. Am. A 29, 2314-2327 (2012).

[109] M. Danckwerts, and L. Novotny, "Optical frequency mixing at coupled gold nanoparticles," Phys. Rev. Lett. 2007, 98, 026104.

[110] N. Grillet, D. Manchon, F. Bertorelle, C. Bonnet, M. Broyer, E. Cottancin, J. Lermé, M. Hillenkamp, and M. Pellarin, "Plasmon coupling in silver nanocube dimers: Resonance splitting induced by edge rounding," ACS Nano, 5, 9450-9462 (2011).

[111] J. Kern, S. Großmann, N. V. Tarakina, T. Häckel, M. Emmerling, M. Kamp, J.S. Huang, P. Biagioni, J. C. Prangsma, and B. Hecht, "Atomic-scale confinement of resonant optical fields.," Nano Lett., 12, 5504-5509 (2012).

[112] D. O. Sigle, J. Mertens, L. O. Herrmann, R. W. Bowman, S. Ithurria, B. Dubertret, Y. Shi, H. Y. Yang, C. Tserkezis, J. Aizpurua, and J. J. Baumberg, "Monitoring morphological changes in 2D monolayer semiconductors using atom-thick plasmonic nanocavities," ACS Nano, 9, 825-830 (2015).

[113] M. Urbieta, M. Barbry, Y. Zhang, P. Koval, D. Sánchez-Portal, N. Zabala, and J. Aizpurua, "Atomic-scale lightning rod effect in plasmonic picocavities: A classical view to a quantum effect," ACS Nano, 12, 585-595 (2018).

[114] L. C. Davis, "Electostatic edge modes of a dielectric wedge," Phys. Rev. B 14, 5523-5525 (1976)

[115] V. Klimov, G. Y. Guo, and M. Pikhota, "Plasmon resonances in metal nanoparticles with sharp edges and vertices: A material independent approach," The Journal of Physical Chemistry C, 118(24), 13052-13058 (2014).

[116] D. C. Tzarouchis, P. Ylä-Oijala, T. Ala-Nissila, and A. Sihvola, "Shape effects on surface plasmons in spherical, cubic, and rod-shaped silver nanoparticles," Applied Physics A, 122(4), 298 (2016).

[117] D. C. Tzarouchis, P. Ylä-Oijala, and A. Sihvola, "Study of plasmonic resonances on Platonic solids," Radio Science, 52, 1450-1457 (2017).

[118] E. Ubeda, I. Sekulic, and J. M. Rius, "Hierarchical discretization of the PMCHWT formulation with jump current discontinuities for the scattering analysis of ferromagnetic objects," *Proc. International Conference on Electromagnetics in Advanced Applications (ICEAA)*, Verona, September 2017, pp. 1093-1096.

[119] R. Fuchs, "Theory of the optical properties of ionic crystal cubes," Phys. Rev. B, vol. 11, no. 4, 1732-1740 (1975).

[120] J. Avelin, A. N. Arslan, J. Brännback, M. Flykt, C. Icheln, J. Juntunen, K. Kärkkänen, T. Niemi, O. Nieminen, T. Tares, C. Toma, T. Uusitupa, and A. Sihvola, "Electric fields in the source region: the depolarization dyadic for a cubic cavity," Electr. Eng., vol. 81, 199-202 (1998).

[121] J. P. Kottmann, O. J. F. Martin, D. R. Smith, and S. Schultz, "Plasmon resonances of silver nanowires with a nonregular cross section," Phys. Rev. B, vol. 64, no. 23, p. 235402 (2001).

[122] A. Tao, P. Sinsermsuksakul, and P. Yang, "Polyhedral silver nanocrystals with distinct scattering signatures," Angew. Chemie Int. Ed., vol. 45, no. 28, 4597-4601 (2006).

[123] S. Zhang, K. Bao, N. J. Halas, H. Xu, and P. Nordlander, "Substrate-induced Fano resonances of a plasmonic nanocube: A route to increased-sensitivity localized surface plasmon resonance sensors revealed," Nano Lett., vol. 11, no. 4, 1657-1663 (2011).

[124] M. B. Cortie, F. Liu, M. D. Arnold, and Y. Niidome, "Multimode resonances in silver nanocuboids," Langmuir, vol. 28, no. 24, pp. 9103-9112 (2012).

[125] L. Hung, S. Y. Lee, O. McGovern, O. Rabin, and I. Mayergoyz, "Calculation and measurement of radiation corrections for plasmon resonances in nanoparticles," Phys. Rev. B, vol. 88, no. 7, p. 75424 (2013).

[126] M. J. Lagos, A. Trügler, U. Hohenester, and P. E. Batson, "Mapping vibrational surface and bulk modes in a single nanocube," Nature, vol. 543, p. 529 (2017).

[127] D. Ramaccia, S. Arcieri, A. Toscano, and F. Bilotti, "Core-shell super-spherical nanoparticles for LSPR-based sensing platforms," IEEE J. Sel. Top. Quantum Electron., vol. 23, no. 2, 1–8 (2017).

[128] U. Hohenester, "Quantum corrected model for plasmonic nanoparticles: A boundary element method implementation," Phys. Rev. B, vol. 91, no. 20, p. 205436 (2015).

[129] H. Wallén, H. Kettunen, and A. Sihvola, "Composite near-field superlens design using mixing formulas and simulations," Metamaterials, 3(3-4), 129-139 (2009).

[130] M. T. Homer Reid and S. G. Johnson , "Efficient computation of power, force, and torque in BEM scattering calculations," IEEE Trans. Antennas Propag., vol. 63, no. 8, 3588-3598 (2015).

List of Publications

Journal articles

J1 **I. Sekulic**, D. Tzarouchis, P. Yla-Oijala, E. Ubeda, and J. M. Rius, "Enhanced discretization of surface integral equations for resonant scattering analysis of sharp-edged plasmonic nanoparticles," accepted for publication in *Physical Review B*

J2 **I. Sekulic**, E. Ubeda, and J. M. Rius, "Versatile and accurate schemes of discretization for the electromagnetic scattering analysis of arbitrarily shaped piecewise homogeneous objects," *J. Comput. Phys.*, vol. 374, pp. 478-494, Dec. 2018.

J3 **I. Sekulic**, E. Ubeda, and J.M. Rius, "Versatile and accurate schemes of discretization in the scattering analysis of 2D composite objects with penetrable or perfectly conducting regions," *IEEE Trans. Antennas Propag.*, vol. 65, no. 5, pp. 2494–2506, May 2017.

J4 E. Ubeda, **I. Sekulic**, J. M. Rius, and A. Heldring "Accurate, grid-robust and versatile combined-field integral equation discretization for the electromagnetic scattering analysis of perfectly conducting targets," submitted to *Journal of Computational Physics*

J5 E. Ubeda, **I. Sekulic**, A. Heldring, and J. M. Rius, "Tangential-normal surface testing for the nonconforming discretization of the electric field integral equation," *IEEE Antennas Wireless Propag. Lett.*, vol. 15, pp. 1581–1584, Jan. 2016.

J6 E. Ubeda, J. M. Rius, A. Heldring, and **I. Sekulic**, "Volumetric testing parallel to the boundary surface for a nonconforming discretization of the electric field integral equation," *IEEE Trans. Antennas Propag.*, vol. 63, no. 7, pp. 3286–3291, Jul. 2015.

J7 A. Camps, H. Park, **I. Sekulic**, and J. M. Rius GNSS-R Altimetry Performance Analysis for the GEROS Experiment on Board the International Space Station, *Sensors*, 2017, vol. 17, pp. 1-18.

Conference papers

C1 **I. Sekulic**, E. Ubeda, J. M. Rius, and A. Heldring, "Regularization of the 2D TE-EFIE for homogeneous objects discretized by the Method of Moments with discontinuous basis functions," in *Proc. Int. Conf. Electromagn. Adv. Appl. (ICEAA)*, Aruba, Aug. 2014, pp. 500–502.

C2 **I. Sekulic**, E. Ubeda, and J. M. Rius, "Tangential-normal line testing for a nonconforming discretization of the Transversal-Electric Electric-Field Integral Equation for 2D conductors," in *Proc. Int. Conf. Electromagn. Adv. Appl. (ICEAA)*, Turin, Italy, Sep. 2015, pp. 581–584.

C3 **I. Sekulic**, E. Ubeda, and J. M. Rius, "Improved accuracy in the scattering analysis of infinitely long ferromagnetic objects," in *Proc. International Symposium on Antennas and Propagation (APSURSI)*, Fajardo, Puerto Rico, July 2016, pp. 309-310.

C4 **I. Sekulic**, E. Ubeda, and J. M. Rius, "Nonconforming discretization of the PMCHWT integral equation applied to arbitrarily shaped dielectric objects," *Proc. European Conference on Antennas and Propagation (EuCAP)*, Paris, Mar. 2017, pp. 311-314.

C5 **I. Sekulic**, E. Ubeda, and J. M. Rius, "Improved accuracy in the scattering analysis of arbitrarily shaped ferromagnetic objects,"*Proc. International Conference on Numerical Electromagnetic and Multiphysics Modeling and Optimization for RF, Microwave, and Terahertz Applications (NEMO)*, Sevilla, May 2017, pp. 167-169.

C6 **I. Sekulic**, E. Ubeda, and J.M. Rius, "Volumetric testing with wedges for a nonconforming discretization of the PMCHWT formulation,"*Proc. Computing and Electromagentics International Workshop (CEM)*, Barcelona, June 2017, pp. 7-8.

C7 **I. Sekulic**, E. Ubeda, and J. M. Rius, "Versatile and accurate electromagnetic analysis of piecewise homogeneous composite objects," *Proc. European Conference on Antennas and Propagation (EuCAP)*, London, April 2018, pp. 1-4.

C8 **I. Sekulic**, E. Ubeda, and J. M. Rius, "Nonconforming domain decomposition method for the flexible analysis of multiscale penetrable structures," *Computing and Electromagnetics International Workshop (CEM)*, Stellenbosch, South Africa, 2018.

C9 E. Ubeda, **I. Sekulic**, and J. M. Rius, "Efficient and accurate electromagnetic scattering analysis of perfectly conducting thick plates," *accepted for publication in International Symposium on Antennas and Propagation (APSURSI)*, Atlanta, July 2019.

C10 E. Ubeda, **I. Sekulic**, and J. M. Rius, "Grid-robust discretization of integral equations in the electromagnetic scattering analysis of homogeneous targets with geometric singularities," *accepted for publication in European Conference on Antennas and Propagation (EuCAP)*, Krakow, April 2019.

C11 E. Ubeda, **I. Sekulic**, and J. M. Rius, "Hierarchical discretization of the PMCHWT formulation with jump current discontinuities for the scattering analysis of ferromagnetic objects," *Proc. International Conference on Electromagnetics in Advanced Applications (ICEAA)*, Verona, September 2017, pp. 1093-1096.

C12 E. Ubeda, **I. Sekulic**, and J. M. Rius, "Balanced tangential testing for the nonconforming discretization of the Electric-Field Integral Equation on open PeC surfaces," *Proc. International Symposium on Electromagnetic Theory (EMTS)*, Aalto, August 2016, pp. 472-475.

C13 E. Ubeda, **I. Sekulic**, J. M. Rius, and A. Heldring, "Testing over the boundary interface for the nonconforming discretization of the Electric-Field Integral Equation," *Proc. International Symposium on Antennas and Propagation and USNC/URSI National Radio Science Meeting*, Vancouver, July 2015, pp. 1170-1171.

C14 E. Ubeda, **I. Sekulic**, J. M. Rius, and A. Heldring, "Volumetric testing for the nonconforming discretization of integral equations in scattering problems," *Proc. European Conference on Antennas and Propagation (EuCAP)*, Lisbon, April 2015, pp. 1-4.

C15 E. Ubeda, **I. Sekulic**, J. M. Rius, and A. Heldring, "Versatile facet-oriented discretization of the electric-field integral equation," *Proc. Computational Electromagnetics International Workshop (CEM)*, Izmir, July 2015, pp. 1-2.